Novel Parylene Filters for Biomedical Applications

Thesis by

Yang Liu

In Partial Fulfillment of the Requirements for the

degree of

Doctor of Philosophy

Caltech

CALIFORNIA INSTITUTE OF TECHNOLOGY

Pasadena, California

2016

(Defended on May 17th, 2016)

To my parents and my loved ones

Acknowledgements

First and foremost, I would like to express my sincere gratitude to my advisor Prof. Yu-Chong Tai. It is him who brought me into the world of scientific research and continues guiding me with his knowledge, enthusiasm, and patience. He motivates me whenever I'm facing difficulty and he is always trying to teach me not only knowledge, but also more importantly, the way of thinking. From him I learned how important it is to analyze questions logically and the role of fundamentals play when tackling scientific problems. Deeply in my heart I respect him so much as a perfect teacher, an outstanding researcher, and an influential mentor in every aspects of life from whom I keep learning. What he has taught will benefit me for my whole life profoundly. It has always been my greatest honor to have him as my advisor.

Besides Prof. Yu-Chong Tai, I would like to thank other professors in my committee, Prof. Hyuck Choo, Prof. Azita Emami, Prof. Amir Goldkorn, and Prof. Mikhail Shapiro for their great insights and invaluable comments.

I would also like to thank all my labmates from Caltech MEMS lab. They are my best friends and I feel so lucky to have them in my life. I appreciate so much for their thoughts, suggestions and help both on research and on other aspects of life. How could I ever forget all the wonderful time I spent together with these amazing guys? We have gone through good and bad times and our friendship grows stronger and stronger. In particular, I would like to thank Dr. Han-Chieh (Jay) Chang, Dr. Jungwook (Jun) Park, Dr. Young-Hyun (Justin) Kim, Dr. Bo Lu, and Dr. Dongyang (Clark) Kang for training me to help me get started during my first few years, and Dr. Yuan Luo, Nicholas

Scianmarello, Xiaoxiao (Shell) Zhang, Aubrey Shapero, and Colin Cook for the generous support, brilliant ideas, and invaluable discussions. You guys are more than friends to me because you have always been backing me up and fight by my side like brothers in arms. There is a long time ahead and we have great things to expect. Many thanks go to Mr. Trevor Roper and Mrs. Christine Garske for your day-to-day support, creating an amazing environment where research goes on smoothly all over the years!

My sincere appreciation also goes to collaborating professors from other institutions, in particular to Prof. Amir Goldkorn, Prof. Kevin Ferrari and Prof. Nanhai Chen. Thanks so much for your effort in the projects and guiding me through the research. I would also like to thank all my co-workers, especially Dr. Tong Xu and Dr. Yucheng Xu for collaborating with me to push the projects moving forward.

Last but not least, I would like to thank my parents as well as other family members. They have always been my biggest support and the source of strength. My special thanks belong to my girlfriend Liqian (Angela) Shu, whose love is the most precious treasure in my life.

Abstract

Novel Parylene Filters for Biomedical Applications

Thesis by

Yang Liu

Doctor of Philosophy in Electrical Engineering

California Institute of Technology

Medical engineering plays a more and more important role in driving the fundamental biology research moving forward. The work presented in this thesis targets at engineer smart parylene filters for various biomedical applications. Three smart parylene membranes are discussed. The first device is parylene magnesium-embedded filter for circulating tumor cells isolation. Circulating tumor cells (CTCs) are cells that slough off the edges of a primary tumor and are swept away by the bloodstream or lymphatic system into the vasculature. They constitute seeds for subsequent growth of additional tumors in vital distant organs, triggering a mechanism that is responsible for the vast majority of cancer-related deaths. Thus CTCs in peripheral blood have been investigated as a valuable biomarker for patients with various types of cancers. However, CTCs are difficult targets to probe owing to their extremely low concentration in peripheral blood. Although rare, CTCs represent a potential approach for the detection,

characterization and monitoring of non-haematologic cancers. Therefore, CTCs capture from whole blood has been identified to be an unmet need for cancer research and effective cell separation methods are required to facilitate the study of CTCs. In this study, we developed a novel design applying a buried sacrificial Magnesium (Mg) layer underneath the original microfilter. After filtration, the filter was immersed in DMEM. When the thin-film Mg was dissolved, the cells were released and thus were ready for further biology analysis.

The second device is parylene based microelectrode filter for single-islet electroisletogram. Other than direct insulin injection, one promising treatment for Type I diabetes is islet transplantation. However, one of the key lacking technologies of islet transplantation is high-throughput islet screening since each transplantation requires about one million islets. Islets, which are heterogeneous by nature, are currently screened as whole populations containing a range of functioning and dysfunctional characteristics. This work represents the first attempt to develop a MEMS technology for the screening of every single islet so as to guarantee no bad islet at all, which should improve results of islet transplant therapy. Here we report the first MEMS device designed for in vitro measuring of electroisletogram (EIG) of individual rat islets. Strong EIG signals in millivolt range are obtained. This work proves the feasibility of using MEMS and EIG for high-throughput screening, in contrast to patch-clamp measurements, of islets for transplantation to treat diabetes.

The third device is parylene-on-PDMS membrane for vaccine production. A parylene-on-PDMS design is proposed to supply oxygen to CV-1 cells for vaccine production. Because the cells are seeded and attached right onto the surface of the device,

extra oxygen is provided through permeation from the PDMS and thin parylene layers. The permeation is studied and cell growth experiments are performed to demonstrate the feasibility of the device. Compared to commercialized bioreactors, this novel design could have large cell density because oxygen is supplied locally and shear force is not a limiting factor any more.

Besides the three devices, parylene properties are also studied and a novel origami design is proposed, which can potentially increase the surface areas of the membranes by fold the 2D flat film into 3D structures. Details are discussed in the following chapters.

Table of Contents

List of Figures

List of Tables

1 INTRODUCTION

This chapter focuses on the introduction of parylene. First of all, the parylene family and the common members are discussed, followed by advantages of parylene as a biocompatible material. Next, the chemical vapor deposition (CVD) processing technology is presented to illustrate how does parylene dimers becomes a uniform coating on substrates. The state-of-art research on parylene in bio-MEMS applications are investigated to demonstrated that parylene is indeed a promising material candidate, drawing more and more attentions from researchers in the relative fields. Parylene membrane applications are also presented as a case in bio-MEMS applications. Parylene membrane normally indicates a sheet of parylene with a wide range of microstructures, such as holes, microchannels, crease patterns etc. for different applications. After the review of parylene, micro-mechanical-electrical-system (MEMS) is introduced for the reason that all the parylene micro-machining techniques are within the processing knowledge of MEMS. Three most common and fundamental technologies are presented, which are lithography, bulk machining, and thin-film process. Lithography is the process that creates patterns on certain photoresists for the purpose of future structure constructions. Bulk machining mainly refers to etching techniques to create trenches,

holes and channels. Both wet etching and dry etching are discussed. Thin-film process part focuses on the metal thin film, including gold, platinum, aluminum, and magnesium, etc. With all the discussions mentioned above, the foundation as well as background of parylene based smart membrane filters for bio-MEMS applications that will be presented in the following chapters are laid.

1.1 Parylene

Parylene is a polymer group of poly-xylylene. Each member in the group has slightly different chemical modification based on parylene-N, which gives us different materials properties. [1] Figure 1-1 shows the chemical structures of some members in the parylene group.

parylene-C   *parylene-D*   *parylene-N*
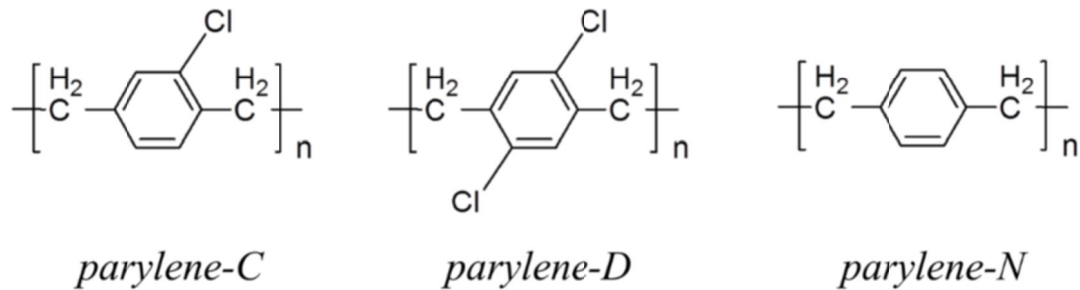
Figure 1-1: Chemical structures of common members in the parylene family: parylene-C, parylene-D and parylene-N (http://scscoatings.com/what-is-parylene/parylene-properties/)

1.1.1 Advantages as a BioMEMS Material

Parylene-C is one of the most widely used biomaterials, especially in the bioengineering applications. U.S. Pharmacopeia certifies it as Class VI biocompatible

material. Besides biocompatibility, it also has good mechanical properties, such as Young's modulus and elongation to break. The optical transparency is also a favorable property for practical experiments [2]. It is also a highly inert material that can stand severe chemical corrosion. Last but not least, parylene-processing technique is totally compatible with traditional MEMS fabrication methods. The thin-film of parylene can be deposited on to any substrate, including both solid and liquid, with precisely controlled thickness. The machining of the parylene thin film can be done with MEMS processes, for instance, the etching of parylene film can be accomplished through oxygen plasma, and both chemicals and different plasmas can change the surface properties. Therefore for all the reasons mentioned above, parylene-C is a perfect choice for substrate of devices in the bioMEMS field.

In our research, due to the application requirements and the advantages of parylene-D, parylene-D is also applied and studied together with parylene-C, which will be introduced in the following chapters.

.

1.1.2 Processing Technologies

Figure 1-2 shows the low-pressure chemical vapor deposition process (LPCVD) of parylene. The parylene dimer (Specialty Coating System) is weighted in an aluminum boat and put into the vaporizer for heating up. The vaporizer temperature is set up to 150 degree C and the parylene dimer becomes gas phase. Then the parylene vapor flows through the tube into the pyrolysis furnace, where it is heated up to 690 degree C. Of course the whole space is under vacuum because of continuous pumping of mechanical pump. In the pyrolysis tube, the dimer of parylene breaks up into monomer due to the

high temperature. Monomer gas then flow into the coating chamber which is under the room temperature. The monomer forms polymer by crosslinking. It will coat everywhere in the chamber where the sample or product is placed beforehand. Because of uniform coating, a glass slide is always put in for the purpose of thickness measurement later on. The rest of monomer gas flows into the cold probe afterwards and get trapped because of the low temperature. Last but not least, a mechanical pump is connected to the whole system to bring the pressure down during the coating process.

The previous paragraph has briefly introduced the deposition process of parylene film. After deposition, it is also important to perform the micromachining of the parylene layer, normally on the surface of silicon wafer. To do that, lithography as well as dry etching techniques are involved. Lithography is used to pattern a mask layer on top of parylene, which will be introduced in the "MEMS technology" section in this chapter. Here, dry etching will be introduced in advance. Oxygen is used as the primary gas for the plasma etching. To generate the plasma, RIE (reactive ion etching) or DRIE is used. The plasma is generated by high frequency magnetic field under low pressure. Frequency is set to 13.56 Megahertz. 400-Watt power, 200-mTorr pressure recipe is optimized as the standard parylene etching method. An etching rate of 0.2-micron/ minute can be achieved.

Dimer

Cℓ

CH2 — ⬡ — CH2

CH2 — ⬡ — CH2

Cℓ

vaporizer →

Dimer, in powder form is added to the machine and heated to 150°C and changed to a vapour state.

stage 1

Monomer

Cℓ

CH2 — ⬡ — CH2

CH2 = ⬡ = CH2

Cℓ

pyrolysis furnace

Next, the Dimer molecule is heated to 690°C, 0.5 torr. This changes the molecular structure to a monomer.

stage 2

Polymer

Cℓ

⟦ CH2 — ⬡ — CH2 ⟧

At room temp, the monomer becomes a polymer, bonding to products placed in the coating chamber.

YOUR PRODUCT

coating chamber

stage 3

liquid cold trap

Excess process gas travels from the coating chamber into an external liquid cold trap.

stage 4

Figure 1-2: low-pressure chemical vapor deposition process (LPCVD) of parylene (lnf-

wiki.eecs.umich.edu)

1.1.3   Overview of Research on Parylene Based BioMEMS

Parylene has been well known as a protective coating material. Research on parylene involves packaging, encapsulation, microfluidic channels and so on. Recently more and more research has been done using parylene as a biocompatible material. In the area of implantable medical devices, Jay *et al.* has published research on retinal prosthesis [3] and Johnson *et al.* reported a novel parylene based cochlear implant to help recover hearing ability [4]. In the areas of cell filtration and cell culturing, Bo *et al.* has

done a tremendous amount of research [5]. Besides all mentioned above, packaging techniques using parylene is a big area as well. For instance parylene on silicone oil packaging for intraocular pressure senor [6].

1.2 Parylene Membrane Applications

In this section we focuses on research targeting to parylene membrane. Besides all the research mentioned above, parylene membrane applications specifically refer to MEMS devices build on a sheet of parylene. The parylene membrane acts as the flexible substrate and the devices fabricated on top of that may contain other layers of thin films or different structures like microchannels regarding different applications. Under some circumstances the surface of parylene also needs selectively special treatments, for instance, for cell culturing on selective areas. Because of the advantages on flexibility, optical transparency and biocompatibility, parylene membrane is a perfect substrate for devices that involve biology experiments. The following chapters will discuss several parylene membrane applications for different purposes.

1.3 MEMS Technologies

MEMS is short for micro-electro-mechanical-system. It refers to technologies that build micron scale integrated devices including both electrical and mechanical components. It emerges because of the development of semiconductor and IC design and fabrication industries [7]. The famous commercialized MEMS industry products include

accelerometers and gyroscopes that have been used widely across all kinds of portable devices. Different from semiconductor chip fabrication, MEMS includes mechanical parts besides the electrical circuits. The mechanical parts can be both sensors and actuators. Figure 1-3 shows a MEMS device with micro mechanical gears.

Figure 1-3: a MEMS device with micro mechanical gears (www.thenanoage.com)

From the date that the first silicon pressure sensor was demonstrated in 1961, MEMS has developed into an interdisciplinary subject that combines mechanical engineering, electrical engineering, chemical engineering, material science, biomedical engineering, and so on. The state of art research on MEMS is not limited to a single, narrow application, but to a wide range of areas, such as RF MEMS, bioMEMS, packaging techniques, etc., which is much broader than the semiconductor industry. In the following subsections, the fundamental traditional MEMS fabrication techniques will be introduced and discussed.

1.3.1 Photolithography

Photolithography is one of the most important techniques in the MEMS fabrication field. It is a process that transfers whatever pattern on the chrome-glass mask to the photoresist layer on the wafer. This step is crucial because it needs to provide the resolution high enough to get the device with the most accuracy and the smallest feature size. Photoresist is sensitive to light under certain wavelengths. Different photoresists have different spectrum but the most widely used ones are most sensitive to UV light. There are 2 different kinds of photoresists, which are positive photoresists and negative photoresists. They are different from the fact that for positive photoresists, the pattern on the chrome-glass mask will be totally transmitted to the photoresists in the same way. By saying that, the part on the mask where there is chrome corresponds to the part where photoresist stays on the wafer; while the part on the mask where there is only glass corresponds to the part where the photoresist will be gone after developing in photoresist developer, in our case, AZ 340. For the negative photoresist, things work oppositely. The transparent parts on the mask corresponds to the parts where photoresist remains after developing process while the parts with chrome result to the parts that photoresist will be gone. This whole argument is clearly seen in Figure 1-4.
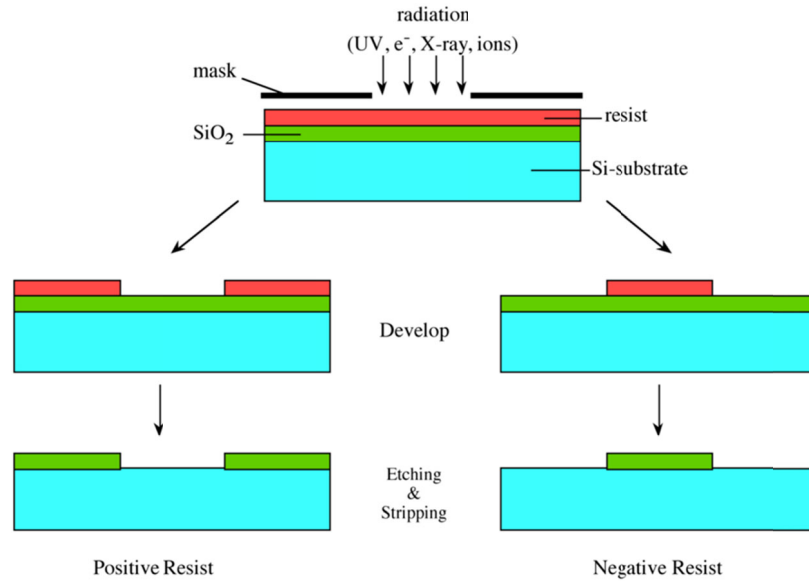
Figure 1-4: Lithography process shows the difference between positive and negative

photoresist (nanotechnologyandsensors.blogspot.com)

The reason of difference is that when positive photoresist got exposed to UV light, the most common types of photoresist become soluble to developer, while for the negative photoresist, after explosion to the UV light, becomes cross-linked and therefore non-soluble to the developer.

The fabrication methods of photoresist thin layer include 3 most common methods: namely spinning, spray coating, and lamination. Spinning refers to the use of spinner machine, which creates vacuum to keep the wafer on the chuck while spinning. The spin rate and time are the most important parameters to tune. For example, Figure 1-5 shows the relationship between the spin rate and the thickness. It is very clear that as the spinning speed increases, the thickness of the photoresist film decreases in a near exponential way. Spray coating is to use a specially designed spray coater and to shower the wafer with photoresist droplets of very small size. Lamination is mainly used for a

kind of negative photoresist, which is called "dry film". The hot-roll temperature, the pressure and the hot-roll speed are controlled and optimized to have the best lamination and adhesion result of dry film. Dry film is a very convenient material to make thick mold. It is a negative photoresist and one layer is 120 microns. If thicker dry film is needed, multiple layers can be laminated.
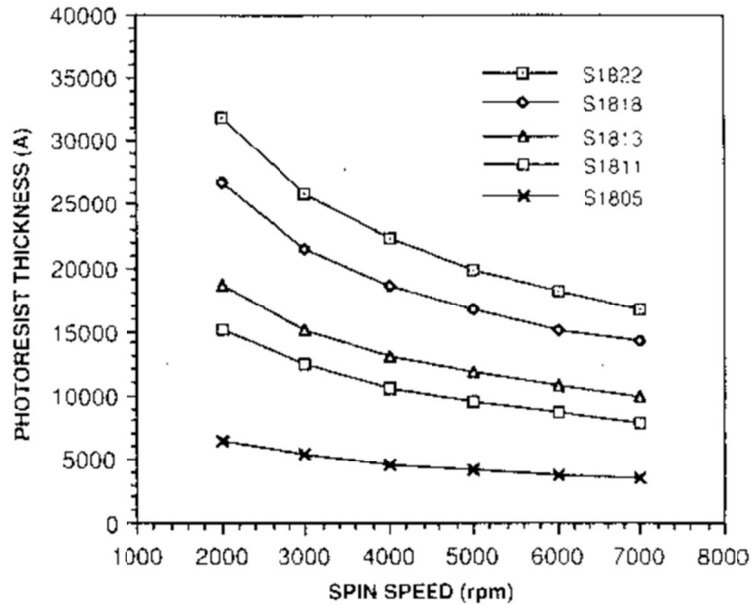
Figure 1-5: Relationship between photoresist thickness and spin speed of photoresist

(www.seas.upenn.edu)

After making the thin photoresist layer, soft baking process is always necessary to solidify the photoresist. Under 100-degree C for 30 minutes, the majority of solvent in the photoresist will evaporate. Exact data of photoresist AZ 4620 on the weight change inside oven after baking for certain time is plotted below. The mass loss is measured by analytical balance after a certain period of time in the oven.
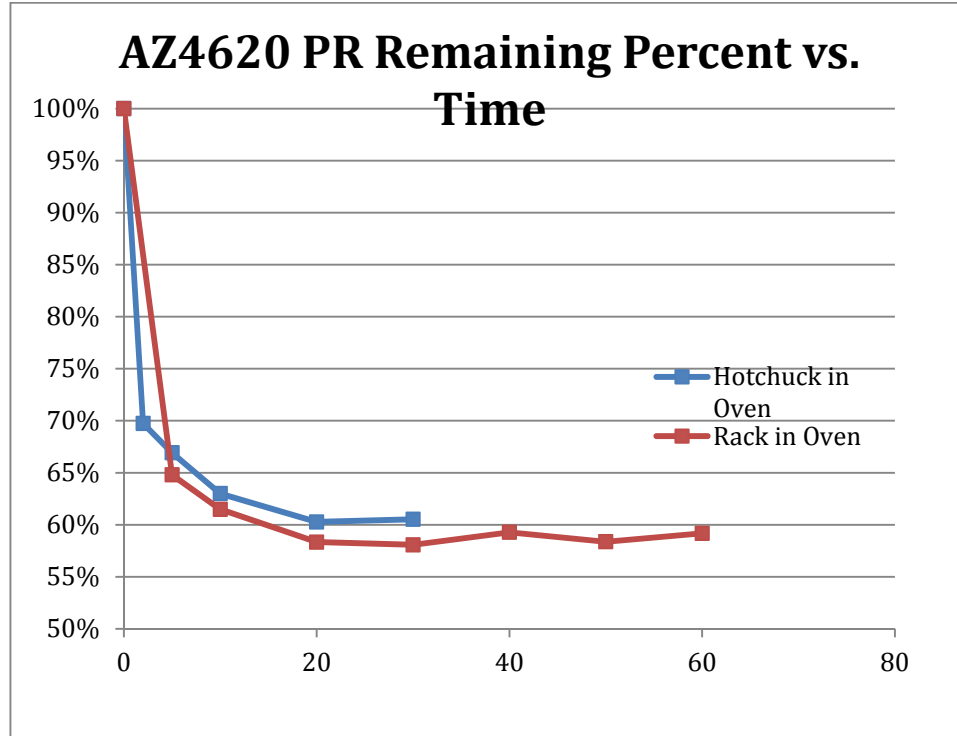
Figure 1-6: Relationship of AZ4620 photoresist remaining weight over time

Once soft baking is done, the wafer is ready for UV exposure. The alignment must be perfect (less than 2 micron error) in order to get the same resolution of 2 micron. Besides that, a successful exposure also need right power and time. If both are low, the photoresist cannot be exposed through. If both are high, the exposed area will be bigger than the area on the mask because the light is not 100% straight down.

Once exposure step is finished, the wafer will be put into developer, which is commonly based. Time and rotation are important factors to control in order to get perfect patterns on the wafer. DI water is used to rinse off the remaining developer. Spin-dry is applied afterwards to get rid of water. Hard baking is followed if necessary.

As discussed above, photoresist lithography process is extremely important for MEMS fabrication processes. For industry and high-level research labs, this process has been automated for many years but it is still important to gain hands-on experience and the knowledge of the basics.

1.3.2   Bulk Micromachining

Bulk micromachining refers to the fabrication process where the bulk material needs to be partially removed. In MEMS technology, it commonly refers to etching techniques. The etching techniques can be divided into two parts: wet etching and dry etching. Wet etching method is applied by using corrosive etchants. On the other hand, dry etching refers to plasma etching such as RIE (reactive ion etching) and DRIE (deep reactive ion etching).

The etching methods can also be divided into isotropic and anisotropic. For the isotropic etching, the etching rate of the substrate is same at all directions. It indicates that the chemicals will etch the materials under the etching mask. This phenomenon is called undercut. Figure 1-7 shows the undercut problem of isotropic etching.
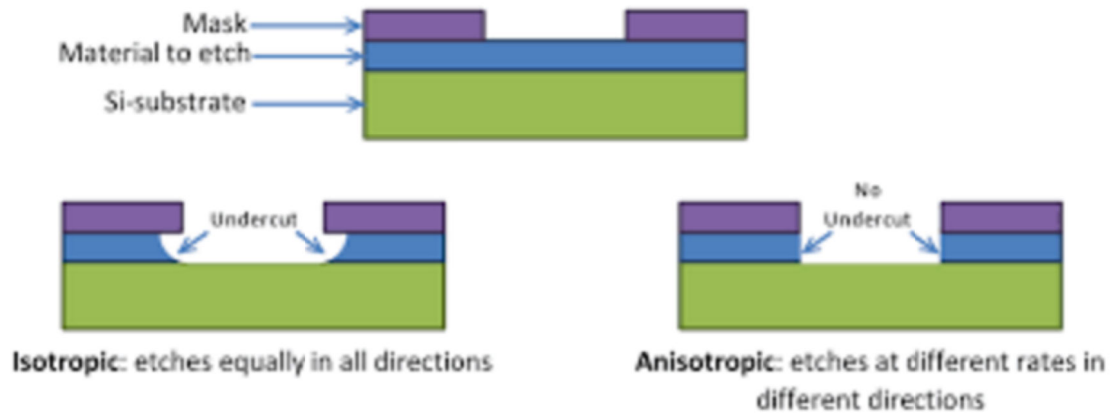
Figure 1-7: undercut phenomenon of isotropic etching (www.engr.ucsb.edu)

RIE and DRIE etching belong to anisotropic etching. They perform etching via plasma. The local equivalent temperature can be as high as thousands of degree C. RIE utilizes RF (radio frequency) power, which is commonly at 13.56 MHz to accelerate the ions to perform the etching via bombardment. RIE has pretty high aspect ratio, and DRIE has even higher. It applies a process call "Bosch process". In Bosch process, the protective layer is coated within a cycle to prevent the further etching of the sidewalls. The result of DRIE is shown in Figure 1-8. If deep channel needs to be created, RIE or DRIE are definitely the first choice.
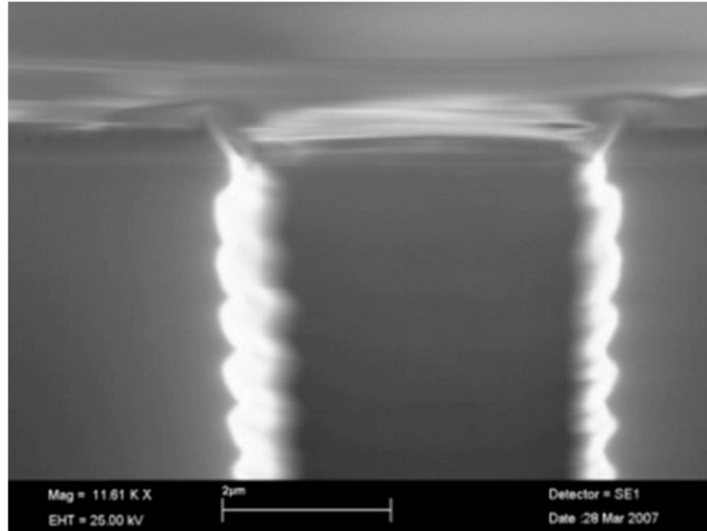
Figure 1-8: SEM photo of DRIE etching result (www.spts.com)

1.3.3   Thin Film Process

In MEMS technology, thin film process refers to creation of a layer with thickness of nanometers to microns. It is a process that has been widely used in different industries: semiconductor, LEDs, optical coatings and so on. [8] There are many different fabrication methods of different materials, such as chemical vapor deposition (CVD) of parylene, which we have introduced in previous sections. Here, we will discuss another method: physical vapor deposition (PVD) for metal thin film process. There are two important machines for PVD: thermal evaporator and Ebeam. Figure 1-9 shows the working principles of the two methods.
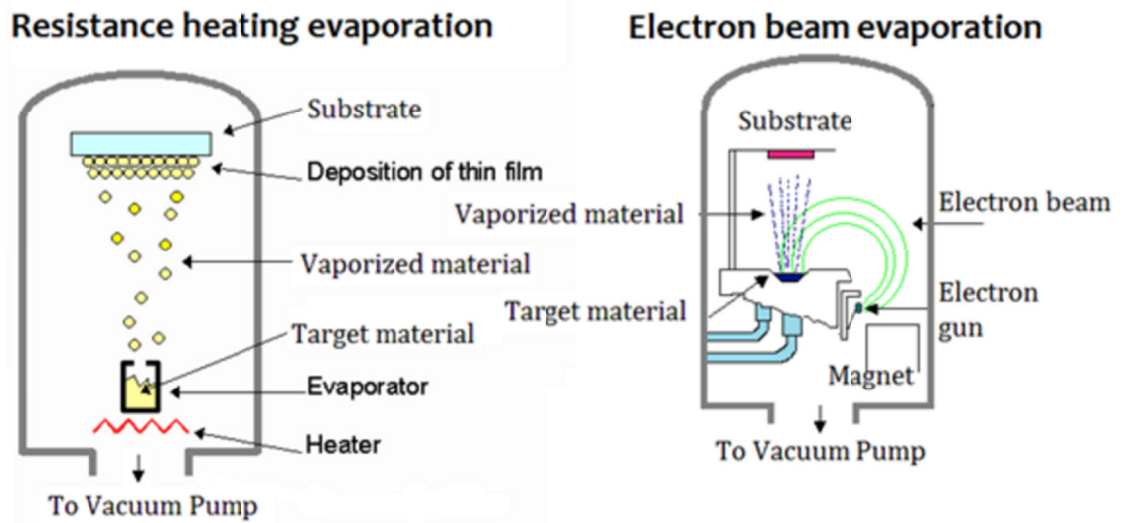
Figure 1-9: Illustration of thermal evaporator and Ebeam process (hivatec.ca)

Thermal evaporator takes advantage of resistive heating to heat up the target material. The vaporized material deposited on the substrate as a thin film. Ebeam applies electron beam to heat up the target material. Both need to be done under vacuum. Because of the different melting points for different materials, sometimes a backside cooling system on the substrate is needed for high melting point metals, like platinum. In order to reach an extremely low pressure, two-stage pumping is used on Ebeam (rough mode and high vac mode). Both mechanical pump and diffusion pump are used to meet the pressure requirement.

The commonly used thin films for MEMS applications include Titanium, Gold, Platinum, Chrome, and Aluminum. Recently Magnesium is also found to be a good metal that Magnesium thin film fabrication is totally compatible with Ebeam [9]. Magnesium has plenty of good properties that can benefit bioMEMS devices, such as

biodegradability. Detailed magnesium fabrication process and characterization will be discussed in the following chapters.

1.4   Layout of the Dissertation

Chapter 2 focuses on parylene characterization, including both mechanical tests and research on parylene surface modifications. Characterization of parylene material properties is the fundamental stuff to perform before design and build devices for the reason that understanding and having the ability to modify the material will help solve problems of device performance.

Parylene smart filter devices are introduced chapter by chapter. Chapter 3 focuses on the topic "parylene magnesium-embedded filter for circulating tumor cells isolation", in which a parylene based filter is designed, fabricated and tested for the capture and release of circulating tumor cells. Chapter 4 discussed the topic "parylene based microelectrode filter for single-islet electroisletogram". A novel design of parylene based filter for electroisletogram recording and analysis is presented. Chapter 5 introduced parylene membrane for vaccine production. Ultra-thin parylene, which is oxygen permutable, is used for cell culturing. The last chapter is on parylene origami structure. It focuses on a novel design of folding 2D parylene film into 3D structure, which opens many doors for new applications on parylene membranes.

1.5   Summary

In this chapter, the parylene materials as well as state-of-art applications are

introduced. Research on parylene membrane devices is also reported to show that parylene based devices are becoming more and more attractive in bioMEMS research. MEMS technologies are discussed afterwards. Important techniques are introduced, such as lithography process, bulk micromachining, and thin film processes. The background introduction will lay the foundation of the discussion on the devices in the following chapters.

1.6   Reference

[1]   SCS   parylene   properties.   Available: http://scscoatings.com/what-is-parylene/parylene-properties

[2]   *Parylene   -   Wikipedia,   the   free   encyclopedia*.   Available: https://en.wikipedia.org/wiki/Parylene

[3]   J. Chang, Y. Liu, and Y.C. Tai, Reliable packaging for parylene-based flexible retinal   implant,   *Solid-State   Sensors,   Actuators   and   Microsystems (TRANSDUCERS & EUROSENSORS XXVII), 2013 Transducers & Eurosensors XXVII: The 17th International Conference on.* pp. 2612-2615, Jun 2013

[4]   A.C. Johnson, A robust batch-fabricated high-density cochlear electrode array, *Micro electro mechanical system (MEMS), 2010 International conference on.* pp. 1007 - 1010, Jan 2010

[5]   B. Lu, S. Zheng, B. Quach, and Y.C. Tai, A study of the autofluorescence of parylene materials for μTAS applications, *Lab Chip*, vol.10, pp. 1826-1834, 2010

[6]   A. Aubrey, Y. Liu, and Y.C. Tai, Parylene-on-oil packaging for implantable pressure sensors, *Micro electro mechanical system (MEMS), 2016 International conference on.*   pp. 403-406, Jan 2016

[7]   *MEMS   -   Wikipedia,   the   free   encyclopedia*.   Available: https://en.wikipedia.org/wiki/Microelectromechanical_systems

[8]   *Thin   Film   -   Wikipedia,   the   free   encyclopedia*.   Available: https://en.wikipedia.org/wiki/Thin_film

[9]   Y. Liu, J. Park, J. Chang, and Y.C. Tai, Thin-film magnesium as a sacrificial and biodegradable material, *Micro electro mechanical system (MEMS), 2014 International conference on.*   pp. 656-659, Jan 2014

2 PARYLENE CHARACTERIZATION

2.1 Introduction

Parylene-C is the most widely used material within the parylene family, especially for the bioengineering applications. It is the Class VI certified biocompatible material by U.S. Pharmacopeia. Besides biocompatibility, it also has good mechanical properties, such as Young's modulus and elongation to break. The optical transparency is also a favorable property for practical experiments. It is also a highly inert material that can stand severe chemical corrosion. Last but not least, parylene-processing technique is totally compatible with traditional MEMS fabrication methods. The thin-film of parylene can be deposited on to any substrate, including both solid and liquid, with precisely controlled thickness. The machining of the parylene thin film can be done with MEMS processes, for instance, the etching of parylene film can be accomplished through oxygen plasma, and both chemicals and different plasmas can change the surface properties. Therefore for all the reasons mentioned above, parylene-C is a perfect choice for substrate of devices in the bioMEMS field.

In our research, due to the application requirements and the advantages of parylene-D, parylene-D is also applied and studied together with parylene-C, which will be introduced in the following sub-chapters.

2.2   Mechanical Properties

The mechanical properties of the parylene-C film were studied using TA Instruments DMA Q800. Among many mechanical properties, Young's modulus, tensile strength, elongation, glass transition temperature, and Rheological Properties are primarily concerning in terms of implantation applications. Therefore they were considered in this chapter. Mechanical properties can be known by many ways. For example, Young's modulus and residual stress can be obtained simultaneously by the load-deflection approach [10]. In our study, mechanical properties were obtained by uniaxial tensile test due to its simplicity and popularity.

2.2.1   Dynamic Mechanical Analysis (DMA)

We applied dynamic mechanical analysis technique to study and characterize the viscoelastic behavior of polymers. Complex modulus is obtained by applying the sinusoidal stress first and the resulting strain is measured. A diagram of this process is shown in Figure 2-1.
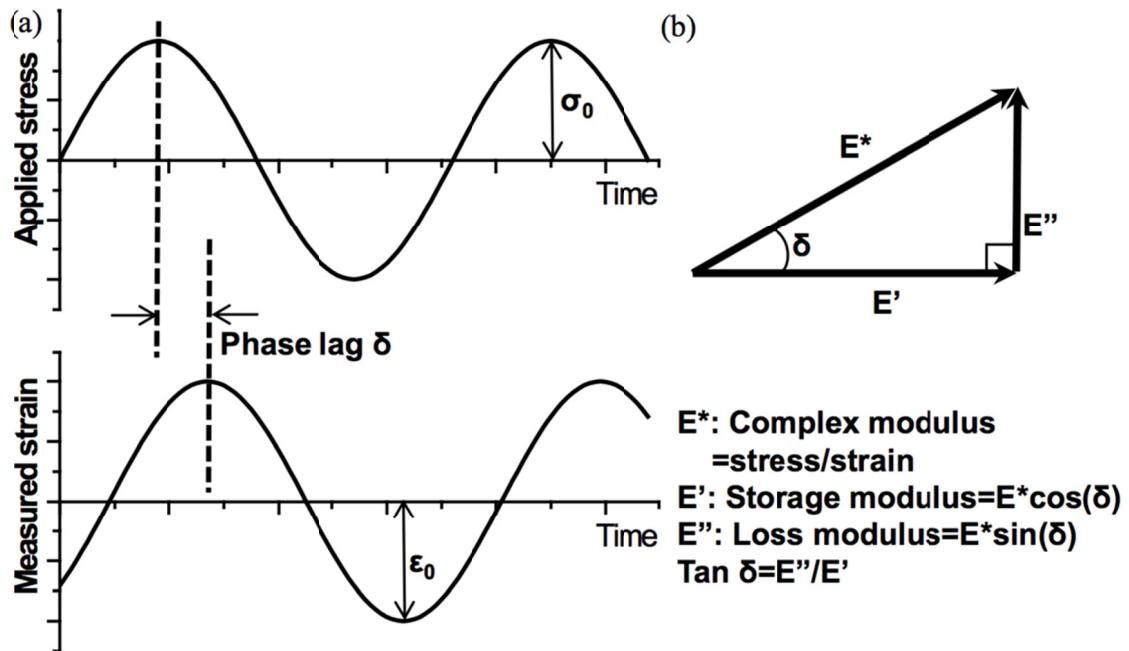
Figure 2-1. The concept of DMA. (a) A sinusoidal stress is applied and the sinusoidal strain response with a phase delay for viscoelastic materials is measured. (b) The relationship between complex modulus, the storage modulus, and the loss modulus [10]

2.2.2 Uniaxial Tensile Test

Uniaxial tensile test is one of the most fundamental and popular tests used to measure the mechanical properties of a material. This section describes the fabrication process of the tensile test samples. A 4-inch wafer is prepared for fabrication after piranha plus buffered hydrofluoric acid (BHF) cleaning, and then hexamethyldisilazane (HMDS) treatment respectively. A 17-μm-thick PA-C film is then deposited over the wafer through LPCVD and then the film was cut into 5.3-μm-wide strips for testing. The gauge length was taken as 10 mm for uniaxial tensile test. Different conditions of

parylene treatments are studied, which are as-deposited, 100°C, 150°C, and 200°C annealed for 30 minutes.

The tensile test is performed under 37°C because the real surgical situation needs to be simulated where the parylene based medical device is implanted. Procedures are described as follows. First, raise the environment temperature to 37°C; maintain isothermal for 30 minutes; finally ramp the strain at 0.5%/minute up to 250% (PA-C samples break before reaching 250% elongation). Figure 2-2 shows the nominal stress/strain curves of PA-C films annealed at different temperatures (as-deposited, 100°C, 150°C and 200°C) for 30 minutes. The sample annealed at 100°C shows 76.3% elongation, while 150°C and 200°C show 10.1% and 2.5%, respectively. Considering stretching and bending in practical surgery process, 100 °C annealing is appropriate. In addition, since the time constant of PA-C crystallization is shorter than 1 minute [10], so a 30-minute thermal annealing is sufficient.
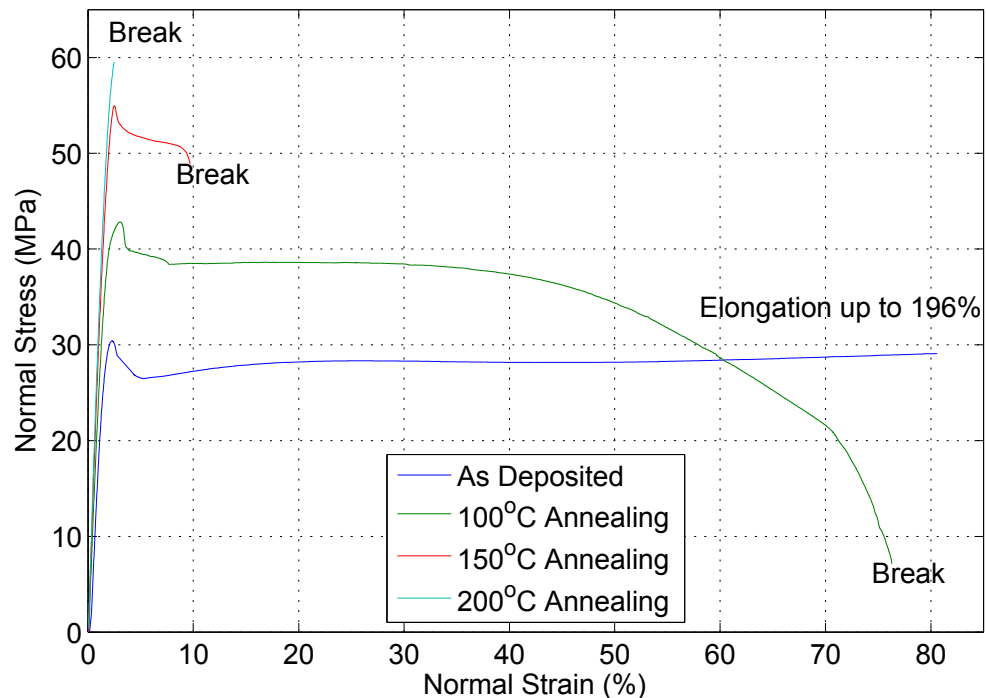
Figure 2-2. Tensile test at 37 °C to choose annealing temperature: 100, 150, 200 °C

annealed samples (for 30 minutes) show 76.3%, 10.1%, 2.5% elongation respectively.

Figure 2-3. DMA setup for tensile test of PA-C film. Shown in the figure is a 200°C pre-

annealed sample but broken after the tensile test.

2.2.3   Glass Transition Temperature (Tg) Test

Because parylene is viscoelastic material, studying the glass transition

temperature is valuable. The material behaves differently below and above the glass

transition region: below is glassy region and above is rubbery region. As shown in Figure

2-4, the left region is the glassy region. The material has relatively higher elastic modulus

and the polymer behaves like an elastic material. In the glass transition region, as the

temperature goes up, the elastic modulus decreases gradually due to the higher polymer

chain mobility [10]. Therefore, as the temperature goes over a critical temperature, i.e.,

glass transition (or second transition) temperature, T_g, the free volume increases to be

higher than 2.5 Vol.-%, permitting different kinds of chain movements as well as moving

in various directions [11, 12]. In addition, higher temperature also provides the polymer chain more energy and makes the chain movement even easier [10].
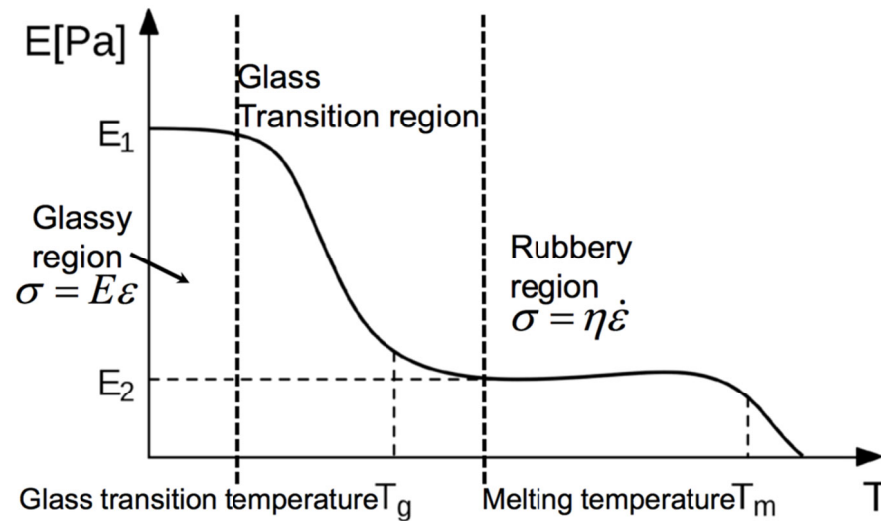
Figure 2-4. Elastic modulus vs. temperature of viscoelastic materials [10]

Here, we firstly measured the glass transition temperature (Tg) of parylene-D (PA-D). PA-D potentially can be a better material than PA-C in terms of the stability of mechanical properties under a high temperature environment, for example, the human body. There are many ways to measure Tg and the results are slight different from each other. Here we choose to apply the storage modulus vs. temperature method by using DMA. Figure 2-5 shows that the glass transition region is from around 82.02 °C to around 87.18 °C. The glass transition temperature is around 84.70 °C.
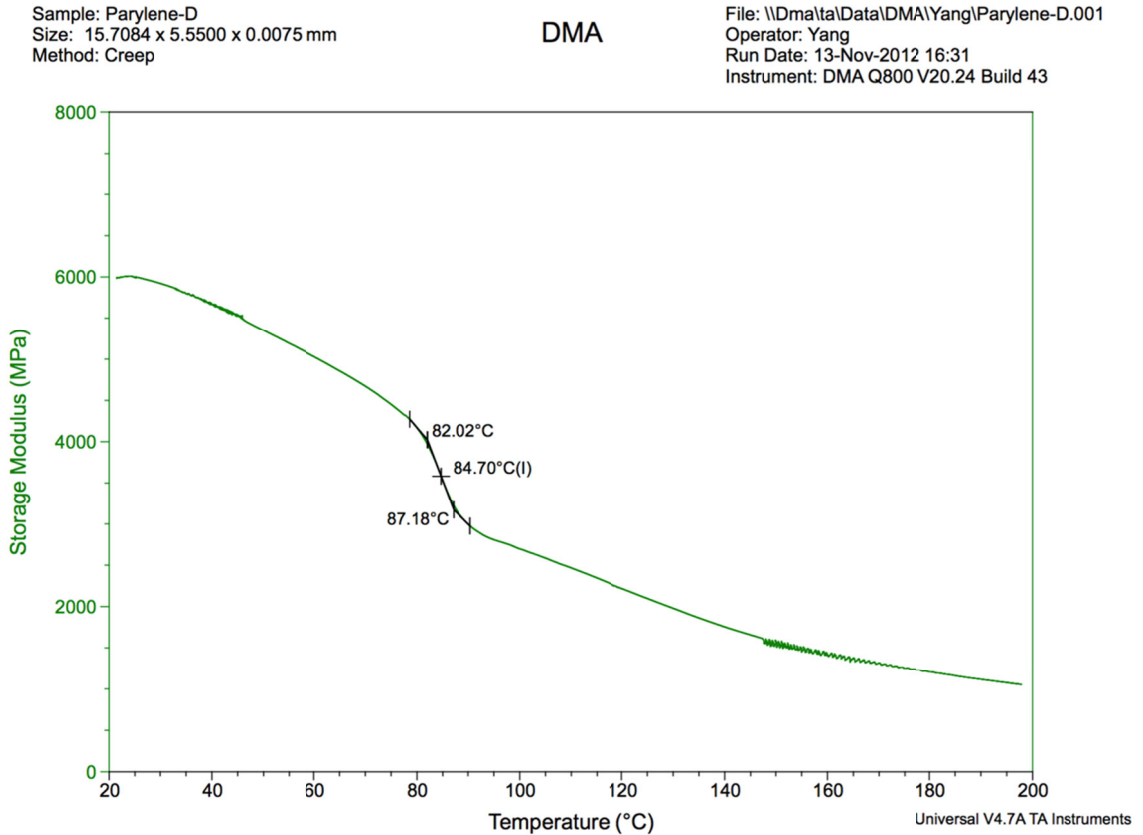
Figure 2-5. Storage modulus of as-deposited parylene-D vs. temperature.

From Figure 2-5 we can see that as-deposited parylene-D has a much higher glass transition temperature than as-deposited parylene-C, which is around 40 °C to 50 °C. Since normal human body temperature is around 37 °C, which is already around the boundary of glass transition region, the parylene-D will be more stable on mechanical properties than parylene-C. Of course one can argue that annealing of as-deposited parylene-C can easily solve this problem because annealing will increase the crystallinity thus resulting stability of properties. However, it is also important to have the material that maintains the same mechanical properties during the fabrication process and parylene-D could do a better job without an additional annealing process.
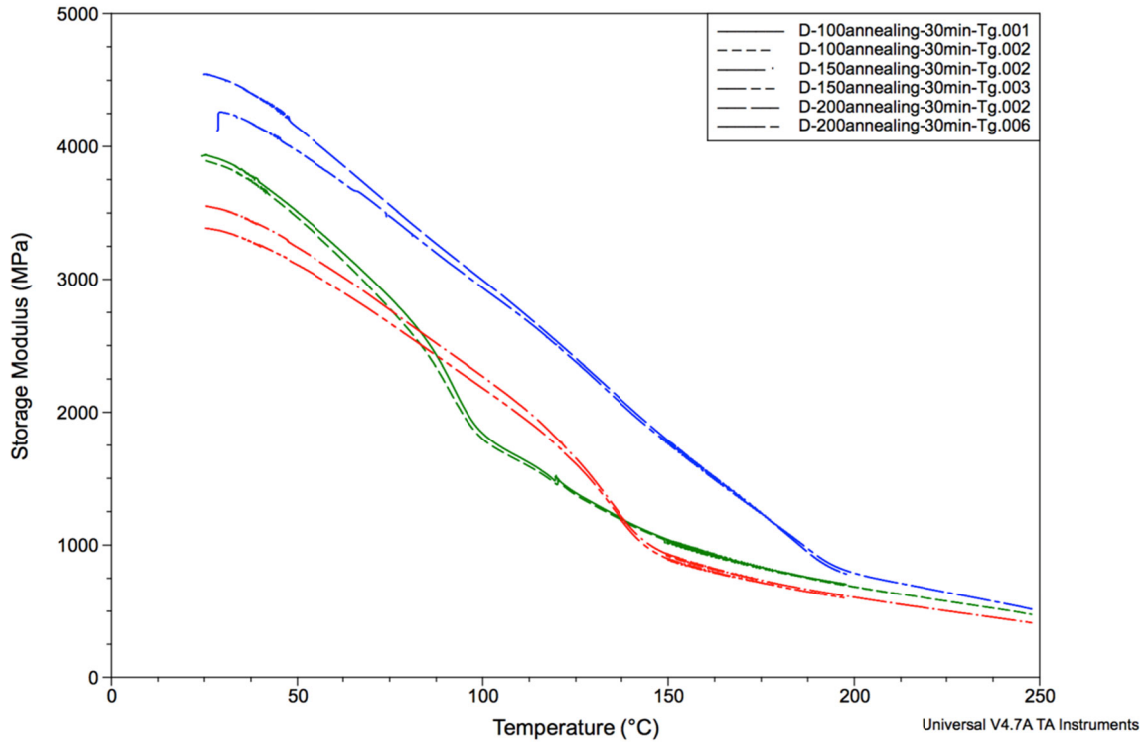
Figure 2-6. Storage modulus of 100 °C, 150 °C and 200 °C annealed parylene-D vs. temperature.

Figure 2-6 demonstrated the glass transition region of parylene-D annealed at different temperatures for 30 minutes. Two experimental lines are plotted for each condition. After annealing at 100, 150, and 200 °C for 30 minutes, the glass transition temperatures also changed to corresponding values that are close to but smaller than the annealing temperatures. It can be concluded that the change of Tg is mainly influenced by the fast progress of the crystallization of the parylene-C during the annealing progress, which happens within minutes.

To conclude, the temperature history is very important to parylene mechanical properties. Parylene-C is the most widely used biocompatible material in the parylene family nowadays; however, researchers might need to be careful about the change of the

material mechanical properties for implantable biomedical devices because that it doesn't have a glass transition temperature that is way higher than the body temperature. Also, another concern for parylene-C is that since MEMS fabrication processes will introduce high temperature, parylene-C is very likely to be annealed at some value above the Tg, which indicates the final parylene-C will not behave the same as the as-deposited one in terms of mechanical properties. Parylene-D is a very good candidate to replace parylene-C if the mechanical properties are crucial in reality because of much higher Tg. A good example to show this point is presented in the parylene-on-oil packaging for intraocular pressure sensor, where the parylene-C will cause severe sensitivity degradation while parylene-D won't [6].

2.3   Study on Parylene Surface Modification

Surface modification is important in the sense that the surface energy plays a crucial role in determine the cell and protein compatibility with the parylene surface. Research has been done on surface modification to either make the surface hydrophobic or hydrophilic [13, 14]. The contact angle of as-deposited parylene is around 80 degrees, which is slightly hydrophobic. Generally speaking there are 3 ways to make modification of the surface. The first one is by chemical or biological coatings on parylene surface. For examples, gelatin and fibronectin coating can significantly enhance the cell adherence to the surface. The second way is to design and fabricate new surface strucutures, such as dense pillars and a lotus leaf – like structure, to achieve super hydrophobicity. The third

way is plasma treatment, which creates functional groups on the parylene surfaces, thus change the surface energy. Here we will focus on the plasma treatments.

2.3.1 Motivation

The motivation to study the surface modification is that we need to come up with a biocompatible material that the CV-1 cells can attach and grow for the production of virus. Parylene is a good candidate; however, due to its hydrophobicity, the cells won't attach to it. Plasma treatments are demonstrated to solve this cell attachment problem. In the following section, different plasma surface treatments will be discussed.

2.3.2 Plasma Treatments

Here we tested two gas sources, the oxygen and ammonia gas, and their combinations. Table 1 summarizes all different recipes. 7-micron parylene-C was firstly coated on 4-inch wafers and plasma was applied for each wafer.

Table 2-1. Plasma treatment receipes for parylene-C

A	50 Watt 200 mTorr 3 min O2
B	50 W 200mT 3 min O2, then
	50 W 200mT 3 min NH3
C	50 W 200mT 3 min NH3
D	50 W 200mT 3 min NH3, then
	50 W 200mT 3 min O2

E   50 W, 205mT O2 + 25 mT NH3, 3 min

F   No treatment, only PA-C coating

CV-1 cell growth was also tested to see the optimized recipe, as shown in Figure 2-7. 1.00E5 Cells were seeded on day 0 and were trypsinized and counted everyday to get the cell growth data. Recipe G is the original commercial cell culture plate.
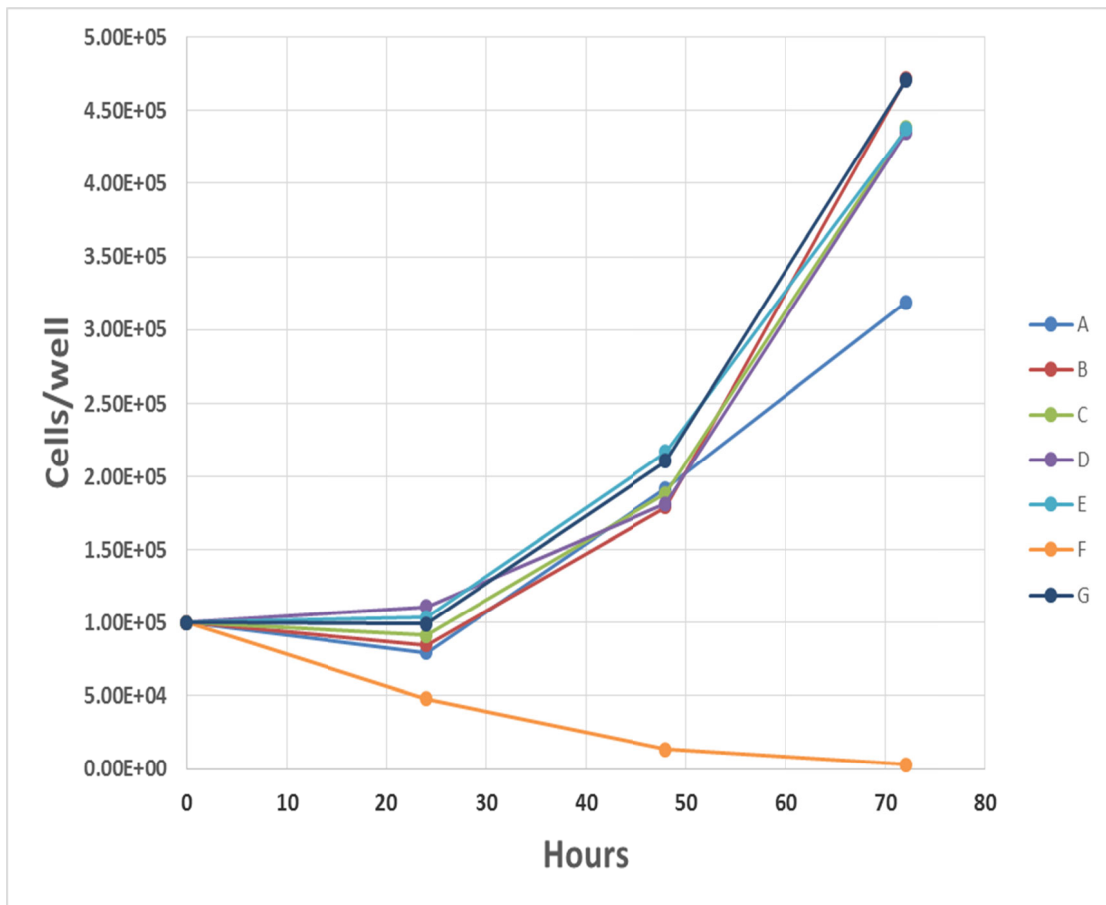
Figure 2-7. CV-1 cell growth for each recipe

From this data we can clearly see that recipe B is the best, which is even better than the original cell culture plate. It can be explained by the theory that oxygen plasma can roughen the surface the parylene by etching, besides forming functional groups [15].

Then the ammonia gas can further binding to the roughened surface, while in other recipes, oxygen is competing with ammonia gas in binding to the surface, and the data reveals that CV-1 cells don't attach to parylene without plasma treatment (F).

2.4 Summary

Properties of parylene are studied and discussed in this chapter. Characterizations are important because the behaviors of parylene could potentially have a large impact on the total functionality of the whole device. Both mechanical properties and surface properties are presented. For the mechanical properties, DMA methods are applied to demonstrate the tensile tests and glass transition temperature tests for various parylene samples under different conditions. The conclusion is that parylene-C has good mechanical properties in general. However, temperature history needs to be documented and considered if mechanical properties of parylene are crucial. Parylene-D is a good replacement of parylene-C because it has a much higher glass transition temperature. For surface properties, plasma treatments are discussed and the application in cell culture is presented. Oxygen plasma combined ammonia gas plasma can treat the surface good enough for CV-1 cells to attach and grow at a speed even faster than ordinary culture dish, whose surface has also been treated. Through of discussion of the parylene characterizations, better understanding of the material is gained which can greatly benefit the fabrication of parylene devices. Details of these devices will be presented in the following chapters.

2.5 Reference

[10] J. Lin, MEMS for glaucoma, Dissertation (Ph.D.), California Institute of Technology, 2012

[11] G. W. Ehrenstein and R. P. Theriault, Polymeric materials: structure, properties, applications. Munich; Cincinnati, OH: Hanser; Hanser Gardner Publications, 2001

[12] K. P. Menard, Dynamic mechanical analysis: a practical introduction. Boca Raton, FL: CRC Press, 2008.

[13] T.Y. Chang, V.G. Yadav, S. De Leo, A. Mohedas, B. Rajalingam, C.L. Chen, S. Selvarasah, M.R. Dokmeci and A. Khademhosseini, Cell and protein compatibility of parylene-C surfaces, *Langmuir*, vol. 23, pp. 11718-11725, 2007

[14] C.L. Chen, S. Jinno, H. Moller, B. Rajalingam, S.H. Chao, S. Selvarasah, A. Khademhosseini and M.R. Dokmeci, Multilayer parylene-C stencils for dynamically controlling cell interactions, *Proc. of MEMS 2008*, Tucson, AZ, USA, pp. 276- 279, 2008

[15] B. Lu, Parylene as a new membrane material for biomems applications, Dissertation (Ph.D.), California Institute of Technology, 2012

3 PARYLENE MAGNESIUM-EMBEDDED FILTER FOR CIRCULATING TUMOR CELLS ISOLATION

3.1 Introduction

Cancer has been a huge threat for human lives so that cancer detection has been an important research fields for both scientists and engineers in related areas. Cancer is not a single disease. It is a group of diseases that have a common characteristic, which is extremely fast cell growth without control. There is a possibility that the cells may spread to other parts of the body. The spreading process then involves circulating tumor cells (CTCs) so it is important to study the capturing of CTCs as well as isolation. In this chapter, a novel device, Parylene magnesium-embedded filter will be introduced and discussed, including material selection, device design and fabrication, results, and discussion.

3.2 State-of-art CTC Detection Methods

Circulating tumor cells (CTCs) are cells that slough off the edges of a primary tumor and are swept away by the bloodstream or lymphatic system into the vasculature [16]. They constitute seeds for subsequent growth of additional tumors in vital distant organs, triggering a mechanism that is responsible for the vast majority of cancer-related deaths. Thus CTCs in peripheral blood have been investigated as a valuable biomarker for patients with various types of cancers [17-20]. However, CTCs are difficult targets to probe owing to their extremely low concentration in peripheral blood (usually around 100 cells/mL of blood) [21]. Although rare, CTCs represent a potential approach for the detection, characterization, and monitoring of non-haematologic cancers. Therefore, CTCs capture from whole blood has been identified to be an unmet need for cancer research and effective cell separation methods are required to facilitate the study of CTCs.

State of art CTC isolation techniques can be divided into two categories. One is depended on antibodies against epithelial cell-adhesion molecule (EpCAM) [22, 23], a protein that sticks out of the outer surface of CTCs, but not healthy blood cells. S. Nagrath etc. [22] have successfully identified CTCs in the peripheral blood of patients with metastatic lung, prostate, pancreatic, breast, and colon cancer in 115 of 116 (99%) samples with a range of 5–1,281 CTCs per ml and approximately 50% purity. However, this method relies on immunomagnetic binding of cell surface EpCAM, an expensive approach that is limited to EpCAM-expressing tumors [24]. The binding of antibodies to EpCAM may induce cytotoxicity, thus altering the original state of CTCs and reducing the reliability of further biological research [25]. Furthermore, the EpCAM-antibody

capture method will require some biochemical ways to break lose the CTCs and a safe method that doesn't harm the CTCs is yet to be proven.

The other methods are antibody-independent [25-28], such as size-based MEMS filters [28, 29]. Because CTCs are generally larger than white blood cells (WBCs), a size-based filter can divide the cell types. Our previous paper described a parylene-C microfilter platform driven by constant low pressure to capture live CTCs from prostate cancer patient blood [28]. We showed that the captured cells could be lysed for telomerase activity detection assays as few as 25 cells added into 7.5 ml blood and the captured cells could proliferate either on or off the filter [28]. Moreover, we successfully integrated this device into a Phase III multi-center clinical trial and showed that in patients with more than 5 CTCs, telomerase activity assayed from microfilter-enriched cells was prognostic of overall survival [30].

3.3 Motivation

Despite its success, the microfilter platform has been limited by the persistence of contaminating peripheral WBCs attached to the filter. These residual background cells are of particular concern when attempting to analyze CTC RNA expression. In order to recover totally pure CTCs (no WBC background), we next adopted a motorized micromanipulator pipette to pick a single cell from the microfilter, but we observed that the cells captured on the filter could not be released easily.

To address this challenge, we thought of magnesium (Mg) etching: thin-Mg film is proved highly biocompatible and can be etched in salt-contained mediums such as Dulbecco's Modified Eagle Medium (DMEM) [31]. In this study, we developed a novel

design applying a buried sacrificial Mg layer underneath the original microfilter. After filtration, the filter was immersed in DMEM. When the thin-film Mg was dissolved, the cells were released. This technique does not require any additional chemical, which might damage or change the cells and disrupt further analysis. The detailed design, fabrication, and testing results will be given in the following sections.

3.4 Magnesium: A Sacrificial and Biodegradable Material

Magnesium (Mg) element has lots of desirable properties for biomedical device applications, especially mechanical and electrochemical characteristics. More specifically, the most important advantages of Magnesium as a temporary biomaterial are: first of all, magnesium's density is 1.74 g/cm^3, which is a great lightweight metal. It is much less than that of Ti alloy (4.4–4.5 g/cm^3). More importantly, this value is very close to that of the bone (1.8– 2.1 g/cm^3) [32]. Secondly, from the mechanics point of view, the Young's modulus of magnesium is 41–45 GPa, which is close to the value of the bone; therefore the application of magnesium can potentially avoids the stress shielding issues [33]. The third point is that magnesium is very important to metabolism. Also it is the fourth most abundant element inside human body. Meanwhile magnesium is an important part for lots of enzymes, as well as RNA and DNA. The last but also the most crucial point is that the electro potential of magnesium is -2.37 V and magnesium demonstrates very low corrosion resistance in Cl$^-$ containing liquid environment. All in all, magnesium has a strong potential to be developed as a biomaterial, particularly for the applications where fast dissolving speed is preferred.

On the other hand, magnesium can potential be totally compatible with traditional MEMS fabrication technologies and acting as a sacrificial metal layer for various different kinds of BioMEMS devices. This means that magnesium could be an interesting dual "sacrificial and biodegradable MEMS material". It also can have a great potential to be applied to many parylene-based devices for implant applications. There are several advantages of magnesium over traditional photoresist as a material for sacrificial layer. For instance the thickness can be much more precisely controlled due to different fabrication processes, and the biodegradability that the sacrificial layer can be dissolved in any Cl^- contained liquids, such as PBS, cell culture medium, and saline, etc. with a relatively fast dissolving speed. Detailed fabrication processes will be discussed thoroughly in the following subsection: Magnesium processing technologies.

3.4.1   Magnesium Processing Technologies

Traditional Magnesium processing technologies in MEMS field mainly includes three ways of preparation of thick-film, which is thicker than 10μm includes laser cutting (Laminates magnesium foil onto glass substrate first and laser cut out of patterns followed by residue removal), electrochemical etching (of commercial magnesium foil), and electrodeposition (of magnesium). Nevertheless, all the three techniques mentioned above are targeting at magnesium film that are thick and there's few reported work on thin-film (submicron) magnesium for MEMS applications. Therefore, we explored the process of Ebeam-deposited "thin-film" magnesium.

Ebeam deposition belongs to Physical vapor deposition (PVD), which happens in vacuum and produces a thin film on substrates (in our application, the substrate is silicon

or parylene) by depositing thin layers of metals. Electrical field focuses the electrons on the metal, which is inside a crucible. The crucible is made of high temperature standing materials. The electron hits the metal surface, transforming its energy into heat. Metal will melt in the crucible and evaporate afterwards. A thin-film metal will be deposited on the substrate, which is on the top of the vacuum chamber. A rotating system is designed for better thin film uniformity. Sub-micron thick film can be achieved. For different metals, because of their difference in melting points, the power required is also different. Also the deposition speed given certain power is also different.

Like other sacrificial metal layers such as Al and Ni, Mg thin films can be prepared by Ebeam evaporation and deposition because of its low melting temperature (~650°C). High-purity Mg pellets are also readily available. In this work, 0.06, 0.3, and 1.0-µm-thick Mg films are deposited on 4-inch silicon wafers.

Table 3-1: Comparison of preparation methods, etchants, and etching rates of Mg, Al, and Ni.

	Preparation methods	Etchants	Etching rates
Mg	Evaporation (30% power, 2.5 Å/sec)	hydrogen chloride	3700 Å/sec·M
		Saline	4.7 Å/sec
Al	Evaporation (47% power, 4.5 Å/sec)	Al etchant Type A (Transene©)	100 Å/sec at 50°C
Ni	Evaporation (45% power, 4.0 Å/sec)	Ni etchant TFB (Transene©)	30 Å/sec at 25°C

The comparisons of deposition methods of magnesium over other commonly used metals are listed in Table 3-1. In brief, it compares the typical deposition rates, etching rates, and etchants of Mg, Al, and Ni. It shows the deposition rates are similar among the popular sacrificial metals but Mg has a much higher etching rate. Etching properties will be discussed in the following subsections.

3.4.2   Parylene Microchannels with Magnesium Sacrificial layer

To study the etching properties of magnesium, both vertical etching sample (Figure 3-1) and channel undercut [34] sample (Figure 3-2) are designed. In vertical etching method, etching chemicals can be sufficiently supplied to the etching front so it's for the measurement of reaction-limited etching rates. Therefore, the etching time can be calculated using just the reaction-limited etching rate. However, if the etching length is long such as in channel etching, reactive chemicals at the etching front may be depleted. The etching rate then is dominated by diffusion mechanism. As a result, a good model has to include both chemical reaction and diffusion. In addition, such a model should also be applicable to a wide range of concentrations. A model that satisfies all these criteria will thereafter be a universal model. Here we have tested etchants including diluted HCl, saline, and culture medium. Although a lot more work needs to be done, the initial results do show that thin-film Mg indeed is a promising dual sacrificial and biodegradable material.

The vertical etching samples (Figure 3-1) are then prepared with exposed etching windows in a 5-µm-thick photoresist. In this case, etching chemicals can be sufficiently supplied to the etching front so it's for the measurement of reaction-limited etching rates.

We have also obtained the first diffusion-limited etching data of Mg using the channel-undercut method. Sacrificial Mg strips are designed to be 10 μm wide. 5-μm-thick photoresist is then spin-coated and patterned (Figure 3-2a&b). In this case, diffusion is an important factor to slow down the etching. All experiments are conducted at room temperature.
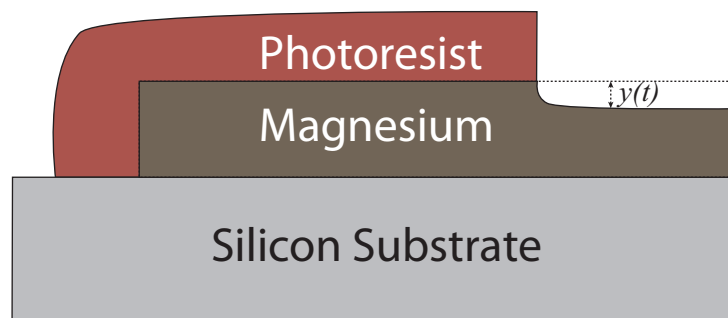
Figure 3-1. Schematic view of magnesium vertical etching samples
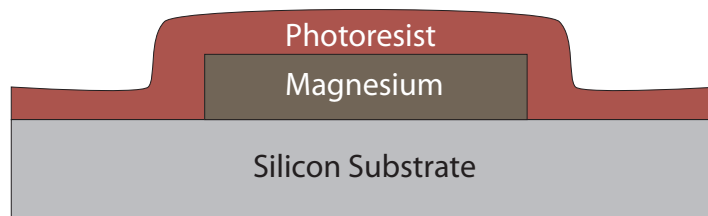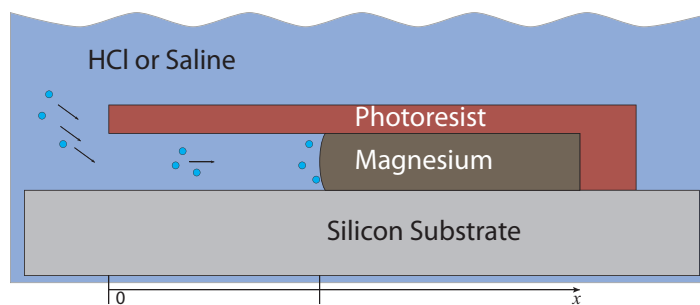
Figure 3-2. (a) Cross-section view of microchannel etching samples; (b) Schematic of etching sacrificial magnesium to form microchannel.

3.4.3 Study of Thin-film Magnesium Etching Properties

3.4.3.1 Vertical etching results

Figure 3-3a shows the etched Mg thickness versus time with various HCl concentrations in the reaction-rate-limited condition. The dependence of magnesium etching rates on HCl concentrations are plotted in Figure 3-3b and a rate of 0.37μm/s·M is obtained.
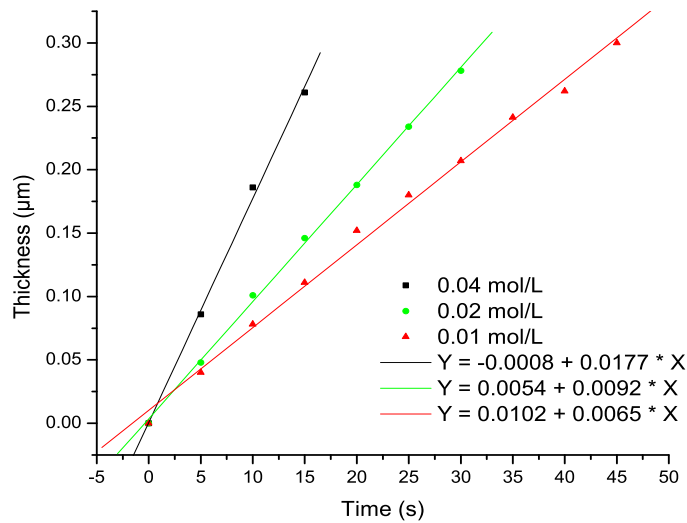
(a)
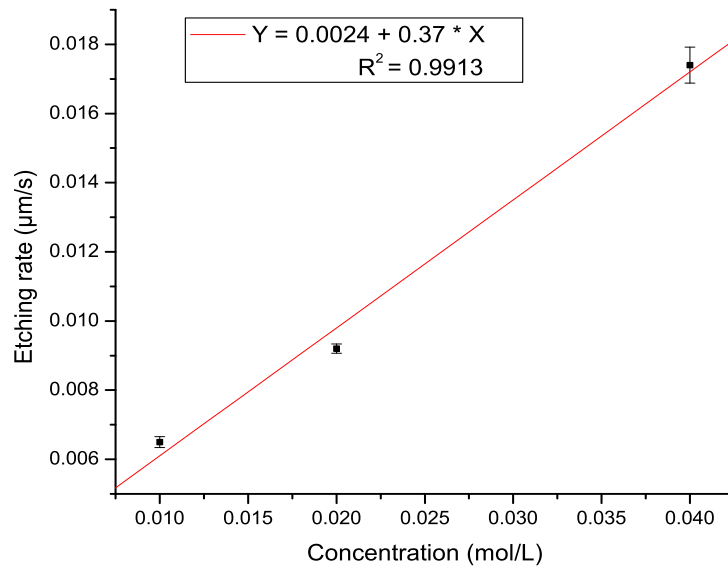
(b)

Figure 3-3. (a) Magnesium thickness versus time of etching in different hydrogen chloride concentrations (b) Magnesium etching rate versus hydrogen chloride concentration.

3.4.3.2   Etching model of sacrificial Mg channel

Figure 3-2b shows the schematic of etching sacrificial magnesium to form microchannel. In order to study the model, firstly we need to make following assumptions: the diffusion coefficient is constant, the heat generation during reaction is negligible, convection is negligible, and the etching process is one-dimensional. Table 3-2 shows all variables and coefficients in the model.

Table 3-2. Coefficients in the etching model.

Symbol	Expression
C	Concentration of reaction chemical

C_b	Bulk reaction chemical concentration
C_s	Etching front chemical concentration
u	Flow velocity
x	Etching length
D	Diffusion coefficient
J	Diffusive flux
t	Time
M	Molar mass
ρ	Density
k_1, k_2	Constants
a, b, e, f	Intermediate variables

Using the coordinates defined in Figure 3-2b, the continuity equation is,

$$\frac{\partial C}{\partial t} + u\frac{\partial C}{\partial x} = D\frac{\partial^2 C}{\partial x^2} \tag{1}$$

Neglecting convection, (1) becomes,

$$\frac{\partial C}{\partial t} = D\frac{\partial^2 C}{\partial x^2} \tag{2}$$

According to Fick's first law,

$$J = -D\frac{\partial C}{\partial x} \tag{3}$$

Assume the chemical reaction is

$$Mg + 2HCl \rightleftharpoons MgCl_2 + H_2\uparrow$$
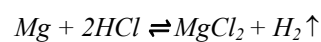
In a stoichiometric reaction,

$$J[Mg] = \frac{1}{2} J[HCl] \tag{4}$$

The etching rate is proportional to $J[Mg]$ at the etching front,

$$\frac{dx}{dt} = J[Mg] \frac{M[Mg]}{\rho[Mg]} \tag{5}$$

From (4) and (5),

$$\frac{dx}{dt} = \frac{1}{2} J[HCl] \frac{M[Mg]}{\rho[Mg]} \tag{6}$$

The other boundary conditions are,

$$C(0,t) = C_b \tag{7}$$
$$C(x(t),t) = C_s \tag{8}$$

In the combined First-and-Second model, the HCl concentration distribution is linear (9), and the reaction rate includes both a first and second order term (10),

$$J[HCl] = \frac{D(C_b - C_s)}{x} \tag{9}$$
$$J[HCl] = k_1 C_s + k_2 C_s^2 \tag{10}$$

Solving (9) and (10), we have,

$$J[HCl] = \frac{1}{2k_2} (\frac{D}{x})^2 [1 - a + (k_1 + 2C_b k_2)(\frac{x}{D})] \tag{11}$$

in which,

$$a = \sqrt{1 + (\frac{k_1 x}{D})^2 + 2(k_1 + 2C_b k_2)(\frac{x}{D})} \tag{12}$$

Substitute Eq. (11) into (6), one has,

$$\frac{dx}{dt} = b(\frac{D}{x})^2 [1 - a + (k_1 + 2C_b k_2)(\frac{x}{D})] \tag{13}$$

in which,

$$b = \frac{M[Mg]}{4k_2 \rho[Mg]} \tag{14}$$

By integrating (13) from time 0 to t, we have t=F(x),

$$t = \frac{D\{ae + 2k_1^2 \frac{x}{D} + (k_1 + 2C_b k_2)[(\frac{k_1 x}{D})^2 - 1]\}}{8bC_b k_1^2 k_2 f} - \frac{D}{2bk_1^3} \log \frac{k_1 a + e}{2f}$$

(15)

where

$$e = k_1 + k_1^2 \frac{x}{D} + 2k_2 C_b$$

(16)

$$f = k_1 + k_2 C_b$$

(17)

k1, k2, and D are determined by experiments of sacrificial Mg channel etching.

3.4.3.3 Sacrificial Mg channel etching results

Figure 3-4 shows the etched channel length versus time for different HCl concentrations. The initial etching rates derived from Figure 3-4 further verify the data from Figure 3-3. For instance, the etching rate for 0.04 mol/L HCl is 1.77E-2 µm/s (Figure 3-3b) while the initial etching rate from Figure 3-4 is 1.51E-2 µm/s. Coefficients k1, k2 and D can be determined experimentally. Nonlinear least squares fitting (NLSF) method, which is based on the Levenberg-Marquardt (LM) algorithm is used to fit Eq. (15) to experimental data, and results are shown in Figure 3-4. This model fits all data using k1 = 9.33E-3 cm/sec, k2 = 275.71E3 cm4/mole·sec and D = 3.86E-6 cm2/sec.
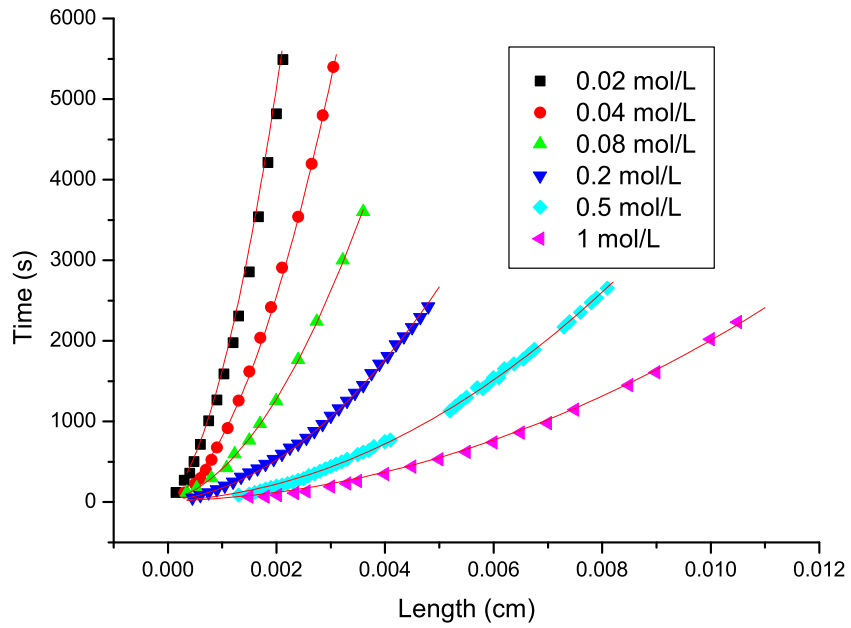
Figure 3-4. 1-µm-thick Mg Etched microchannel length versus time for different

hydrogen chloride concentrations.
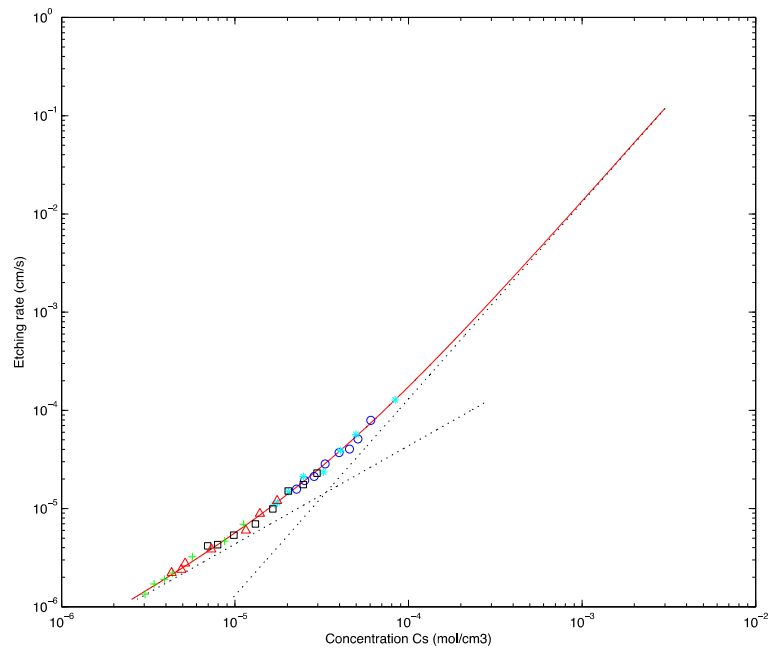
Figure 3-5. Mg etching rate dependence on concentration Cs. Solid line represents the combined first-and-second order model. Dotted line represents first or second order only.
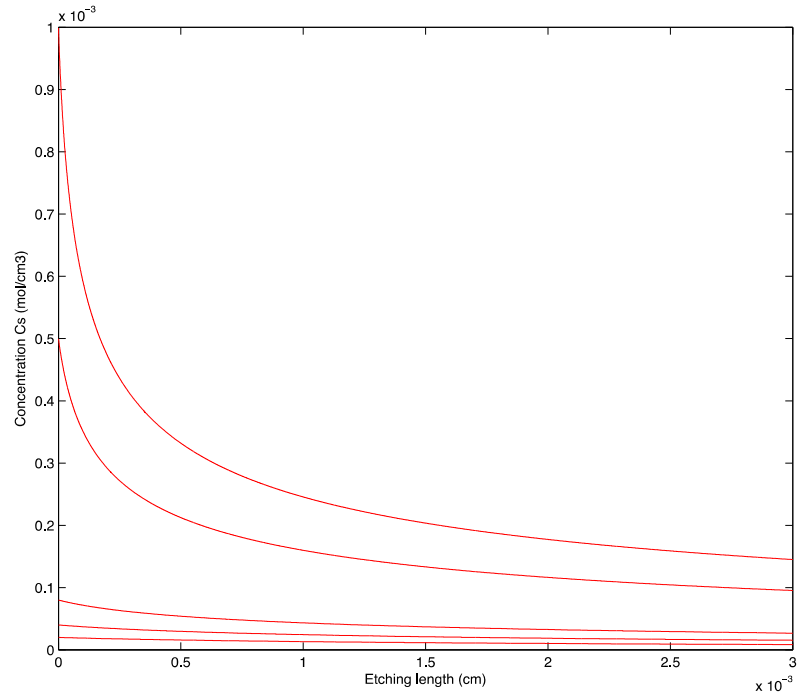
Figure 3-6. Concentrations of reactant at the etching front. Bulk concentration is the value of Cs when depth equals 0. Higher bulk concentration drops faster.

Figure 3-7 then shows the thickness effects using three different thicknesses (i.e., 0.06, 0.3 and 1.0 μm) of Mg in 0.04M HCl. The results show that the undercut rates for the thicker channels are bigger than the thinner ones. The result is consistent with [34].
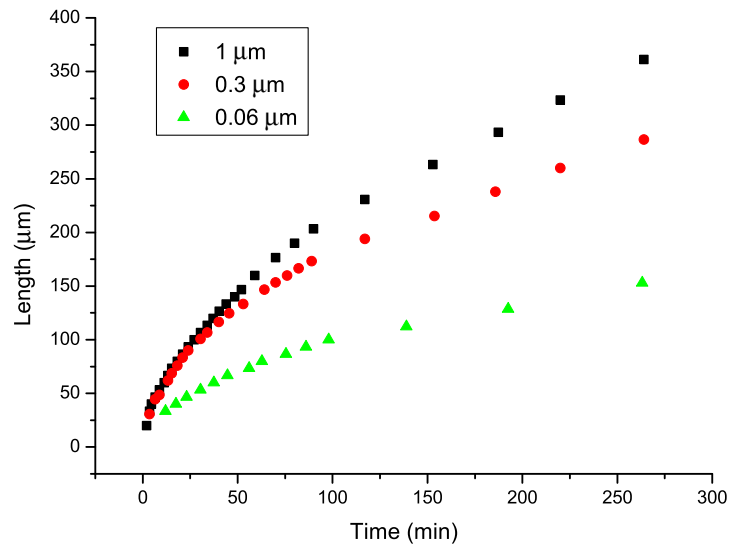
Figure 3-7. Microchannel etching length over time for three different thicknesses of

magnesium in 0.04M HCl.

The hypothesis is that the etching chemical (i.e., Cl^-) interacts with the inner photoresist surface so the overall effective diffusion constant is reduced. In the future, one should consider the thickness effects if Mg is thinner than 0.06μm or thicker than 1μm.

Figure 3-8 shows the etching of 1-μm-thick Mg microchannels to form in 0.04 mol/L hydrogen chloride at different time intervals.

48

(a)   (b)
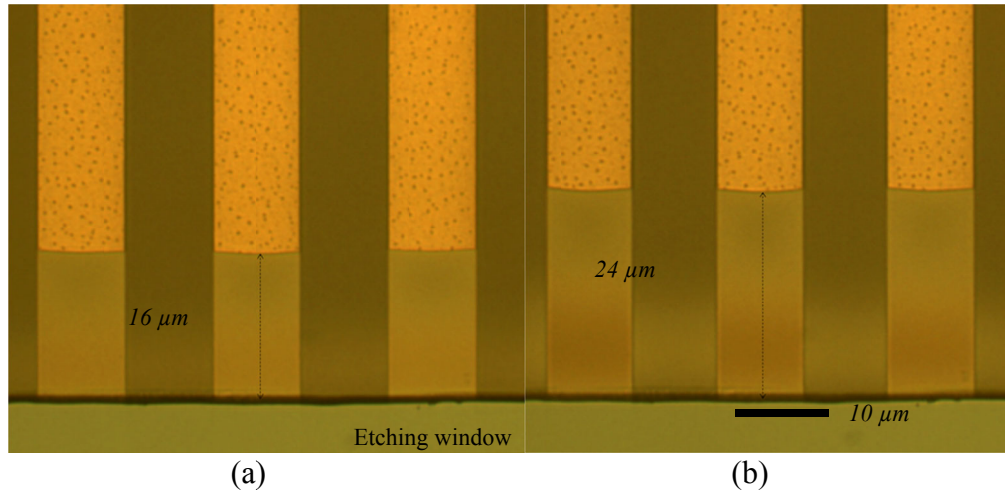
Figure 3-8. Photographs of etching 1 μm thick magnesium to form microchannels in 0.04 mol/L hydrogen chloride: (a) after 30 min; (b) after 60 min.

3.4.3.4 Biodegradable etching results

In addition to sacrificial etching, biodegradable etching in saline and culture medium is also demonstrated here. Figure 3-9 shows the etched length of microchannel versus time in saline.
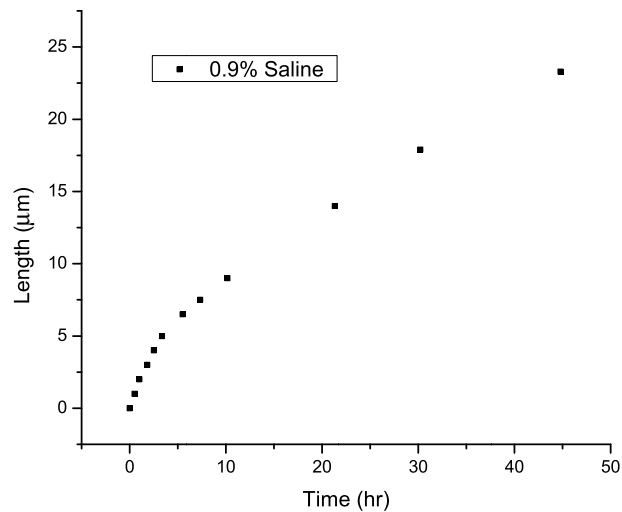
Figure 3-9. (a) Microchannel etching length over time in 0.9 wt% saline.

Figure 3-10 then shows the open-surface Mg etching rates in saline and Dulbecco's modified Eagle medium (DMEM, a cell culture medium) mixed with FBS and PBS. The chloride ion concentrations are 0.15M in saline and 0.11M in DMEM, and the resulting etching rates are 1.7 and 1.27μm/hr respectively. The results show that the Mg biodegradation depends mainly on chloride ion concentration and has a converged rate of ~11.4μm/hr·M. Note that this rate is much faster than other widely-used biodegradable polymer materials such as PLA. For instance, the degradation time for PLA/PLGA (50:50) is only about 0.2μm/hr (i.e., 10 weeks of biodegradation time for microspheres of 100μm in diameter).
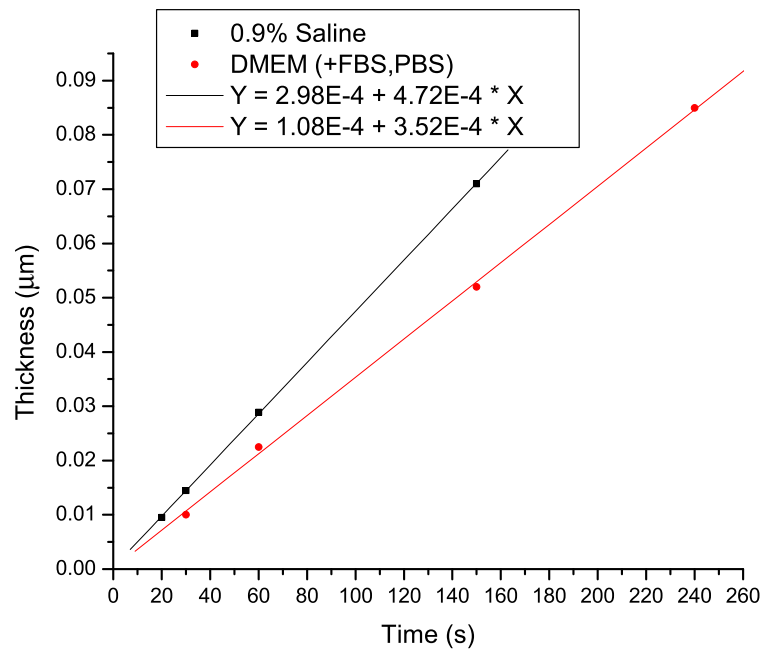
Figure 3-10. Thickness change over time in 0.9% saline and DMEM.

3.4.3.5 Conclusions

This work reports the first etching tests of thin-film Mg in diluted hydrochloric acid (HCl), saline, and culture medium. Both vertical etching and sacrificial Mg microchannel etching methods are applied to study the etching properties. Data of sacrificial Mg microchannel etching are fitted by the combined first-and-second order model. The initial results do show that thin-film Mg is a promising dual sacrificial and biodegradable material in MEMS application.

3.5 Parylene Magnesium-embedded Filter

3.5.1 Introduction

Circulating Tumor Cells (CTCs) are rare cancer cells that are shed by tumors into the bloodstream and can be valuable biomarkers for various types of cancers. However, CTCs captured on the filter could not be released easily using the existing CTC analysis platforms based on size. To address this limitation, we have developed a novel Magnesium-embedded cell filter for capture, release, and isolation of Circulating Tumor Cells (CTCs). The CTC-filter consists of a thin Ebeam-deposited Magnesium (Mg) layer embedded between two parylene-C (PA-C) layers with designed slots for filtration and CTC capture. Thin Mg film is proved highly biocompatible and can be etched in saline, PBS and Dulbecco's Modified Eagle Medium (DMEM) etc., properties that are of great benefit to help dissociate the filter and thus release the cells. Finite element method (FEM) analysis was performed on the Mg etching process in DMEM for the structure design. After filtration process, the filter was submerged in DMEM to facilitate Mg

etching. The top PA-C filter pieces break apart from the bottom after Mg completely dissolves, enabling captured CTC cells to detach. The released CTC can be easily aspirated into a micropipette for further analysis. Thus, the Magnesium-embedded cell filter provides a new and effective approach for CTCs isolation from filter, making this a promising new strategy for cancer detection.
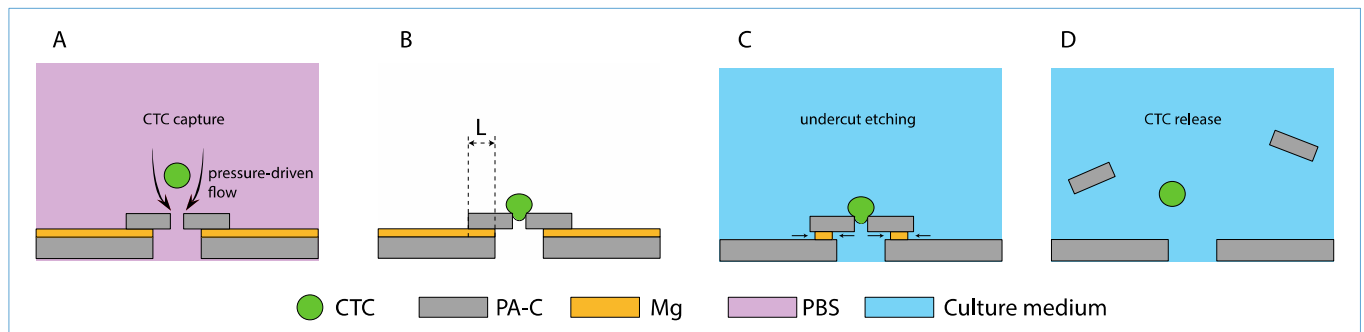
Figure 3-11. Schematics of Mg-embedded CTC filter filtration, Mg dissolving as well as CTC release. A, The CTC gets captured during filtration, B, The CTC deforms and gets stuck in the filter slot, C, The Mg sacrificial layer is going through undercut etching in DMEM, D, The filter pieces separate and the CTC cell is released.

3.5.2 Design

In this section, the design of the whole device, as well as the experiments, is discussed in detail, including structural design and analysis.

3.5.2.1 Structure design

T. Xu etc. have discussed the optimization of the CTC filter slot size in [28]. Here in this work, we followed the optimized design proposed. The top PA-C slot width is 6 μm while the top PA-C slot length is 40 μm. The bottom parylene thickness is 10 μm and

the top is 5 µm. The total filter size is 6 mm by 6 mm, same as in [28]. Figure 1A shows the cross-sectional view of single Mg-embedded filter slot while Figure 3-12 illustrates the top view of the whole filter membrane.

Total filter size: 6 mm by 6 mm
PA-C slot width: 6 µm
PA-C slot length: 40 µm
PA-C membrane thickness: 10 µm (bottom) + 5 µm (top)

40 µm
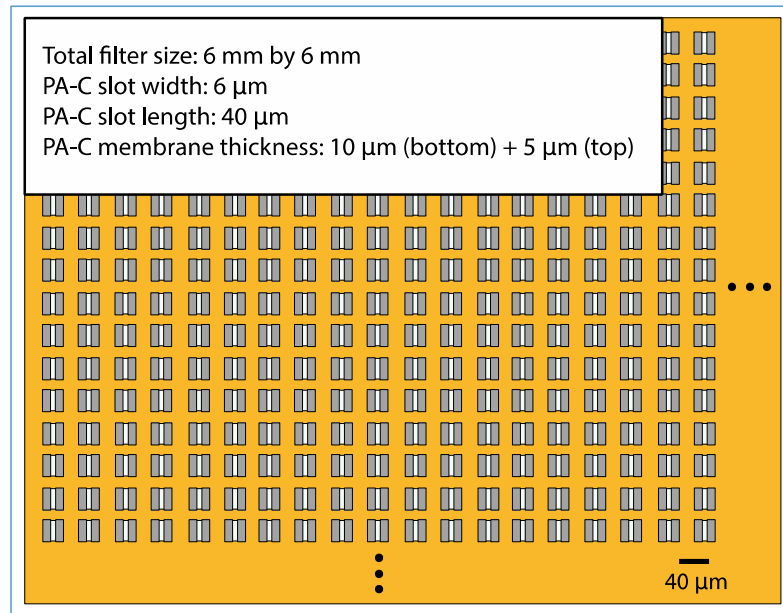
Figure 3-12. Schematic of Mg-embedded filter membrane (top view) with all the structure dimensions shown on the upper-left corner.

3.5.2.2 FEM Analysis

As indicated in the schematic of Figure 3-11, Mg sacrificial layer was sandwiched between top and bottom parylene. Thus the undercut etching happened on both open ends towards the inside (Figure 3-11C). The undercut etching is a complicated process that combines not only chemical reaction, but also diffusion of reactants from the bulk liquid to the etching fronts [34]. Therefore it is not straightforward to calculate the dissolving time of any given Mg etching length, which is "L" in Figure 3-11B. To have a reasonable Mg dissolving time in DMEM after CTC capture, for instance 2.5 hours, FEM analysis was performed to find out the structure design parameters, especially the value of "L". In

order to run FEM analysis, the etching reactants as well as chemical reaction principle were studied beforehand.
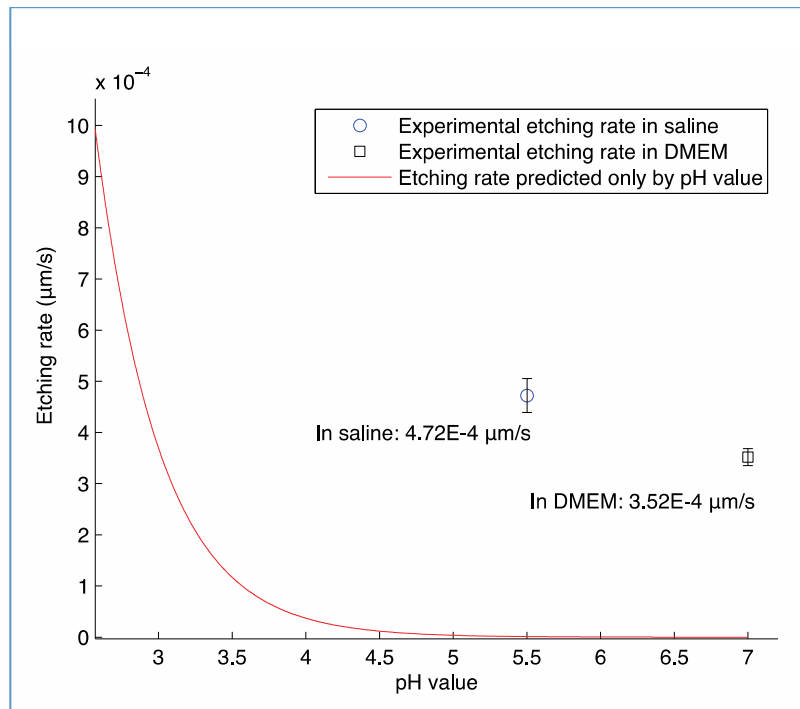
Figure 3-13. Etching rate dependence on pH value. Experimental data in saline and DMEM are much bigger than the pH value model predicted, and thus Mg corrosion is the dominating process for salt-containing medium.

Figure 3-13 shows the Mg etching rate (in μm/s) in relationship with the pH value of the solutions. The blue circle and the black square are experimental data of etching in saline and DMEM respectively, while the red line is the etching rate predicted only by pH value, following the equation:

Etching rate (μm/sec) = 0.37 (μm/sec·M) · concentration of [H+] (M) (1), where 0.37 μm/sec·M were experimentally discovered in [10] with pH value ranging from 0 to 2, where the dominating chemical reaction is as simple as:

$$Mg + 2H^+ \rightarrow Mg^{2+} + H_2\uparrow$$
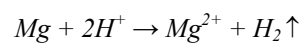
Therefore, assume etching rate is y and pH value is x, equation (1) becomes $Y =$ $0.37 * 10^{-X}$, which was plotted as the red line.

Interestingly, the practical etching rates in saline (4.72E-4 μm/sec) and DMEM ((3.52E-4 μm/sec) are much faster than what the red line predicts (1.17E-6 μm/sec and 3.70E-8 μm/sec respectively). It indicates that pH is no longer the dominating factor for biodegradable etching study. Here we purpose that corrosion accelerates the etching speed as an electrochemical Process. The oxidizing Mg supplies electrons and the electrons can move through the sodium cation to the oxygen that dissolved in the solution. In this case redox reaction happens between Mg and the oxygen. This etching process is likely to be dominated by corrosion principle, other than pH value. Therefore oxygen dissolved in water should be treated as the reactant.

Figure 3-14 shows the region of embedded Mg to etch is sandwiched between top and bottom PA-C, the geometry of which is set to be 1 μm (thickness) by 6 μm (width) by 40 μm (length). As shown in Figure 3-11C, side etching happens at both ends of the channel. The case has been simulated in 2D on the cross-section of 1 μm by 6 μm, with the following parameters:

Table 3-3: Coefficients for simulation

Parameters	Values
Initial oxygen concentration	0.26 mol/m^3
Oxygen diffusion coefficient	2.1E-9 m^2/s
Mg density	1740 kg/m^3
Mg Molar mass	0.02345 kg/mol

Initial reaction rate	3.52E-10 m/s

The Moving mesh (ALE) method was applied to simulate the deformation of Mg boundary over time. Automatic Remeshing was turned on to remesh after each step of combined etching and diffusion process. The dynamic simulation results of embedded Mg etching front are presented in Figure 3-14. The etching process ends after 8523 seconds in simulation, which is 2.36 hours. It is a reasonable number for the Mg to totally dissolve. The bars indicate the concentration of oxygen, ranging from 0.25 mol/m3 to 0.26 mol/m3. There is little change in the concentration of oxygen between the etching front and the bulk solution, which implies 6-μm etching length is short enough so that diffusion doesn't limit the etching rate much. Since the FEM simulated etching time is neither too short nor too long, 6 μm was set to be the etching length for the design of the Mg-embedded filter.
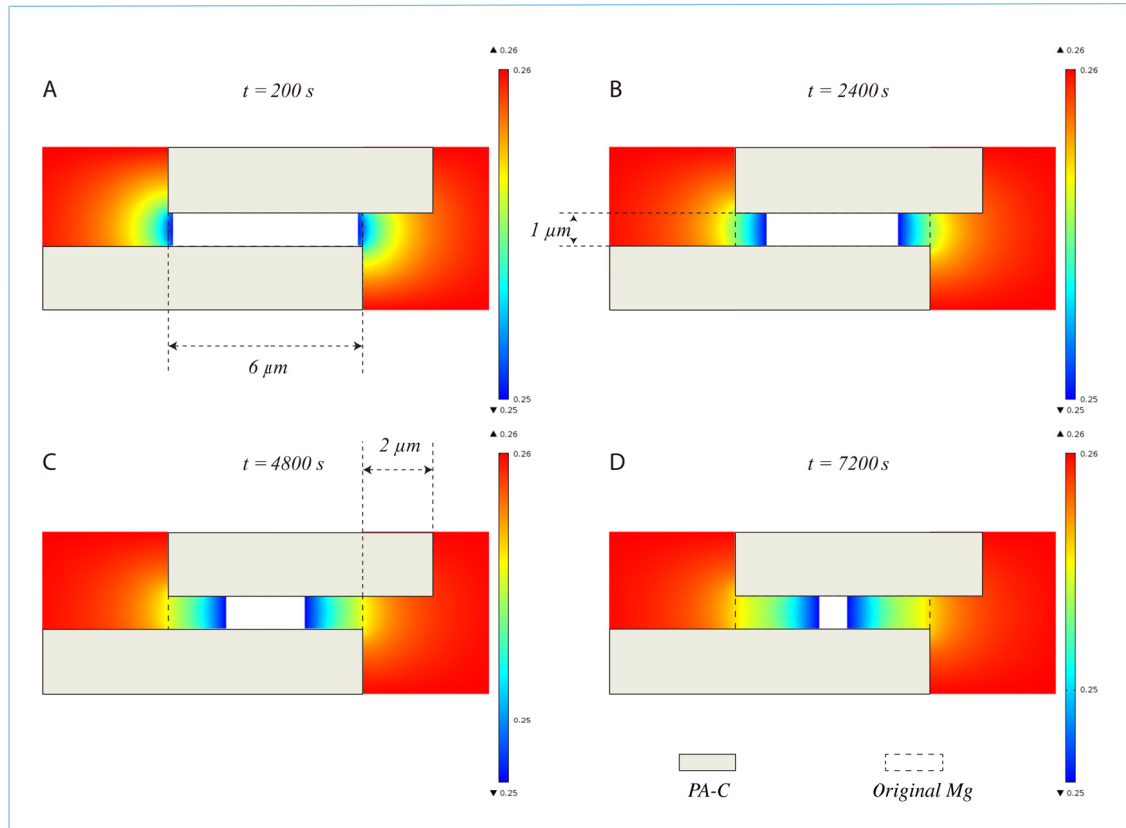
Figure 3-14. FEM analysis on etching process of sacrificial Mg sandwiched between top and bottom PA-C layer for an Mg-embedded filter design, the geometry of which is set to be 1 μm (thickness) by 6 μm (width). A, B, C, D show the Mg etching progress, as well as oxygen concentration distribution at 200 s, 2400 s, 4800 s and 7200 s respectively. Simulation results predicted that Mg etching process would finish after 8523 seconds, a reasonable number so that 1 μm (thickness) by 6 μm (width) were set to be the design of the Mg-embedded filter.

3.5.3 Fabrication Methods

The Mg-embedded CTC filter was fabricated by microelectromechanical systems (MEMS) process. It mainly includes film deposition (PA-C, Al, Mg), photoresist-spray-coating-based liftoff process, reactive ion etching (RIE), and wet-chemical anisotropic etching. The fabrication process steps are shown in Figure 3-15A and detailed as follows.

1) A 4-inch silicon wafer was prepared for fabrication through piranha plus buffered hydrofluoric acid (BHF) cleaning, and then 3-minutes hexamethyldisilazane (HMDS) treatment, respectively. The HMDS treatment facilitated peeling off of PA-C from silicon wafer at the last step. 10-µm-thick PA-C film was then deposited over the wafer. After that, 0.1-µm-thick aluminum (Al) layer was thermally evaporated over the PA-C and the photoresist (PR) AZ1518 was spin-coated, exposed, and developed to pattern Al as a oxygen plasma-etching mask for PA-C.

2) Oxygen plasma (400W, 300mT) in RIE was used to etch through the openings on PA-C film all the way down to silicon surface. Then Al layer was etched away in Al etchant from Transene Company, Inc. at 60 ◦C, followed by Deionized water (DI water) rinsing.

3) Next, 1-µm-thick Mg was evaporated on the 4-inch wafer over the PA-C using E-beam following the recipe reported in Table 3-1.

4) 10-µm-thick photoresist (PR) AZ4620 was then spin-coated and patterned through lithography as a sacrificial layer. Another run of oxygen plasma (50W, 200mT, 1 minute) in RIE was applied to roughen the surface of PA-C, followed by a 30-second BHF cleaning to make the surface hydrophobic.

5) The final 5-µm-thick PA-C layer was deposited over the device.

6) 0.1-µm-thick aluminum (Al) layer was thermally evaporated over the top PA-C and the photoresist (PR) AZ1518 was spin-coated, exposed, and developed to pattern Al as a oxygen plasma etching mask for PA-C.

7) Top PA-C layer is then etched through by oxygen plasma (400W, 300mT). Al layer was then etched away in Al etchant from Transene Company, Inc. at 60 ∘C, followed by Deionized water (DI water) rinsing.

8) Finally, the sacrificial photoresist was taken away by acetone, and the magnesium-embedded cell filters were peeled off from silicon in DI water. The SEM photo of the final Mg-embedded filters is shown in Figure 3-5B.
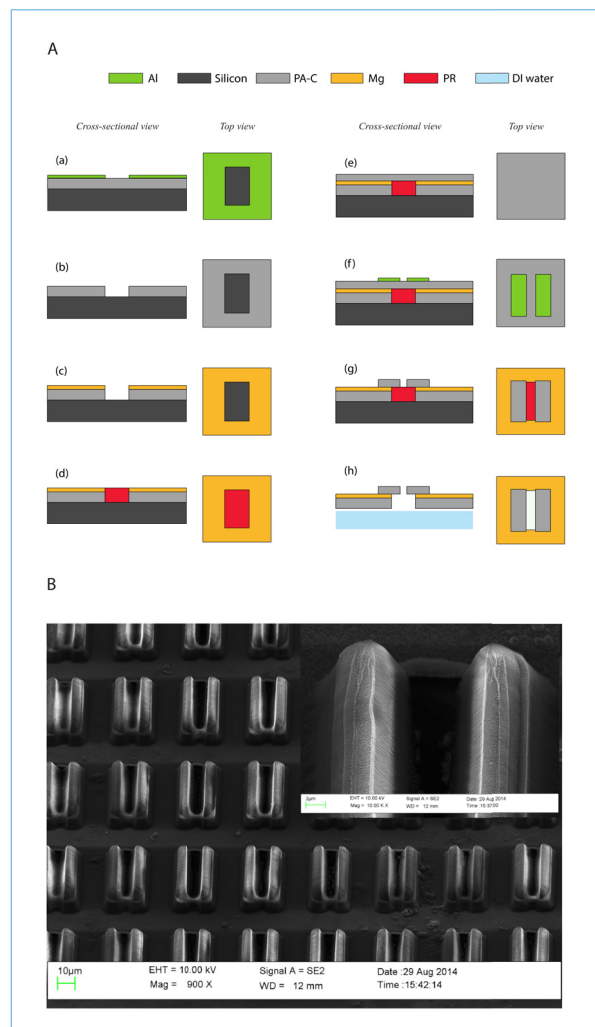
Figure 3-15. A, Fabrication process of the filter: a) Al deposition/patterning on Si as PA-C etching mask, b) Oxygen plasma etching of PA-C, c) Mg deposition, d) Photoresist spin-coating/patterning, e) PA-C deposition, f) Al deposition/patterning, g) PA-C etching, h) Photoresist dissolving and peeling off device from Si substrate. B, SEM photo of Magnesium-embedded CTC filter.

3.5.4   Setup Design and Assembly

Figure 3-16A shows the schematic of the CTC medium filtration system. Pressure from a nitrogen tank was reduced to <1 psi by a two-stage regulator and further down-regulated accurately by adjusting a needle valve to around 0.13 psi. The filter was sandwiched between two pieces of PDMS with wells. Two wells formed a chamber where they were tightened. The PDMS films were coated onto two acrylic pieces for mechanical support. The Mg-embedded filter after medium filtration is shown in Figure 6B, while Figure 6C is fluorescence photo of captured CTCs.
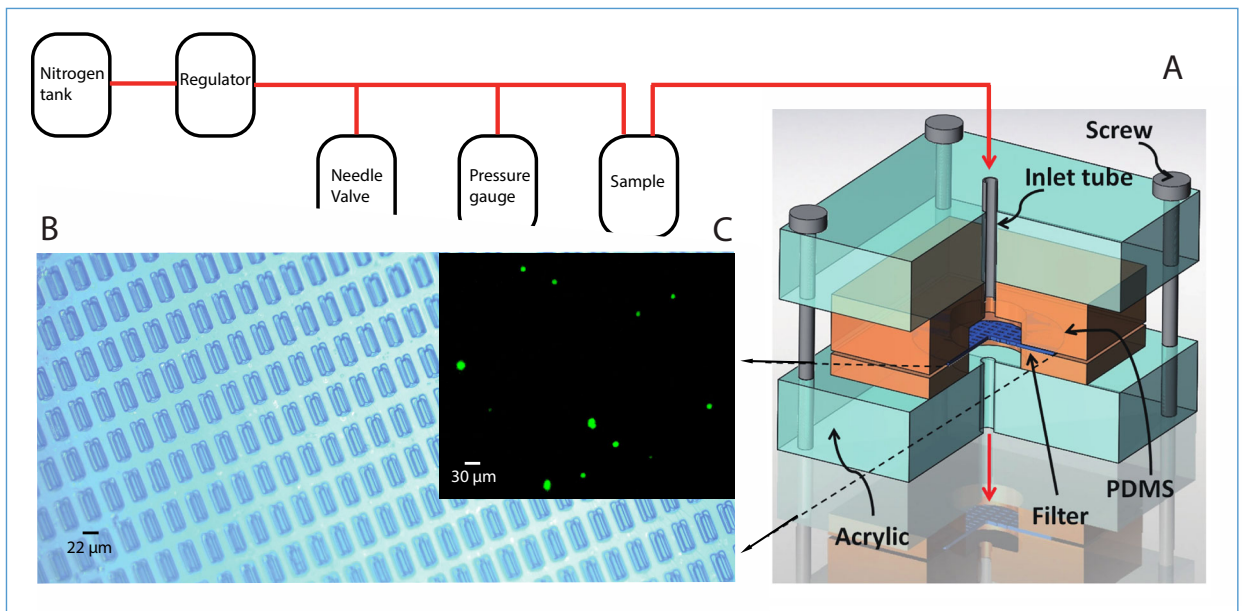
Figure 3-16. A, Constant-pressure fluid delivery system for the process of filtration that consists of the nitrogen tank as pressure source, as well as regulator, needle valve, and pressure gauge to control and read the pressure. B, Micrograph of Mg-embedded filter under bright field. C, Fluorescence photo of captured CTCs after filtration process.

3.5.5   Experiments

Green fluorescent protein labeled MDA-MB-231 breast cancer cells (~16 μm in diameter) were used to test the new design of the Mg-embedded CTC filter. 29 MDA-MB-231 cells were spiked into 0.4 mL PBS with the filtration done in 5 minutes. 26 cells were successfully recovered. Capture efficiency was 89.7%. This efficiency is comparable to what T. Xu claimed in [28], which is around 90%.

As shown in Figure 3-17A, the Mg coats remained un-etched 1 minute after filtration, keeping the filter intact. When the filter was incubated with DMEM for 150 min, the top PA-C slots were detached, due to the underneath Mg sacrificial layer total dissolving (Figure 3-17B). As a result, the captured cancer cells were released from the filter. To pick up the isolated cells, we have set up the system that consists a micromanipulator, a micropipette with 20-μm inner diameter (ID), a syringe, and a syringe pump. The micropipette was controlled by the micromanipulator, and it was connected to the syringe pump, which was to create the suction force for aspirating released cells (Figure 3-17C).
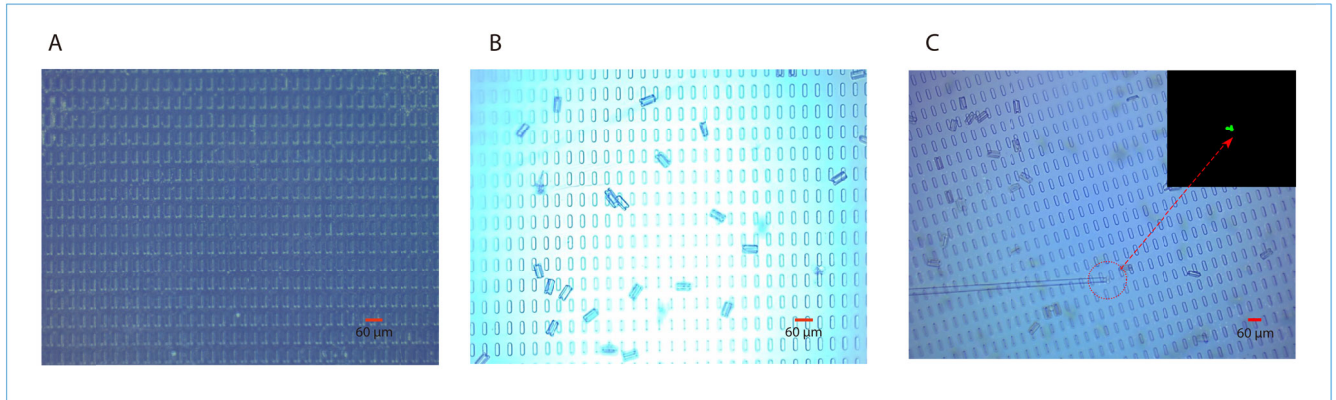
Figure 3-17. Mg dissolving process in DMEM and CTCs release: A, After 1 min. Mg remained in place during filtration process. Top parylene secured to bottom parylene. B, After 150 min. Mg is totally etched away. Top parylene free-released from the bottom parylene. C, MDA-MB-231 breast cancer cells released. Cells were aspirated into the micropipette.
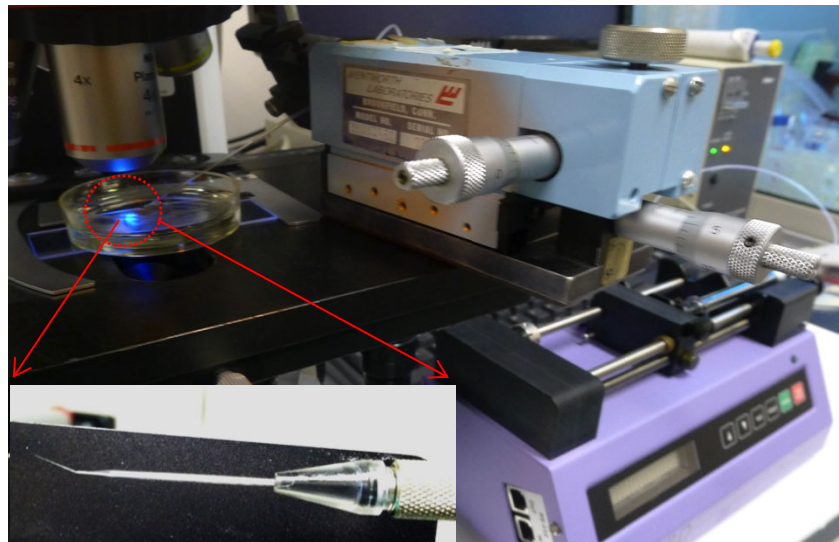
Figure 3-18. A, Setup for CTC aspiration into micro-pipette. B, close-up of the micro-pipette with 20 μm tip.

3.6 Results and Discussion

Two-dimensional finite element method (FEM) analysis was performed on the Mg etching process in DMEM for the structure design. The results were then applied to the fabrication of a novel Magnesium-embedded cell filter, which could potentially be used for capture of rare CTCs followed by recovery of CTCs with high purity (no WBC background) that is essential for RNA expression profiling to guide cancer management. This new design with a thin-film Mg sacrificial layer allows us to release captured CTCs without adding any additional chemicals. The feasibility of this novel Mg-embedded CTC filter has been successfully demonstrated.

Although this novel Mg-embedded filter is a promising method to capture and release CTC with high purity without any additional chemical, blood tests from cancer patients need to be performed and statistical biology data need to be collected to further compare this new approach with others.

3.7 Reference

[16]   S. C. Williams, Circulating tumor cells, *PNAS*, vol. 13, pp. 4861, 2013

[17]   S. J. Cohen *et al,* Relationship of circulating tumor cells to tumor response, progression-free survival, and overall survival in patients with metastatic colorectal cancer *J. Clin. Oncol*, vol. 26, pp. 3213–21, 2008

[18]   M. Ignatiadis *et al*, Different prognostic value of cytokeratin-19 mRNA positive circulating tumor cells according to estrogen receptor and HER2 status in early-stage breast cancer, *J. Clin. Oncol*, vol. 25, pp. 5194–202, 2007

[19]   K. Fizazi *et al,* High detection rate of circulating tumor cells in blood of patients with prostate cancer using telomerase activity, *Ann. Oncol*, vol.183, pp. 518–21, 2007

[20] B. Hu and A. Goldkorn, Circulating tumor cells in prostate cancer: a better predictor of survival than prostate specific antigen? *Expert Rev. Anticancer Ther.,* vol. 14, pp. 1257–60, 2014

[21] P. Li *et al,* Acoustic separation of circulating tumor cells, *PNAS*, vol.16, pp. 4970–5, 2015

[22] S. Nagrath, L. V. Sequist, S. Maheswara, D. W. Bell, D. Irimia, L. Ulkus and M. Toner, Isolation of rare circulating tumour cells in cancer patients by microchip technology, *Nature*, vol. 7173, pp. 1235–9, 2007

[23] B. L. Khoo, M. E. Warkiani, D. S. W. Tan, A. A. S. Bhagat, D. Irwin, D. P. Lau and C. T. Lim, Clinical validation of an ultra high-throughput spiral microfluidics for the detection and enrichment of viable circulating tumor cells, *Plos One*, vol. 10, e111296, 2014

[24] B. J. M. Gasent *et al,* Circulating tumor cells in breast cancer: methodology and clinical repercussions, *Clin. Transl. Oncol*, vol. 10, pp. 399–406, 2008

[25] M. Münz *et al,* Side-by-side analysis of five clinically tested anti-EpCAM monoclonal antibodies, *Cancer Cell Int.,* vol. 10, pp. 44, 2010

[26] N. M. Karabacak, P. S. Spuhler, F. Fachin, E. J. Lim, V. Pai, E. Ozkumur and M. Toner, Microfluidic, marker-free isolation of circulating tumor cells from blood samples *Nat. Protocols*, vol. 3, pp. 694–710, 2014

[27] H. W. Hou, M. E. Warkiani, B. L. Khoo, Z. R. Li, R. A. Soo, D. S. W. Tan, and C. T. Lim, Isolation and retrieval of circulating tumor cells using centrifugal forces *Sci. Rep.*, vol. 3, pp. 1259, 2013

[28] T. Xu, B. Lu, Y. C. Tai, and A. Goldkorn, A cancer detection platform which measures telomerase activity from live circulating tumor cells captured on a microfilter, *Cancer Res.,* vol. 70, pp. 6420–6, 2010

[29] G. Vona *et al,* Isolation by size of epithelial tumor cells: a new method for the immunomorphological and molecular characterization of circulating tumor cells, *Am. J. Pathol.*, vol. 1, pp. 57–63, 2000

[30] A. Goldkorn *et al,* Circulating tumor cell telomerase activity as a prognostic marker for overall survival in SWOG 0421: A phase III metastatic castration resistant prostate cancer trial, *Int. J. Cancer*, vol. 136, pp. 1856–62, 2015

[31] Y. Liu, J. Park, J. H. Chang, and Y. C. Tai, Thin-film magnesium as a sacrificial and biodegradable material, *Proc. 2014 IEEE 27th. Int. Conf. on Micro Electro Mechanical Systems (MEMS) (San Francisco, USA, 26–30 January 2014)* pp. 656–9, 2014

[32]   M. P. Staiger, A. M. Pietak, J. Huadmai, et al. Magnesium and its alloys as orthopedic biomaterials: a review. *Biomaterials*, vol. 27, pp. 1728–1734, 2006

[33]   X. Gu and Y. Zheng, A review on magnesium alloys as biodegradable material, *Front. Mater. Sci. China*, vol. 4, pp. 111-115, 2010

[34]   J. Liu, Y. C. Tai, J. Lee, K. C. Pong. Y. Zohar, and C. M. Ho, In situ monitoring and universal modelling of sacrificial PSG etching using hydrofluoric acid, in *Digest Tech. Papers MEMS'93 Conference*, Fort Lauderdale, February 7-10, pp. 71-76, 1993

4 PARYLENE BASED MICROELECTRODE FILTER FOR SINGLE-ISLET ELECTROISLETOGRAM

4.1 Introduction

This chapter introduces the parylene based microelectrode filter for single-islet electroisletogram. Background and motivation will be discussed first, followed by design, fabrication, and testing. Periodic electroisletogram has been achieved from islets, which has demonstrated the feasibility of this design and potential application for islet screening process. Details will be presented in the following sections.

4.2 Diabetes

Diabetes, which is also known as diabetes mellitus (DM), is a group of metabolic diseases in which there are high blood sugar levels over a prolonged period. Symptoms of high blood sugar include frequent urination, increased thirst, and increased hunger. If left untreated, diabetes can cause many complications. Acute complications include diabetic ketoacidosis and nonketotic hyperosmolar coma. Serious long-term complications

include cardiovascular disease, stroke, chronic kidney failure, foot ulcers, and damage to the eyes. [35]

Diabetes is due to either the pancreas not producing enough insulin or the cells of the body not responding properly to the insulin produced. [36] There are three main types of diabetes mellitus:

Type 1 DM results from the pancreas's failure to produce enough insulin. This form was previously referred to as "insulin-dependent diabetes mellitus" (IDDM) or "juvenile diabetes". The cause is unknown. [37]

Type 2 DM begins with insulin resistance, a condition in which cells fail to respond to insulin properly. [37] As the disease progresses a lack of insulin may also develop. [38] This form was previously referred to as "non insulin-dependent diabetes mellitus" (NIDDM) or "adult-onset diabetes". The primary cause is excessive body weight and not enough exercise. [37]

Gestational diabetes, is the third main form and occurs when pregnant women without a previous history of diabetes develop high blood-sugar levels. [37]

4.2.1 State-of-art Research on Islets Transplantation

Worldwide, more than 750 individuals with type 1 diabetes mellitus (T1DM) have received allogeneic islet transplants since 1974, in an effort to cure their chronic condition. [38] Though this is still a small number (especially when compared with the estimated 1 million afflicted with T1DM and an additional 17 million with type 2 diabetes in the US, not to mention the estimated 140 million with diabetes worldwide), much has been learned. The initial enthusiasm over the observation that islet

transplantation can restore insulin-independent euglycemia to patients with long-standing T1DM has been dampened by complications associated with the procedure itself and the immunosuppression necessary to prevent rejection of the transplanted islets, as well as by the gradual loss of islet function and other problems arising from the placement of allogeneic islets in the liver [39, 40].

Nevertheless, the field of islet transplantation has evolved significantly from the breakthrough of the Edmonton Protocol in 2000, since significant advances in islet isolation and engraftment, together with improved immunosuppressive strategies, have been reported. The main limitations, however, remain the insufficient supply of human tissue and the need for lifelong immunosuppression therapy. [41] Great effort is then invested in finding innovative sources of insulin-producing β cells. At the same time, researchers have been studying the screening of islets to improve the efficiency of implantation.

4.2.2 Motivation of Detecting Single-islet Electroisletogram

As discussed in section 4.2.1, other than direct insulin injection, one promising treatment for Type I diabetes is islet transplantation [42]. In islet transplantation, pancreatic islets from a donor are injected into the liver of another person and recent results showed that 58% of the transplanted patients were insulin independent for more than one year. However, one of the key lacking technologies of islet transplantation is high-throughput islet screening since each transplantation requires about one million islets. Islets, which are heterogeneous by nature, are currently screened as whole populations containing a range of functioning and dysfunctional characteristics [43].

Currently, processed islets are only screened in bundles of 1,000+ islets, so many "bad" islets are not removed. This work represents the first attempt to develop a MEMS technology for the screening of every single islet so as to guarantee no bad islet at all, which should improve results of islet transplant therapy [44]. The ultimate goal motivating this work is to improve the yield and quality of functioning human islets from donor cadaver pancreases for islet transplant therapy for diabetes patients.

The first MEMS feasibility study of targeting islet membrane potential for fast screening and the results are very promising. It is interesting because the release of insulin by beta cells is triggered by glucose through the depolarization of the beta cell membrane. Theoretically, all the beta cells would synchronize their depolarization and provide a constructive depolarization potential. Therefore, monitoring EIG could potentially be very useful for screening healthy islets.

4.3   Design

Here we report the first MEMS device designed for in vitro measuring of electroisletogram (EIG) of individual rat islets.   Using vacuum to hold an islet in proximity to a microelectrode, strong EIG signals in millivolt range are obtained, while the noise is about 100μV pk-pk.

4.3.1   Concept of System Level Design

The platform for single-islet EIG consists of 3 modules: 1, a dam that holds culture medium; 2, the microelectrodes that connect to the Printed Circuit board (PCB); and 3, tubes that connect holes on the PCB to a vacuum pump, which creates suction at one microelectrode. Figure 4-1 is an illustration of the islet screening apparatus, where

one electrode has suction to achieve proximity with an islet, and another electrode acts as ground. Through-holes are drilled in a PCB and the device is peeled from the wafer, taped to the PCB, and shorted to the PCB with silver paint.
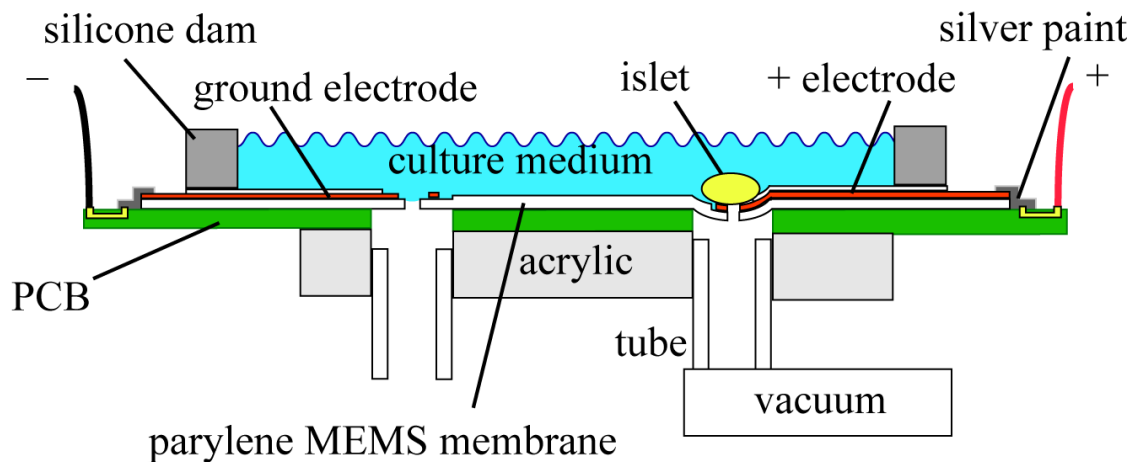
Figure 4-1. Schematic diagram of the islet screening apparatus. The right electrode deflects due to suction from a vacuum pump. Surface tension prevents culture medium from leaking into the left tube.

4.3.2   Parylene Based Microelectrodes Filter Design

Parylene-C is a good candidate as the material for substrate of multielectrode arrays (MEAs), due to its high biocompatibility, good mechanical strength and machinability. It has been widely used in bio-MEMS applications, including recent work on intraocular implant and cell filtration [38]. Parylene has been widely studied [45-47] and used in various industries because of its many excellent properties, such as superior barrier property used to protect the electronic devices against damages from moisture and corrosive etchants [48-50].

4.3.2.1   First Generation of Design (round electrodes)

The design and micro-fabrication process of MEAs on parylene-C film is detailed

in Figure 4-2. First, a 4-inch wafer was prepared for fabrication after piranha plus

buffered hydrofluoric acid (BHF) cleaning, followed by the hexamethyldisilazane

(HMDS) treatment. Enough time was given for enough amount of HMDS to form

multilayers on parylene-C film, which enabled easy-peeling of the whole device at the

end of fabrication. A 10-µm-thick PA-C film was then deposited over the wafer (Figure

4-2a). When Chemical vapor deposition (CVD) process of PA-C finished, the coated

silicon wafer was moved to oxygen plasma chamber and went through the "descum"

process. 50W, 200mT, and 2 minutes recipe was used to roughen the PA-C surface, as

well as create oxygen related functional groups for better Ti/PA-C adhesion. Next,

Electron beam physical vapor deposition (EBPVD) is performed on Titanium/Gold

(Ti/Au). A 200Å-thick Ti layer and 3000Å-thick Au layer were then deposited on PA-C.

2µm-thick photoresist (PR) AZ1518 was then spin-coated and patterned as the etching

mask for Ti/Au. Wet-etching was performed and Ti/Au is patterned (Figure 4-2b). After

that, another 5µm-thick PA-C layer was deposited on top (Figure 4-2c). In order to

expose the surface of microelectrodes and connecting pads, 10µm-thick PR AZ4620 was

patterned as etching mask for top PA-C layer. Oxygen plasma (400W, 300mT) is used to

etch through the openings (Figure 4-2d). The top PA-C film is to reduce parasitic

capacitance between the positive electrode and the culture medium. Then, 20µm-thick PR

AZ4620 layer was spin-coated and patterned differently to create suction holes. The

bottom PA-C film is etched by oxygen plasma all the way down to the silicon surface

(Figure 4-2e). Finally, the device is peeled from the wafer and connected to the PCB with silver paint (Figure 4-2f).

Figure 4-3 shows the close-up of MEMS electrodes. Au surface is exposed and the center suction holes are created.
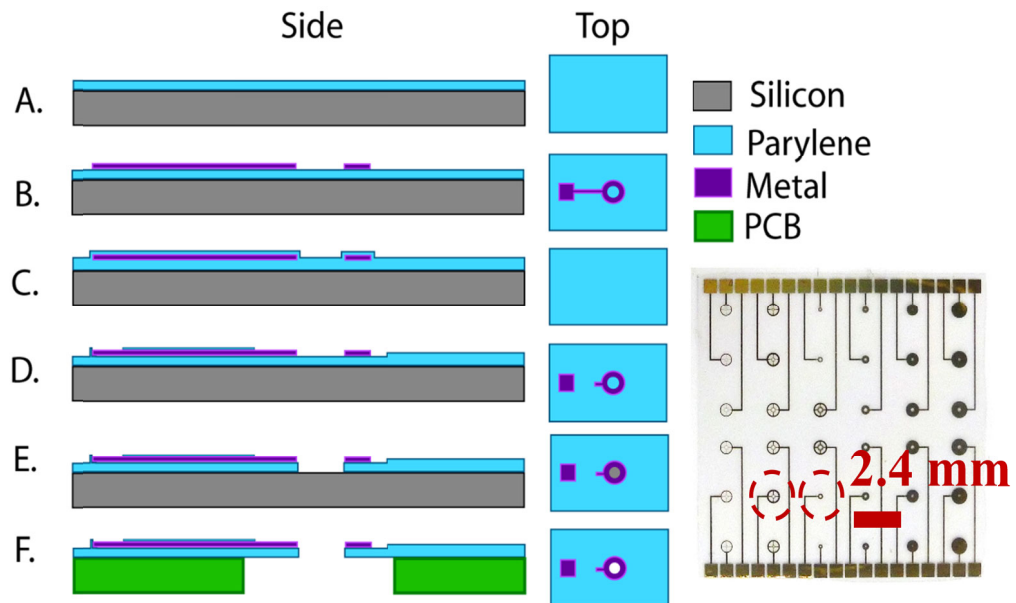
Figure 4-2. Left: Fabrication process of EIG microelectrodes. A: PA-C deposition/patterning on Si, B: Ti/Au deposition and patterning, C: Top PA-C deposition, D: Expose islet contact area and electrical connection pad, E: Etching suction holes in PA-C, F: Peel off of Si and tape to PCB. Right: Parylene MEMS membrane after peeling.
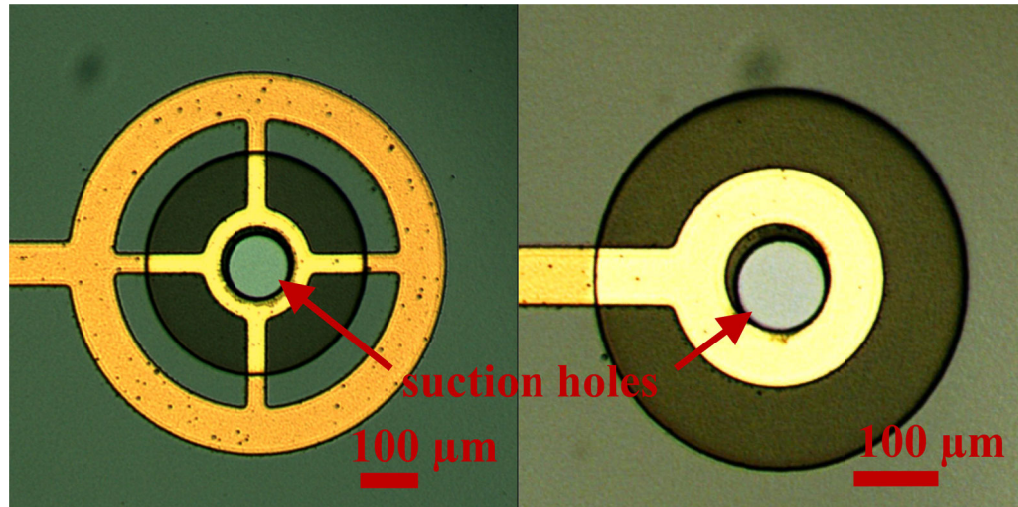
Figure 4-3. MEMS electrodes with vacuum-suction holes. The above electrodes are circled in final MEMS device in Figure 4-2.

4.3.2.2   Second Generation of Design (fishnet electrodes)

To determine what pattern of electrode could capture, hold and release islets the best, grids of holes of varying street width and hole diameters were investigated, reminiscent of a fishnet. Holes that were too big could not capture islets. Meanwhile holes too small could not have enough suction, and streets too wide could not release islets (Figure 4-4). Hole diameters of 20μm, 40μm, 60μm, and 80μm and street widths of 20μm, and 40μm were investigated.
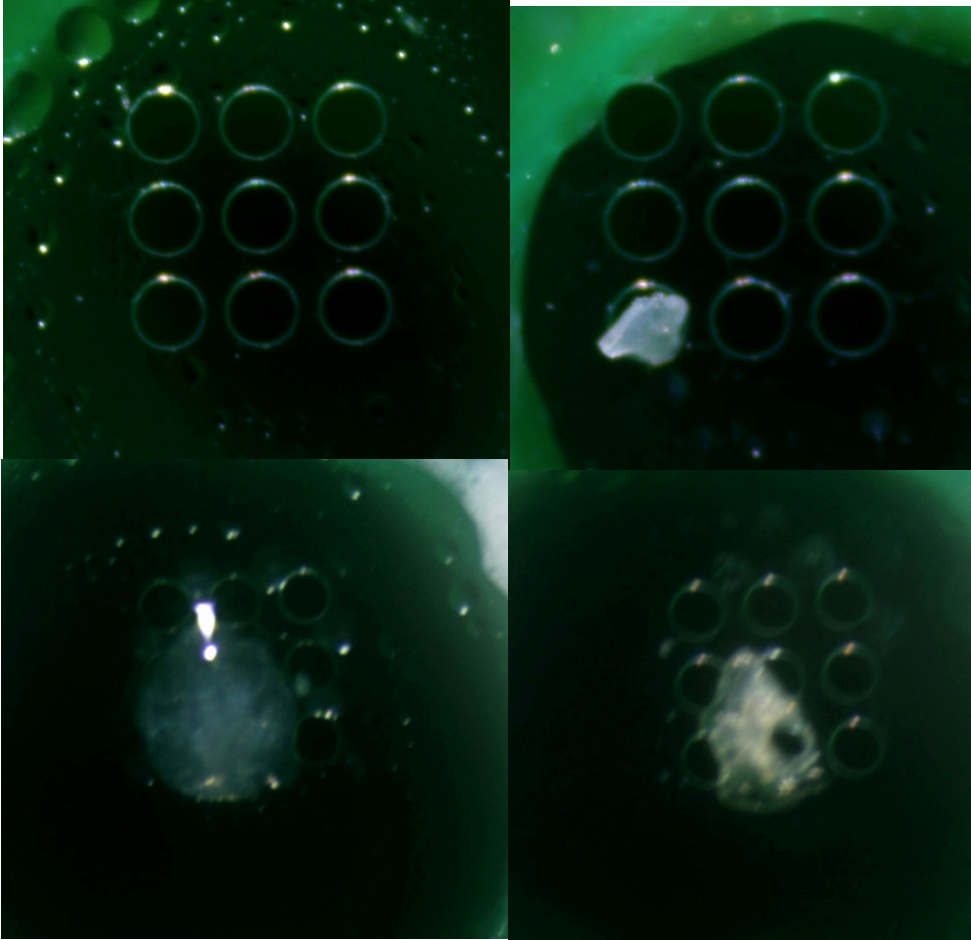
Figure 4-4. Fishnet test design. Top left: 60μm diameter, 20μm street. Top right: Same as top left showing islet is too small. Bottom left and right: 60μm diameter, 40μm street, before and after back pressure. Islet could not be removed in this case.

Table 4-1: Summary of different hole and street sizes on capturing islets.

Street width / Hole diameter	20 μm	40 μm
20 μm	Islets captured. Can be released with back pressure	(presumed streets too wide)
40 μm	Islets captured. Can be released with	Streets too wide. Islet sticks even with backpressure

	back pressure	
60 μm	Holes too big. Islets not captured	Streets too wide. Islet sticks even with backpressure
80 μm	(presumed hole too big)	Holes too big. Small and medium islets not captured. Streets too wide. Islet sticks even with back pressure

A satisfactory design was considered to be able to hold islets, and release it with back-pressure (suction of 2.61 psi). Back-pressure was provided by an aero-duster of internal pressure no greater than 300 psi. Table 4-1 is the summary of different hole and street sizes on capturing islets. The two most satisfactory designs had street width of 20μm, and hole diameters of either 20μm or 40μm.
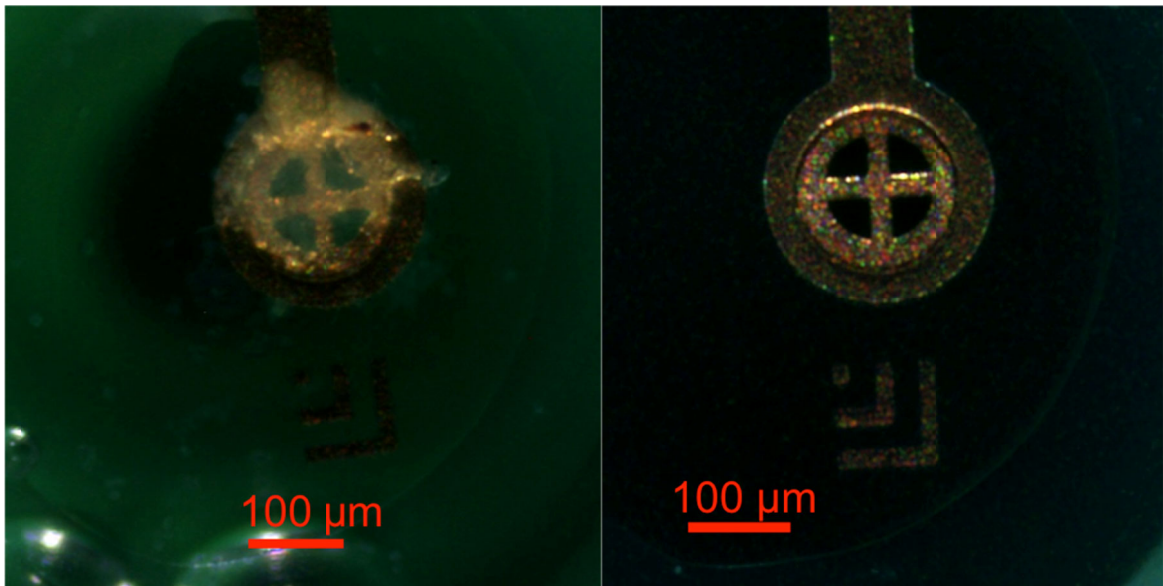
Figure 4-5. Fishnet MEMS electrodes with vacuum-suction holes. The same electrode is pictured with a captured islet, and after the islet is removed.

4.4 Assembly and Integration

Figure 4-6 is the picture of the entire setup. Both the MEMS EIG device and the recording system to computer are placed inside a shielding box to reduce the noise level. Each MEMS suction pad has a labeled lead and suction tube so an arbitrary pad may be selected.

Figure 4-6. Picture of entire setup. Each MEMS suction pad has a labeled lead and suction tube so an arbitrary pad may be selected.

Figure 4-7 shows the close up of MEMS EIG device on the PCB. Each microelectrode is shorted to one PCB pad, which connects to the recording system by wire. A 8mm by 10mm silicone dam is made as the reservoir for islets culture medium, and glued on the top of PA-C microelectrodes device.

Figure 4-7. Picture of close up of MEMS EIG device.

4.5   Results and Discussion

Islets were isolated from a rat pancreas, and then settled in 3mM glucose medium for around 2 hours before the measurement of EIG. Figure 4-8 is the fluorescence photo of Cal-520™, AM (calcium-sensitive) dyed islets. Glucose level was brought up to 11.1 mM before measurement to enable more rapid islet firing. Islets, together with medium, were dropped on the MEMS apparatus, and then the vacuum pump was turned on to suck one single islet to the desired fishnet electrode. Recording was started to get single islet EIG.
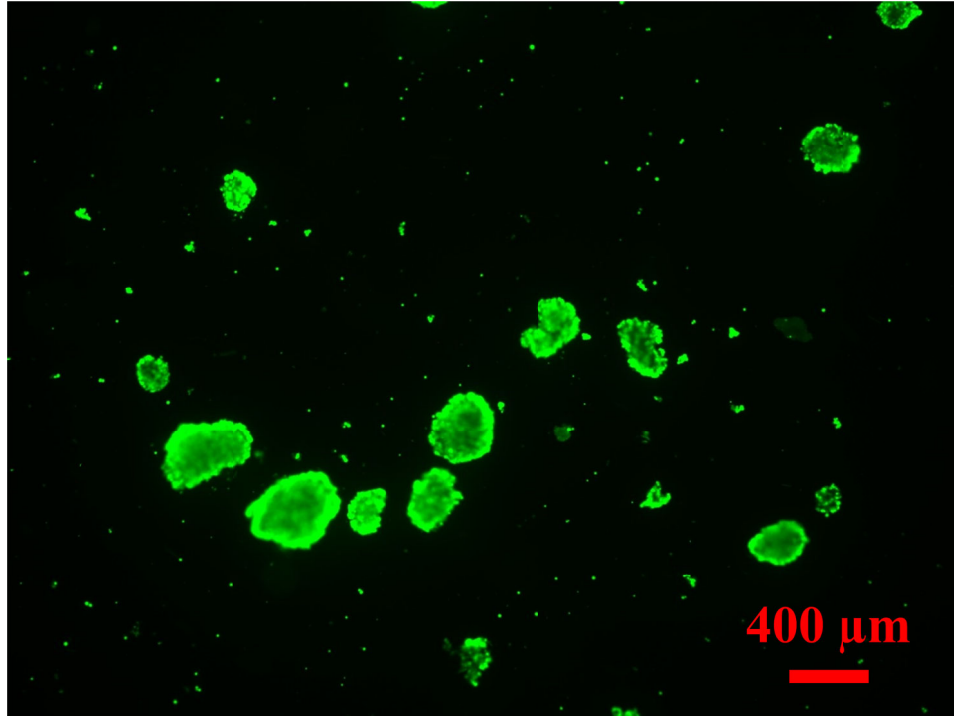
Figure 4-8. Fluorescence photo of Cal-520™, AM (calcium-sensitive) dyed islets.

Figure 4-9 shows a 20-minute-long recording of EIG of a rat islet in 11.1 mM glucose culture medium, showing multiple packets of action potentials. The first packet is plotted in Figure 4-10. The results show that clear and large signal-to-noise EIG can be obtained using a MEMS EIG device (SNR = 106).
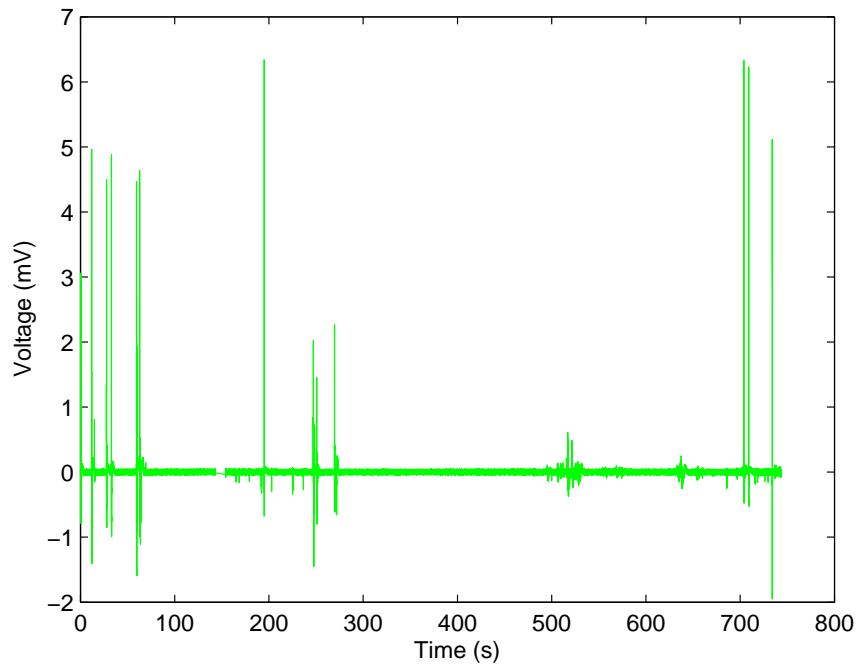
Figure 4-9. Extended recording of EIG of islet in 11.1 mM glucose culture medium.

Packets of action potentials separated by several minutes are as expected from healthy

islets at this concentration of glucose.
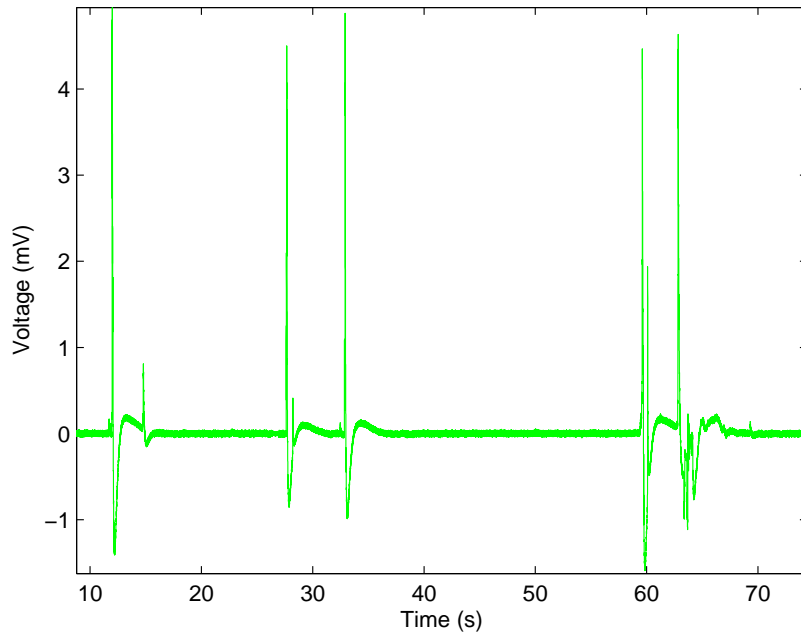
Figure 4-10. Close up of action potentials from Figure 4-9 shows an achieved SNR=106. The EIG signal shape is expected and EIG magnitude is satisfactory compared to patch clamp due to sufficient coupling capacitance between the electrode and islet membrane and minimal parasitic capacitance between the electrode and culture medium.

4.6   Summary

This work has successfully demonstrated the MEMS device designed for in vitro measuring of EIG of individual rat islets. Strong EIG signals in millivolt range are obtained. With this success, the next work will be to build MEMS EIG arrays including microfluidics for the screening of a large number of islets.

4.7   Reference

[35]   *Diabetes mellitus - Wikipedia, the free encyclopedia*. Available: https://en.wikipedia.org/wiki/Diabetes_mellitus

[36]   Shoback, edited by G. G. David, Chapter 17, Greenspan's basic & clinical endocrinology (9th ed.). New York: McGraw-Hill Medical. ISBN 0-07-162243-8, 2011

[37]   "Diabetes Fact sheet N°312". WHO. October 2013. Retrieved 25 March 2014

[38]   K. I. Rother and D. M. Harlan, Challenges facing islet transplantation for the treatment of type 1 diabetes mellitus, *J Clin Invest.*, vol. 114, pp. 877–883, 2004

[39]   B. Hirshberg, K. I. Rother, B. J. Digon, J. Venstrom, and D. M. Harlan, State of the art: islet transplantation for the cure of type 1 diabetes mellitus, *Rev. Endocr. Metab. Disord.*, vol. 4, pp. 381–389, 2003

[40]   A. M. Shapiro et al, Islet transplantation in seven patients with type 1 diabetes mellitus using a glucocorticoid-free immunosuppressive regimen, *N. Engl. J. Med.,* vol. 343, pp. 230–238, 2000

[41]   S. Pellegrini, E. Cantarell, V. Sordi, R. Nano, L. Piemonti, The state of the art of islet transplantation and cell therapy in type 1 diabetes, *Acta Diabetol.,* pp. 1-9, 2016

[42]   N.C. Close, B.J. Hering, and T.L. Eggerman, Results From the Inaugural Year of the Collaborative Islet Transplant Registry, *Transplantation Proceedings*, vol. 37, pp. 2, 2005

[43]   I. R. Sweet, M. Gilbert, S. Scott, I. Todorov, R. Jensen, I.Nair, I. Al-Abdullah, J. Rawson, F. Kandeel, and K.Ferreri, Glucose-Stimulated Increment in Oxygen Consumption Rate as a Standardized Test of Human Islet Quality, *American Journal of Transplantation*, vol. 8, pp. 1, 2008

[44]   I. Todorov, I. Nair, A. Avakian-Mansoorian, J. Rawson, K. Omori, T. Ito, L. Valiente, I. Iglesias-Meza, C. Orr, K.D. Shiang, K. Ferreri, I.H. Al-Abdullah, Y. Mullen, and F. Kandeel, Quantitative assessment of β-cell apoptosis and cell composition of isolated, undisrupted human islets by laser scanning cytometry, *Transplantation*, vol. 90, pp. 8, 2010

[45]   D. Kang, S. Matsuki, and Y.-C. Tai, Study of the hybrid parylene/PDMS material, *in Micro Electro Mechanical Systems (MEMS), 2015 28th IEEE International Conference on*, pp. 397-400, 2015

[46]   D. Kang, A. Stanley, J. H. Chang, Y. Liu, and Y. C. Tai, Effects of deposition temperature on Parylene-C properties, *in Micro Electro Mechanical Systems (MEMS), 2013 IEEE 26th International Conference on*, pp. 389-390, 2013

[47]   D. Kang, J. H. Chang, J. Y. H. Kim, and Y. C. Tai, In situ heating to improve adhesion for parylene-on-parylene deposition, *in 7th IEEE International Conference on Nano/Micro Engineered and Molecular Systems (NEMS)*, pp. 226-229, 2012

[48]   J. H. Chang, Y. Liu, D. Kang, M. Monge, Y. Zhao, C. C. Yu, et al., Packaging study for a 512-channel intraocular epiretinal implant, *in Micro Electro Mechanical Systems (MEMS), 2013 IEEE 26th International Conference on*, pp. 1045-1048, 2013

[49]   J. H. Chang, D. Kang, and Y. C. Tai, High yield packaging for high-density multi-channel chip integration on flexible parylene substrate, *in Micro Electro Mechanical Systems (MEMS), 2012 IEEE 25th International Conference on*, pp. 353-356, 2012

[50]   J. H. C. Chang, Y. Liu, D. Kang, and Y. C. Tai, Reliable packaging for parylene-based flexible retinal implant, *in Solid-State Sensors, Actuators and Microsystems (TRANSDUCERS & EUROSENSORS XXVII), 2013 Transducers & Eurosensors XXVII: The 17th International Conference on*, pp. 2612-2615, 2013

5 PARYLENE-ON-PDMS MEMBRANE FOR VACCINE PRODUCTION

5.1 Introduction

First of all, an overview on state-of-art vaccine production will be given and places to improve will be discussed, together with motivation (section 5.2). In section 5.3, a novel parylene-on-PDMS membrane design for vaccine production will be proposed. Section 5.4 will focus on the fabrication process. Oxygen permeation and modeling will be discussed in section 5.5. A series of experiments have been done to demonstrate its feasibility (section 5.6).

Approximately, every second man and every third woman is affected by cancer at some point in their life. Conventional cancer therapies, like surgery, chemo-, and radiotherapy, are not always effective enough alone to defeat cancer, and often they have severe side effects. New therapy options are desperately needed for treating cancer, and hence the design of efficient cancer treatments is one of the major challenges of medical science. A combination of traditional and novel cancer treatments may improve the

patient's prognosis, or even cure the patient if the cancer is detected early enough. Gene therapy and oncolytic viruses hold great promise for the development of novel cancer therapies. Oncolytic vaccinia virus (VV) has emerged as a promising candidate for gene therapy agent. [51] Amgen's Imlygic (talimogene laherparepvec), the first FDA-approved oncolytic virus therapy, will be available within weeks at $65,000/patient.

Vaccinia Viral (VV) Forms are briefly introduced here. There are 4 kinds of forms in total:

1. Intracellular Mature Virion (IMV) – is the most abundant form of virus and is retained in cells until lysis; it is a robust, stable virion and is well suited to transmit infection between hosts. [52]

2. Intracellular Enveloped Virion (IEV) – is formed by wrapping of IMV with intracellular membranes, and is an intermediate between IMV and CEV/EEV that enables efficient virus dissemination to the cell surface on microtubules. [52]

3. Cell-associated Enveloped Virion (CEV) – induces the formation of actin tails that drive CEV particles away from the cell and is important for cell-to-cell spread. [52]

4. Extracellular Enveloped Virion (EEV) - mediates the long-range dissemination of virus in cell culture and, probably, in vivo. [52]

The morphogenesis of VV is shown in Figure 5-1. IMV are made in a virus factory and move on microtubules (MT) to the wrapping membranes derived from the tran-Golgi network (TGN) or early endosomes. A double membrane to form IEV that move to the cell surface on MT wraps IMV. The IEV membrane fuses with the plasma membrane to form CEV that induce actin tail formation to drive the virion away from the cell. CEV also be possibly released to form EEV. [52]
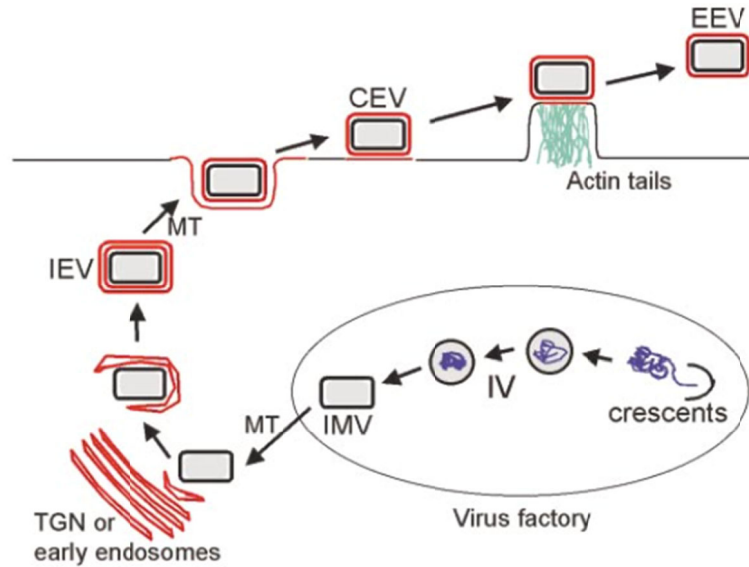
Figure 5-1. VV morphogenesis

From the discussion above we can see there are a lot of places to improve innovatively. For instances, Culture of cells for large-Scale vaccine (VV) production, Purification of viruses and infectivity of viruses. A bunch of detailed questions worth research, like viral loss due to aggregation during filtering. But here, in this chapter, the culture of cells is studied as the most fundamental way to improve the efficiency of large-scale vaccine production.

5.2   Motivation

The PFU target for oncolytic therapy is 10^{10} PFU/dose. Given 100 patients, then 10^{12} PFU Total is needed. Currently the two most popular tools for the cell culture are flasks and bioreactors. Simple calculation can be done to estimate the time and volume cost for the target. For the bioreactor, the cell density can reach 2.4×10^5 cells/ml. There

could be 5000 viruses/cell. And in our case, the PFU/virus is 1/100, which indicates the effective virus number is 1 out of 100 virus. So the PFU density is calculated as $(2.4 \times 105$ cells/mL)*(5000 viruses/cell)*(1/100 PFU/virus) = 12×106 PFU/ml. Therefore, a 100L bioreactor is needed. [53] For the flasks (for instance T-225 flask), Cells density can be calculated as 2×10^7 cells/225cm^2, which equals to 90×10^3 cells/cm^2. So the PFU per area can be calculated as $(90 \times 10^3$cells/cm^2)*(5000 viruses/cell)*(1/100 PFU/virus) = 4.5×10^6 PFU/cm^2. Therefore, 222×103 cm^2 surface area is needed, which equals to 1000 T225 flasks. Also each flask occupies 800mL space, so it requires 1m^3 of incubator space. Besides space cost, feeding one flask takes around 30 seconds, if feeding 3 times a week, it takes 25 hours per week to do the job. In order to be more efficient, both space and time cost should be lowered.

Besides time and space cost, another disadvantage of bioreactor is that gas sparging's damage to cells. In sparged bioreactors, cells are attached to micro carriers and oxygen as well as carbon dioxide is supplied through gas bubbles. The higher energy-dissipation rate combined with the microeddy length being smaller than the sizescale of the cell make bubbles smaller 1mm diameter more deadly. [54] Figure 5-2 shows the specific death rate vs. bubble diameter.
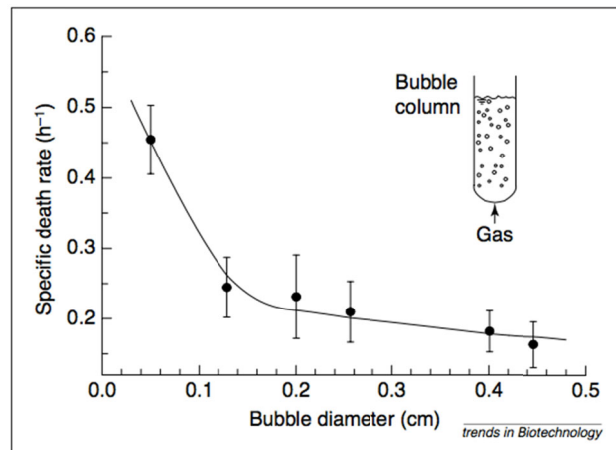
Figure 5-2. Specific death rate vs. bubble diameter [54]

The effect of shear is also one limiting factor that needs to be taking into account. Figure 5-3 shows that the shear rate has a crucial impact on the relative growth extent once it passes certain threshold. [55]
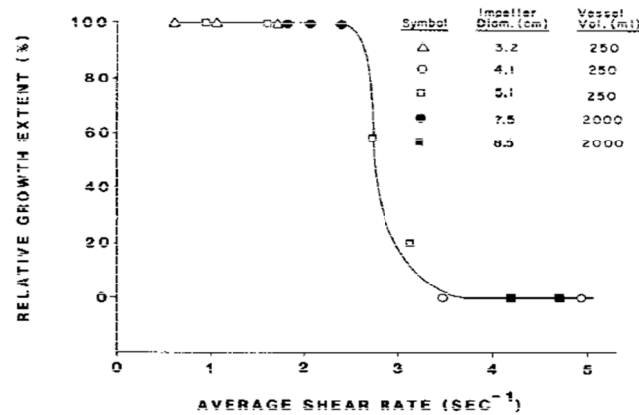
Figure 5-3. Relative growth extent of FS-4 cells vs. average shear rate [55]

Because of the constraints discussed above, here a novel design is proposed, which could be able to potential reduce the time and space cost, eliminate the gas sparging issue which kills cells, and increase the surface area / volume. Figure 5-4 shows the surface area / volume value for the cell factory, wave bioreactor, dialysis bioreactor, and the perfusable membranes. The number for cell factory is pretty low because the separation between two layers is as big as 1 inch, in order to maintain the oxygen demand. The wave bioreactor is higher but still limited by the micro-carriers amount and shear force. The perfusable membranes is very promising because it can have much better surface area / volume value, which means much higher cell density.
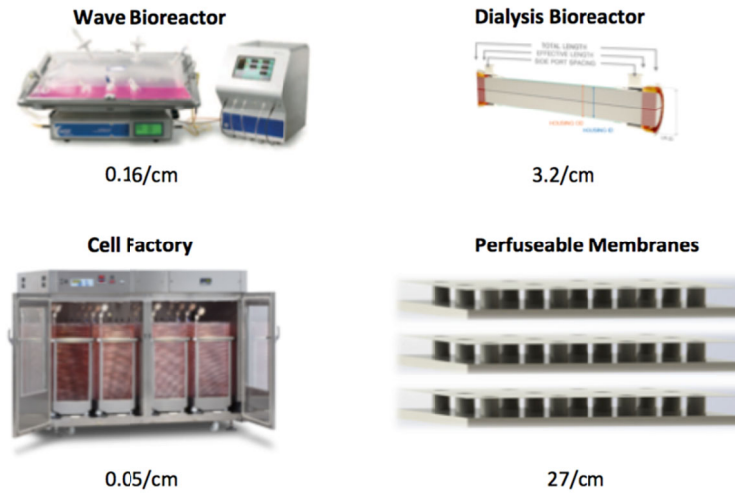
Figure 5-4. Comparison on surface area / volume value

5.3 Design

5.3.1 Material design

Instead of commercialized flasks, bioreactors, and roller bottles, we choose parylene as our material, to which cells adhere and attach. As discussed in chapter 2, the good biocompatibility, mechanical properties, and MEMS compatible machinability make parylene the perfect material for cell culture. However, in order to have cell attachment, the surface of parylene needs to be modified. The contact angle of as-deposited parylene-C is around 80 degree, which needs to be lowered for cell growth. The CV-1 cells love hydrophilic surface instead of hydrophobic. Experiment has been performed to observe the cell attachment on surfaces with different contact angles. Up to 40 degrees, cell attachment is good. For any surface with contact angle larger than 70 degree, there will be no cell attachment. In order to make the parylene surface hydrophilic, plasma treatment method is applied. As discussed in chapter 2, different

combinations of gases have been tested and cell growth experiments have been done on different treated surfaces. CV-1 Cell numbers are counted every day up to 3 days. From Figure 2-7 and Table 2-1, we can conclude that recipe B performs best, which is 50 W 200mT 3 min O2, followed by 50 W 200mT 3 min NH3. The possible explanation is that oxygen plasma will first roughen the surface of parylene and ammonia plasma will form functional groups to lower the surface energy.

After the cell attachment problem tackled, gas permeation is the next big problem to solve. Ideally stacks of parylene membrane need to be designed to save the cost, and gas can be supplied through the permeation of parylene to eliminate the gas sparging damage. Therefore we are taking advantage of ultra-thin parylene. As shown in Figure 5-5, when parylene goes thinner in submicron region, the permeability goes dramatically higher. Therefore, it is possible to supply mixed gas from the other side of the ultra-thin parylene membrane and let the gas permeate to the attached cells. More details on the permeability will be discussed in the next section.
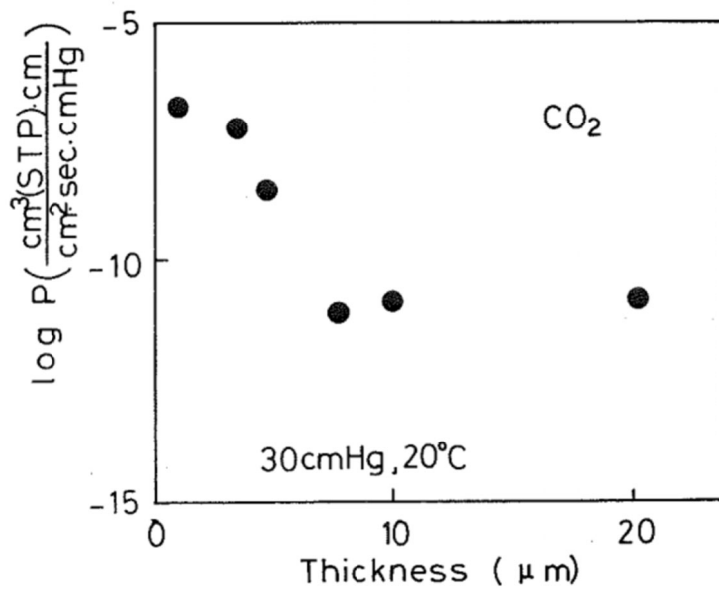
Figure 5-5. Permeability coefficient of CO_2 as a function of parylene thickness [55]

However, one practical problem, which is not trivial, is that ultra-thin parylene is very hard to handle. It always breaks accidentally because it is so thin. Therefore, we come up with the ultra-thin parylene-on-PDMS structure. PDMS is porous so it won't be the major barrier, which is proved in the following section. We choose to apply the biocompatible silicone MED4-4210. After fully cured and leached, it won't release harmful chemical that strong enough to affect cell growth, which is also proved by experiments. The details on structure design are presented in the next section.

5.3.2   Structure design

Figure 5-6 shows the concept of single layer cross-sectional structure design. PDMS chamber is fabricated first and ultrathin parylene is coated. Gas flows through the chamber and permeates out. Figure 5-7 shows the 3D concept with gas flow and cell attachment. PDMS pillars are designed for mechanical support to prevent the whole device from bulging when pressure is applied.
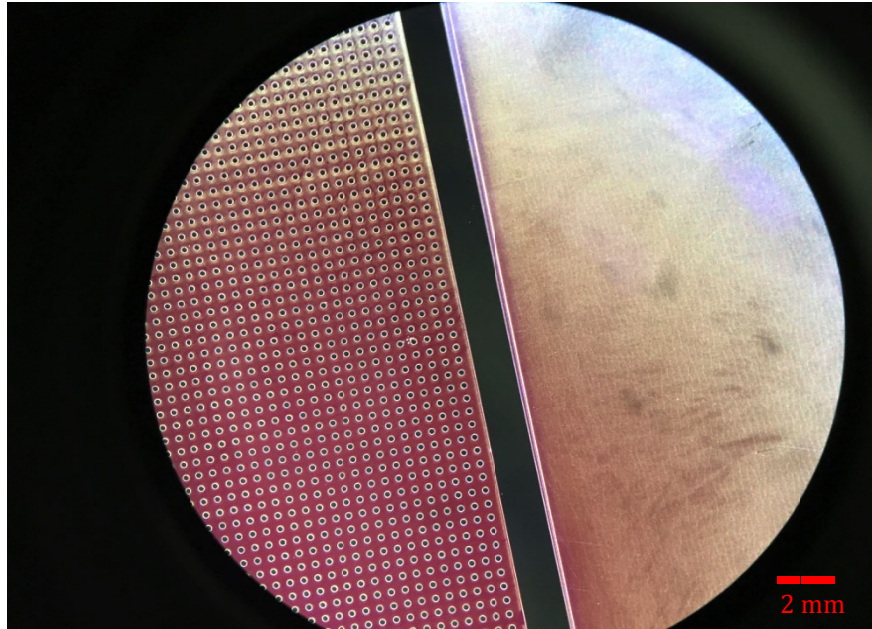
Figure 5-6. Picture of dry-film modes.
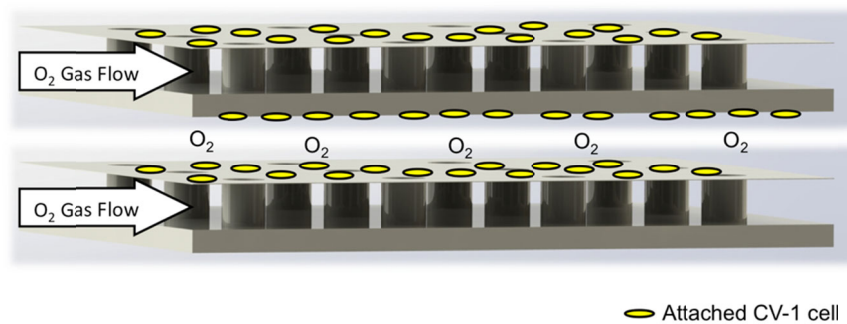
Figure 5-7. Concept of two layers 3D structure design with gas flow and cells attached.

5.4 Fabrication

The fabrication process starts from making the mold for PDMS. 5 cm by 5 cm area is designed and 1 layer of dry film photoresist is used. The top and bottom PDMS molds are made separately. After both top and bottom sheets are fabricated, they will be aligned and bonded together to form the PDMS chamber.

The part A and part B of the PDMS MED 4-4210 are mixed with a 10 to 1 ratio in weight. After mixing them well, 20 minutes degasing process is followed to take out bubbles trapped inside. Then the uncured PDMS is poured on to the mold. After half curing, the film is peeled off from the mold and the top and bottom pieces are bonded together (Figure 5-8, 5-9, 5-10).
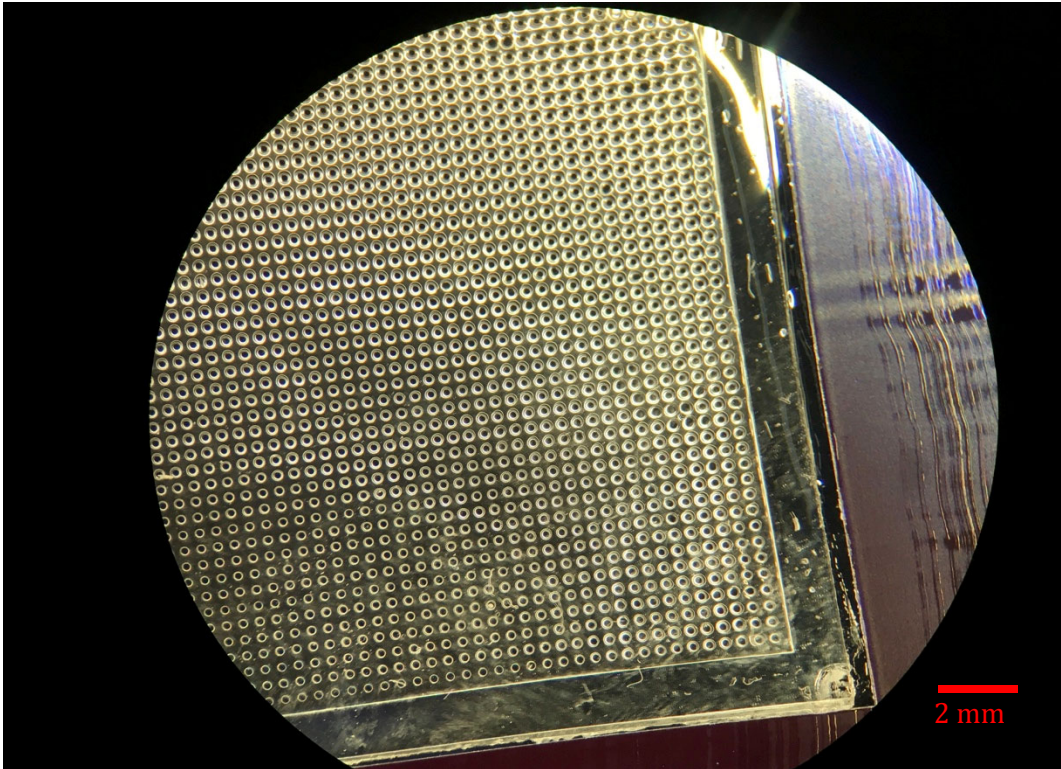
Figure 5-8. PDMS device after assembly and gluing top and bottom pieces together.
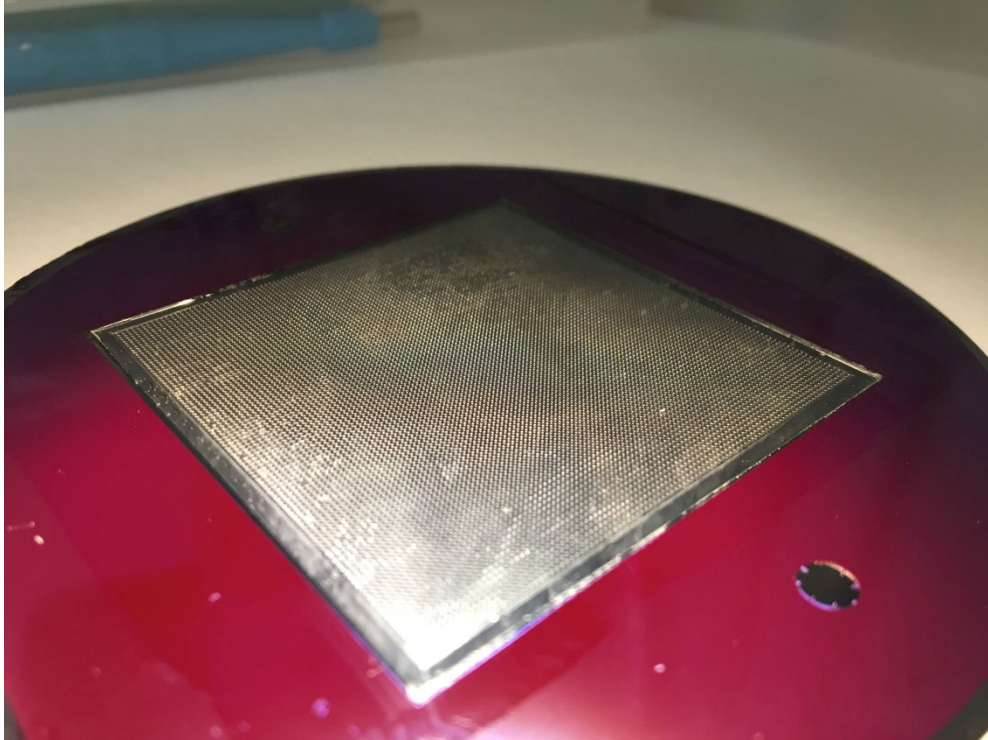
Figure 5-9. Overview of PDMS device.
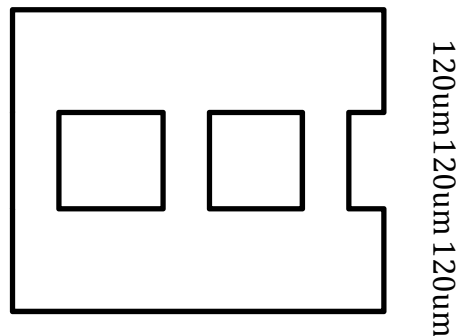
Figure 5-10. Cross-sectional structure of the PDMS device.

The PDMS bag is then fully baked at 150 degree C for 2 days, followed by leaching in acetone at 90 degree C for 3 days. These two steps are crucial for the PDMS not releasing too much harmful chemicals to the cells. After the PDMS bag is ready, connections are made to it by inserting two tubing into the hallow space, and sealed with also PDMS (Figure 5-11). Then the devices, together with the tubing, are coated with thin

parylene.
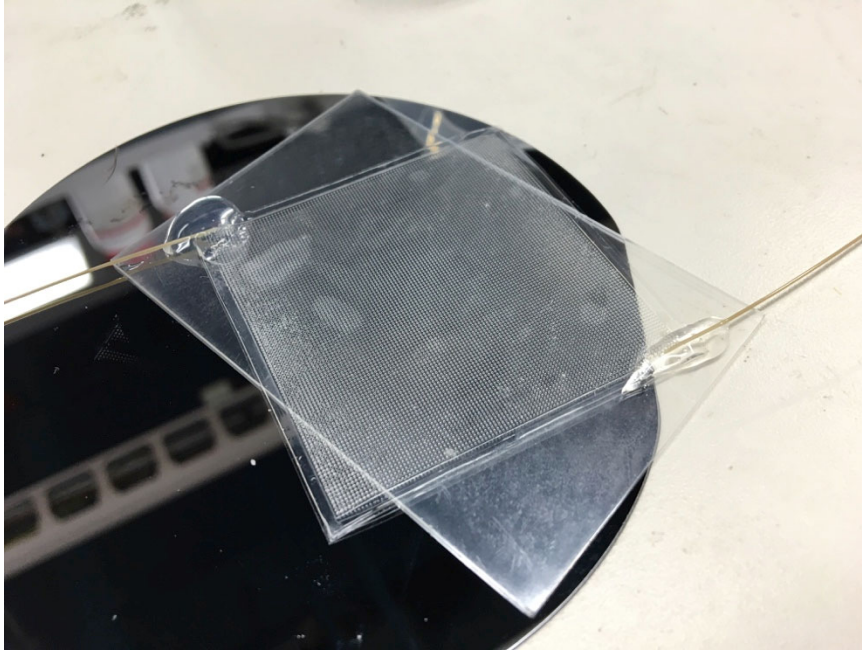
Figure 5-11. 310um PEEK Tubing Inserted.

After thin-parylene is coated, Oxygen followed by ammonia plasma is used to treat the surface of parylene, as discussed before.

Finally, resazurin dye is applied to test the oxygen permeation after the device is connected to oxygen supply, as shown in Figure 5-12. Red color change is clearly seen on the membrane of the device, which indicates that the oxygen does perfuse out. Detailed study on the permeation of oxygen will be discussed in the following sections.

Figure 5-12. resazurin dye study to verify oxygen permeation.

5.5   Oxygen permeation study

Oxygen permeation is studied quantitatively in this section. The device is at the bottom of the dish and covered with 5mm water in depth. Oxygen gage pressure is maintained at 1 psi at the inlet port and 100% oxygen continues flow during the test. Oxygen sensing probe touches the device surface in order to be as accurate as possible (Figure 5-13). Figure 5-14 illustrates the structure of the model and Figure 5-15 shows the calculation of oxygen concentration on the parylene surface. Because the parylene penetrates into the porous PDMS, therefore it is hard to preciously predict the exact structure. Here in Figure 5-15, three assumptions on the permeability of the 0.6um are made and the corresponding oxygen concentrations are calculated. If the permeability of thin parylene is treated the same as bulk parylene, 84% is achieved. If it is treated as 3 times permeability of bulk or porous, 93% or 99.95% can be achieved. The experimental result is shown in Figure 5-17. The oxygen level saturates at around 90% so the calculation of oxygen concentration is pretty accurate.
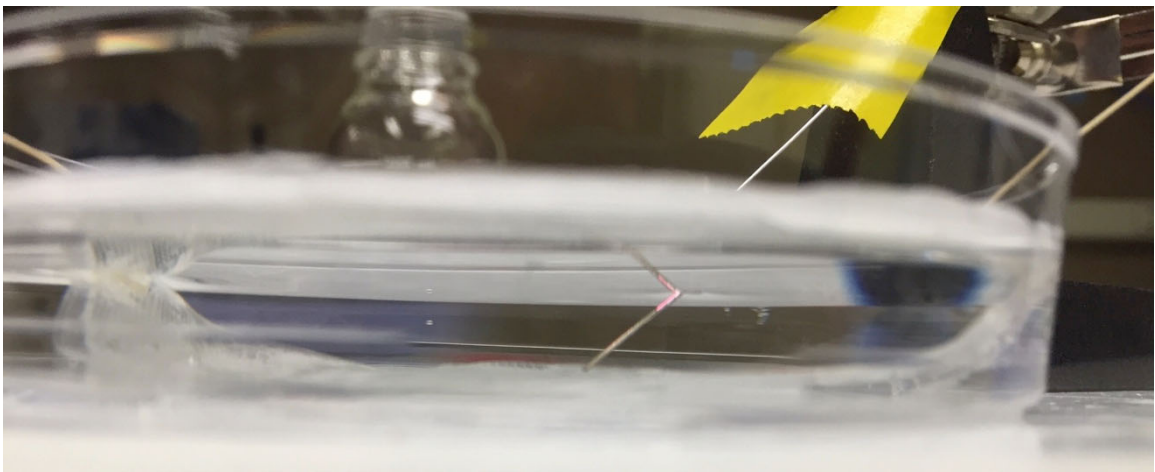
Figure 5-13. Setup of oxygen permeation test
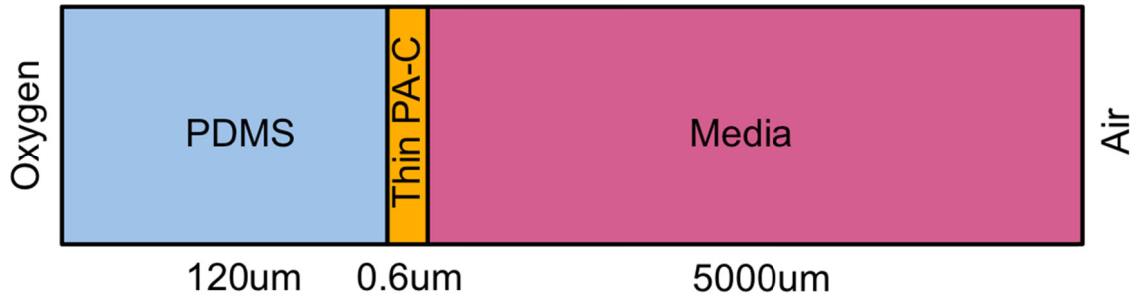
Figure 5-14. Structure for modeling.
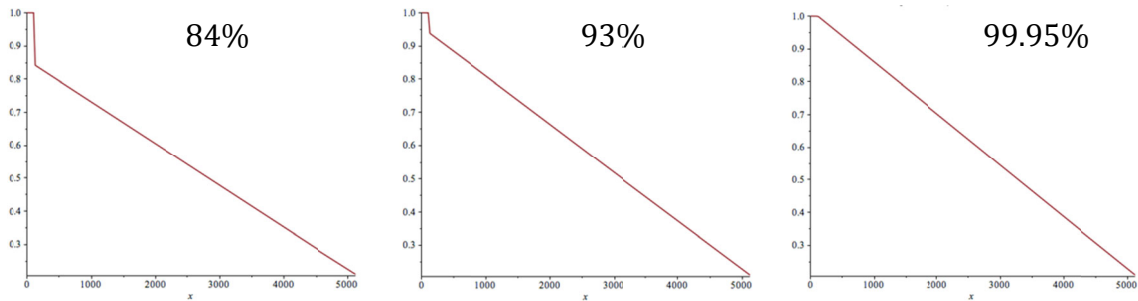
Figure 5-15. Modeled oxygen concentration on the parylene surface. Left, treating the thin parylene as bulk. Middle, treating the thin parylene as 3 times permeability of bulk. Right, treating the thin parylene as porous. 84%, 93% and 99.95% oxygen concentration are predicted for each case.

$$\cdot \, Dpdms := 1.6 \cdot 10^4 \; \# \left[\frac{um^2}{s} \right] \; diffusion \; of \; oxygen \; \textbf{in} \; PDMS :$$

$$\cdot \, Dh2o := 2.1 \cdot 10^3 : \# \left[\frac{um^2}{s} \right] \; diffusion \; of \; oxygen \; \textbf{in} \; water :$$

$$\cdot \, Dpac := 2.5 : \# \left[\frac{um^2}{s} \right] \; diffusion \; of \; oxygen \; \textbf{in} \; water$$

$$\cdot \, Hpdms := 1.12 \cdot 10^{-17} : \# \left[\frac{mol}{um^3 \cdot atm} \right] \; solubility \; of \; oxygen \; \textbf{in} \; PDMS$$

$$\cdot \, Hh2o := 1.3 \cdot 10^{-18} : \# \left[\frac{mol}{um^3 \cdot atm} \right] \; solubility \; of \; oxygen \; \textbf{in} \; water$$

$$\cdot \, Hpac := 5.3 \cdot 10^{-19} : \# \left[\frac{mol}{um^3 \cdot atm} \right] \; solubility \; of \; oxygen \; \textbf{in} \; bulk \; PA - C$$

$$\cdot \, Hair := 40.81 \cdot 10^{-18} : \# \left[\frac{mol}{um^3 \cdot atm} \right] \; solubility \; of \; oxygen \; \textbf{in} \; air$$

Figure 5-16. Parameters for calculation.
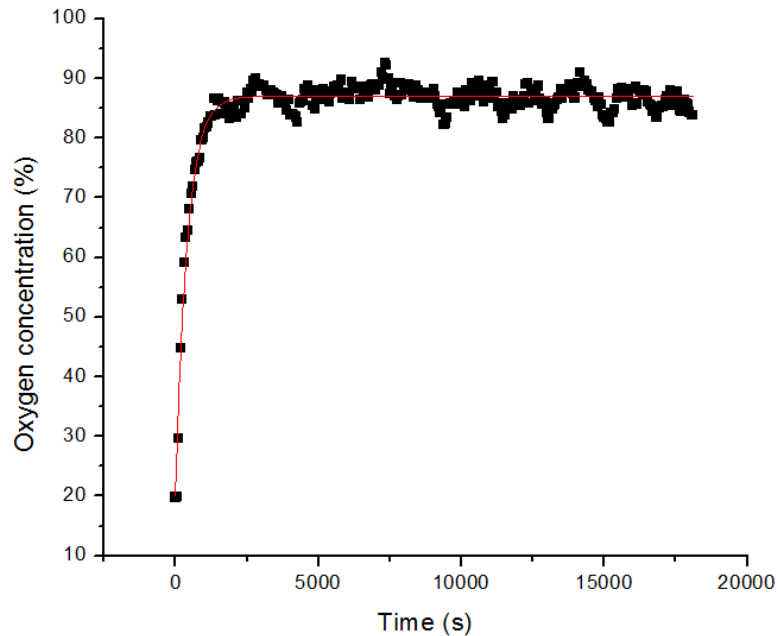
Figure 5-17. Experimental oxygen permeation test

5.6   Results and discussion

5.6.1   1ˢᵗ experiment

Oxygen free environment was created for the 1ˢᵗ experiment, from which we want to test the extremely worst case, where no oxygen is supplied from the environment, and the only gas source is supplied from the device. In order to create this oxygen free environment, the device was kept inside the O-ring sealed contained with oxygen absorbers inside to consume oxygen. The oxygen probe went inside of the container through the lid to measure the oxygen level decay (Figure 5-18). The result does show that the oxygen-free container can be kept at very low oxygen level.
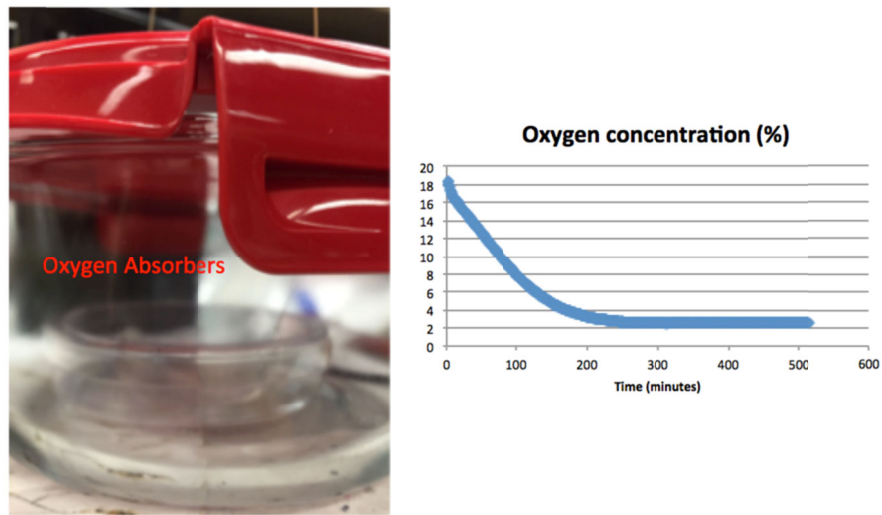
Figure 5-18. Oxygen-free setup and oxygen concentration test to prove the oxygen drop.

3E6 CV-1 cells have been seeded (Day 0) onto A, parylene-on-PDMS device with mixed oxygen and carbon dioxide gas supply (normoxic) and B, parylene-on-PDMS device without gas supply (normoxic) and C, parylene-on-PDMS device in oxygen-free container (anoxic). After 3 hours of seeding, the cells in all conditions (Normoxic, Anoxic) begin attaching (Figure 5-19) After one day (Day 1), cells attached and spread all over confluently on both normoxic devices A and B (Figure 5-20), and cells detached and lysed on device C (Figure 5-21). This result showed that the cells didn't survive the oxygen free environment without any other gas sources.
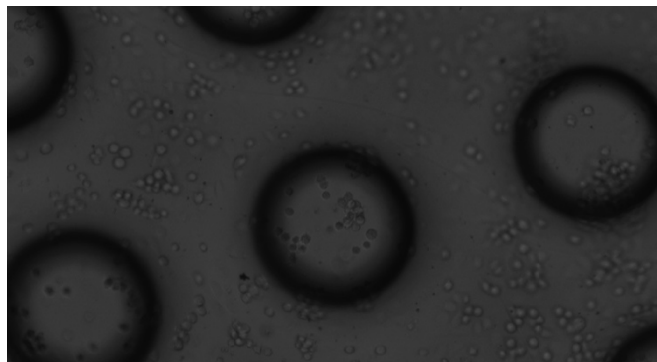
Figure 5-19. After 3 hours all Conditions (Normoxic, Anoxic) begin attaching
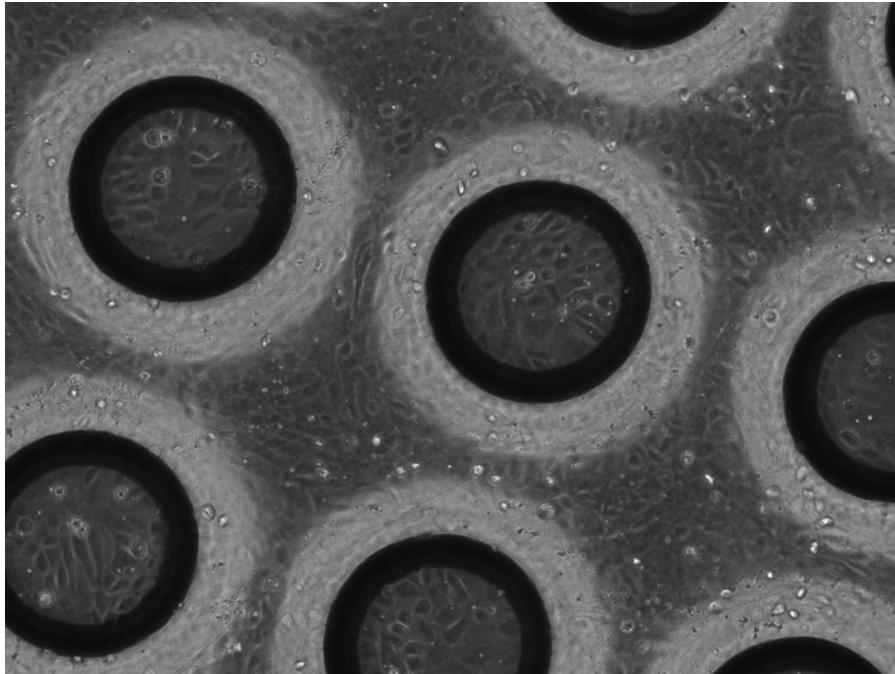
Figure 5-20. CV-1 cells attached and spread confluently on both parylene-on-PDMS devices (normoxic)

Figure 5-21. CV-1 cells detached and lysed after 24 hours for sample C (anoxic)

On Day 1, both A and B were moved into oxygen free environment. A was still connected with gas supply while B wasn't. After one day (Day 2), the cells on B detached from the parylene surface and started to die (Figure 5-22), while cells on A survived (Figure 5-23). This 1st experiment proves that the parylene-on-PDMS device with mixed gas supply can provide enough gas to sustain the cells even in the extreme oxygen free environment. This is the extreme worst case in terms of oxygen supply and the feasibility of the device is proved.
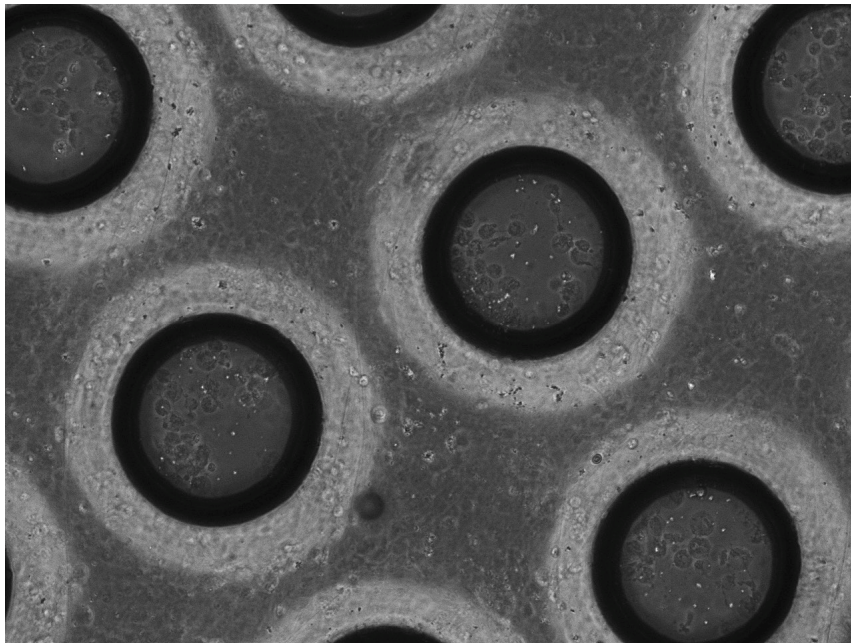
Figure 5-22. CV-1 cells detached and started to die on B without mixed gas supply in the oxygen free environment (anoxic) after 1 day
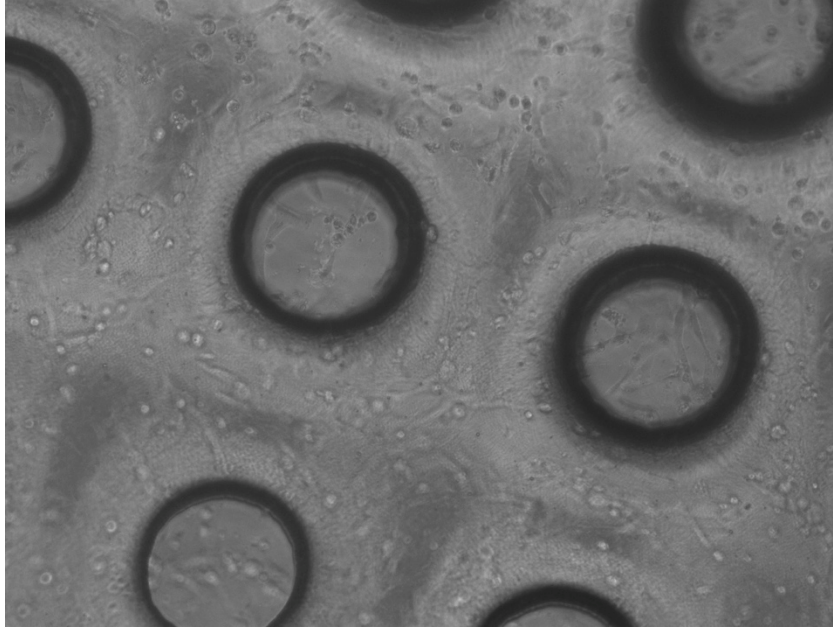
Figure 5-23. CV-1 cells survived on A with the mixed gas supply (anoxic + perfusion O_2)

5.6.2　2nd experiment

In the 2nd experiment, 3E5 CV-1 cells are seeded onto 3 samples: A, parylene-on-PDMS device with mixed oxygen and carbon dioxide gas supply; B, parylene-on-PDMS device without gas supply; and C, regular 10 cm cell culture dish. The starting cell density was 3820-cells/cm^2 Counting cells measured cell growth two days later. The resulting cell densities were: A, 7523 cells/cm^2; B, 7200 cells/cm^2 and C, 7130 cells/cm^2. The result is plotted in Figure 5-24. Considering the error during cell counting, there is no statistically significant difference among theses 3 conditions. This result indicates that under normal incubator environment, the oxygen and CO_2 supply is abundant. Therefore, more oxygen supply from the devices won't increase the cell growth rate. On the other hand, combining these two experiments, we can conclude that the device with oxygen

supply does deliver gases to the attached cells, which reaches the goal. The next step will be making stacks of the devices to truly improve the cell culture density.
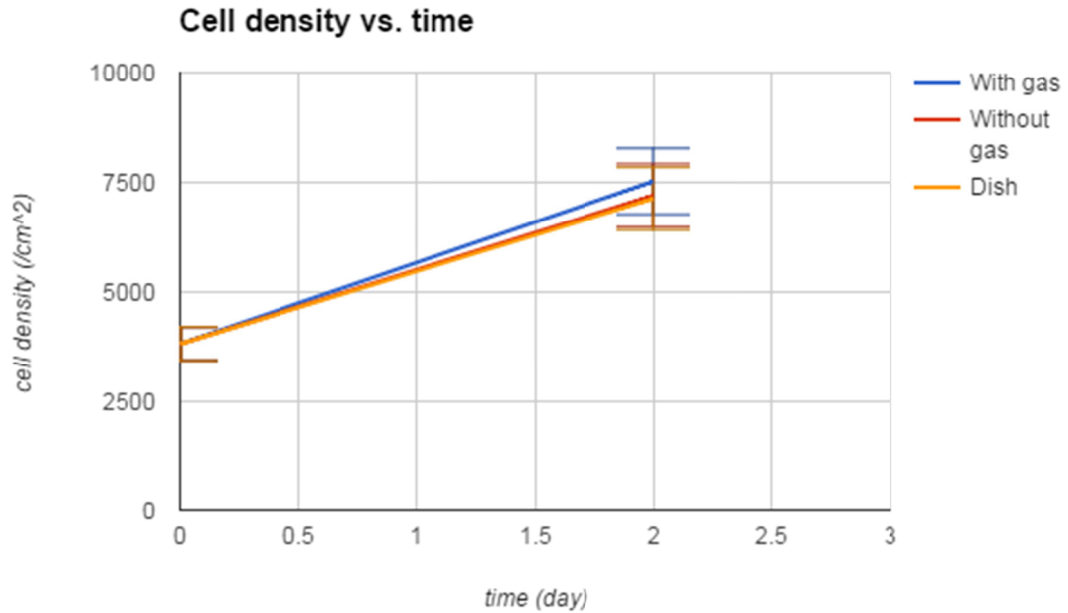
Figure 5-24. Cell density vs. time for 3 different conditions.

5.7   Conclusion

In this chapter a novel parylene-on-PDMS device is presented. The motivation is to innovatively increase the large-scale vaccine production efficiency. More specifically, this device is designed to improve the cell culture part by reducing the cost and solving the gas sparging issue. Ideally, by stacking the membranes together, high cell density can be achieved. Here we have demonstrated that the gas can be delivered to the cells and cells have attached and grew well. The feasibility of one single piece of membrane has been demonstrated, and the next step should be making stacks of the membranes to increase the cell density.

5.8   Reference

[51]   S. Vallius. Large scale amplification and purification of replication competent vaccinia virus, 2012

[52]   G. L. Smith, A. Vanderplasschen, M. Law. The formation and function of extracellular enveloped vaccinia virus, *Journal of General Virology*, 83(12), pp. 2915-2931, 2002

[53]   L. J. Ausubel, M. Meseck, I. Derecho, P. Lopez, C. Knoblauch, R. McMahon, J. Anderson et al. Current good manufacturing practice production of an oncolytic recombinant vesicular stomatitis viral vector for cancer treatment, *Human gene therapy* vol 22, pp. 489-497, 2010

[54]   Y. Chisti, Animal-cell damage in sparged bioreactors, *Trends in biotechnology*, vol.18, pp. 420-432, 2000

[55]   M. S. Croughan, J. F. Hamel, and D. I. Wang, Hydrodynamic effects on animal cells grown in microcarrier cultures, *Biotechnology and bioengineering*, vol. 67, pp. 841-852, 2000

[56]   A. Tanioka, N. Fukushima, K. Hasegawa, K. Miyasaka, and N. Takahashi, Permeation of gases across the poly (chloro‑p‑xylylene) membrane, *Journal of applied polymer science*, vol. 54, pp. 219-229, 1994

6 PARYLENE ORIGAMI STRUCTURE

6.1 Introduction

This chapter introduces a novel design to fold a 2D parylene membrane into 3D structures. With pre-designed folding crease patterns, the final shape after folding can be controlled. This technique will be useful under the specific circumstances where certain shape is required for the parylene based device to match the curvature of objects, like the curvature of organs (in this chapter the human eyeball curvature as a perfect example), and where the surface area per volume of parylene needs to be increased, for instance, the vaccine productions project from chapter 5, where we would like to push the cell density to the limit, in order to increase the vaccine production outcome. And last but not least, we are able to apply this technique to create interesting thing, like the "micro-origami US map" presented in this chapter.

Origami, the Japanese art of paper-folding, is normally thought of as primarily a decorative art. However, the techniques of origami can be applied to improve various technological problems. One that regularly arises is the need to fabricate a structure using

conventional planar fabrication processes, but then transform a planar sheet into a more complex three-dimensional form with origami technique. Theoretical algorithms for origami design may be used to effect this transformation. One such opportunity arises in the field of retinal implants. Here, a thin-film microelectronic circuit comprising an artificial retina may be formed from a biocompatible polymer (e.g., parylene) using planar thin-film processing. When implanted, though, the electrode array must be formed into a shape compatible with the approximately spherical curvature of the back of the eyeball so that the electrode can be in close contact (typically a few tens of microns) with the retinal surface. The origami design problem, then, becomes one of finding a folding pattern that transforms a thin planar surface into a shape conformal to a spherical surface.

The general approach for designing such a folding pattern is well known in the field of origami. In fact, it is possible create origami versions of an arbitrary surface of rotation. Of course, it is not possible to achieve perfect conformation to a surface with net Gaussian curvature; a planar film has zero curvature, and any shape folded from same must have zero Gaussian curvature except along a finite set of points and lines. However, it is possible to come arbitrarily close to a smoothly curved surface with a finite polyhedral folded form, and all that is necessary is that the folded shape fall within the mechanical tolerance required by the retina.

Here, we present the novel method of folding a fully-released 2D micro-fabricated parylene-C device with a designed folding crease patterns to a 3D spherical origami structure to achieve an origami retinal implant fitting the original curvature inside the eyeball [57]. Therefore, the origami implant design enables the possibility of first making an extended device in 2D format and, after a possible minimal surgical cut and insertion,

then folding it into a 3D device inside the eye for necessary geometric matching with host tissues. Prosthetic retinal implants have been modelled in FEA simulations before [58]. The use of a creased thin-film substrate, however, presents a unique challenge. Woo et al [59, 60] have modelled creases as a kink in undamaged film using 2D shell elements and also using 2D solid continuum elements to obtain a crease cross-section. Neither approach is suitable in our case as we need the full 3D shape and the film thickness and crease radii are on the same order as the desired implant-retina separation distance. We developed an FEA model to investigate how these effects alter the implant's convex surface.

In this work, parylene-C is chosen to be the material for the origami structure. Due to its high biocompatibility, good mechanical strength, and machinability, parylene-C has become a good candidate as the material for implantable devices. Recently, studies of parylene-C based retinal implantable devices have been reported for the treatment of age-related macular degeneration. This paper then reports the first 3D spherical PA-C origami folded from a 2D film with pre-designed folding crease patterns.

6.2   Motivation

Geometric matching is crucial for electrical stimulation applications, especially retinal prosthesis. The implant is meant to partially restore vision to people who have lost their vision due to retinitis pigmentosa or macular degeneration et cetera. Among 3 types of retinal implants currently in clinical trials (epiretinal, subretinal, suprachoroidal), epiretinal implants (on the retina) are able to provide the recipient with images by electrically stimulating surviving retinal cells for light perception and object recognition.

However, one problem that remains unsolved is to fabricate a spherical epiretinal device with a radius of curvature that matches the retina. Here, a novel origami design is demonstrated that solves this problem by folding a 2D device into 3D spherical structure with pre-designed curvature.

| 100µm | EHT = 15.00 kV | Signal A = SE2 | Date :14 Nov 2012 |
| | Mag =   100 X | WD =   15 mm | Time :10:50:06 |
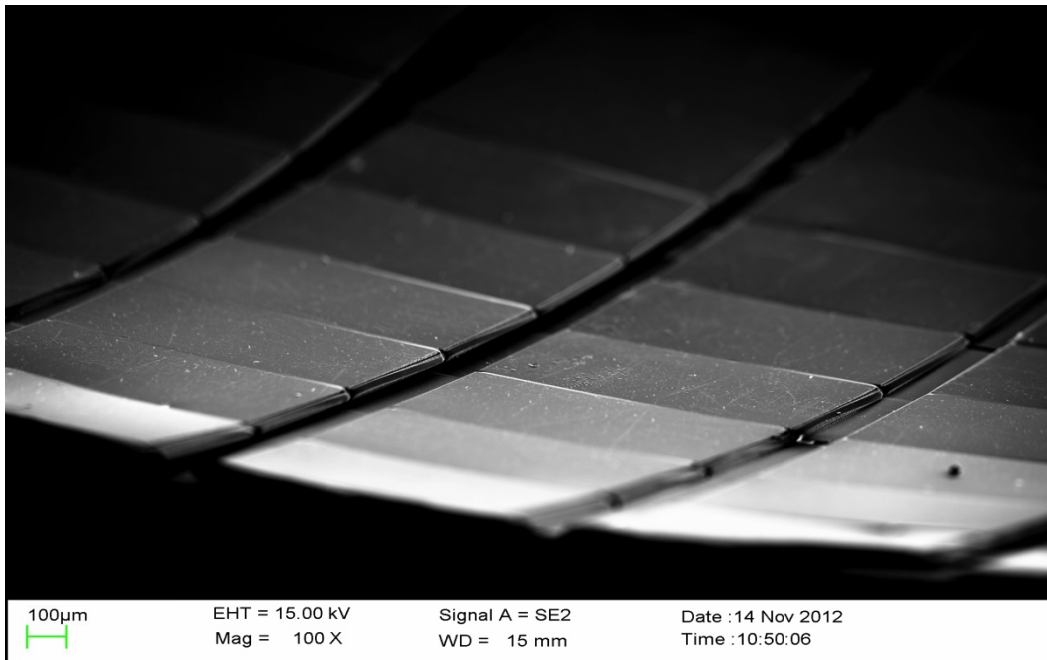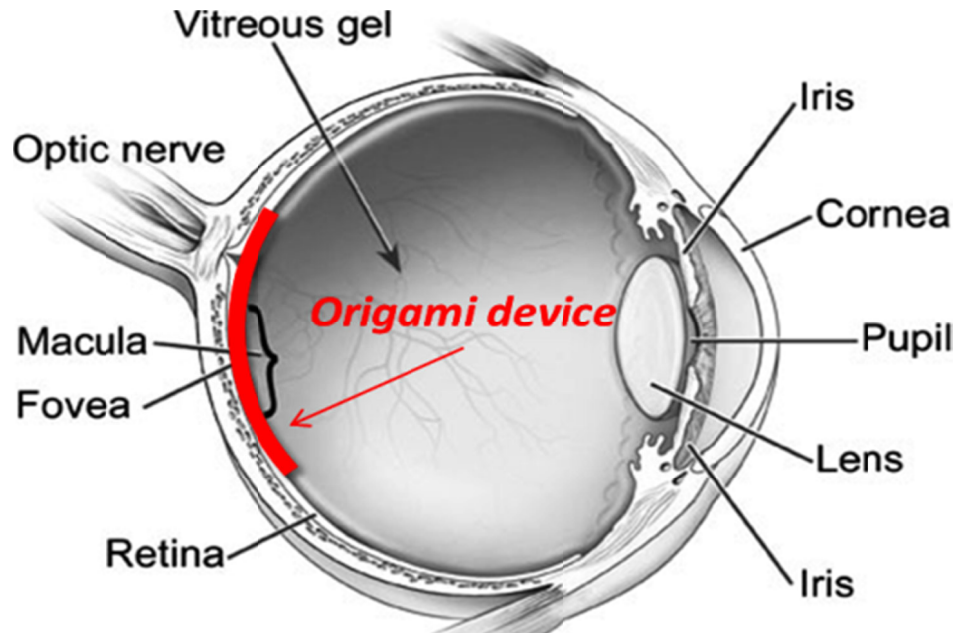
Figure 6-1. Top, Origami device for intraocular implant: curvature needed to closely appose device to the retina. Bottom, SEM image of parylene-C origami structure

Here, we have designed and developed a micro-origami implantable device for retina prosthesis (Figure 6-1), and demonstrated it with a micro-scaled 3-dimensional (3D) United State (US) map. The origami device is a way to construct a 3D spherical structure from a micro-fabricated-2D parylene-C (PA-C) in order to implant the intraocular epiretinal device, which requires a curved electrode array to fit the curvature of the macula. The US map in 2D was patterned with Ti/Au on PA-C film and assembled to spherical structure after folding. Crease-lines for sphere are mathematically designed and patterned, and then thin silicone oil is used as a temporary glue to hold the folded structures through surface tension. The temporary origami is then thermally set into permanent 3D shapes at 100∘C for 30 minutes in vacuum utilizing the viscoelastic properties of PA-C. The reported origami technique enables the possibility of first making an extended device in 2D format and, after a possible minimal surgical cut and insertion, then folding it into a 3D device inside the eye for necessary geometric matching with host tissues.

6.3 Design

As shown in Figure 6-2, the crease patterns consist of curved lines. Once folded along the curved lines with the right sequence, the designed 2D film can turn into a spherical structure. These crease lines are designed by mathematics and computer simulation. The simulation is run within a multi-objective optimization loop, which

minimizes the contact pressure on the retina by changing parameters such as width and thickness of crease regions.
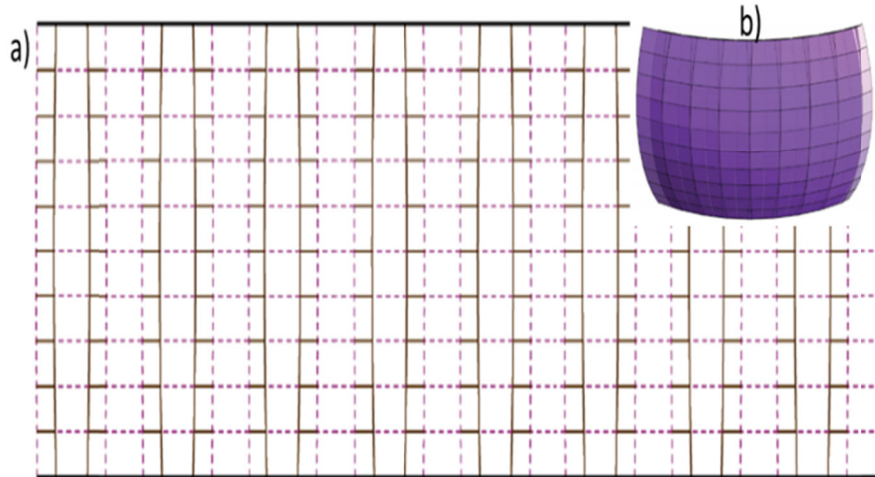
Figure 6-2. a) The crease pattern: crease lines are curved; b) conceptual model of final device.

6.3.1   Modeling

Computational algorithms for designing thin-flange structures have been presented by Lang [61] and Mitani [62]; an algorithm for Mosely's thick-flange concept was presented by Mitani [63]. Here we present a further generalization that incorporates additional design elements, in particular gaps to accommodate material thickness and tolerances and a continuously variable parameter defining the configuration of the flanges around the outside.

The basic concept is straightforward. Imagine wrapping an orange with a sheet of paper. There are several ways this could be done. We could place the orange on top of a flat sheet, then gather the edges up around it to meet at the top, or we could wrap the sheet around it to form a cylinder, then gather the excess together at both top and bottom.

Both approaches have been described; the second has the advantage that it distributes the excess material more evenly, and so it is the approach that we will adopt going forward.

We note that for a truly spherical surface, the sheet could assume a smoothly curved form in one direction, but because the sheet is a developable surface, its Gaussian curvature must be zero; there must be some direction along which the sheet is straight in 3D (that is, it must be a ruled surface). Nevertheless, we can approximate any curved surface to arbitrary precision by creating a polygonal approximation to the surface. We will assume an m-fold rotational symmetry in the axial direction, and then an arbitrary order-n quantization in the vertical direction.

If one were allowed to cut the paper, we could imagine wrap- ping a sphere by creating a series of polygonal "gores", like the segments of a beach ball, each of which subtended a fixed angle about a vertical axis of symmetry, as illustrated in Figure 6-3.

Now, in order to create this structure from a single sheet, we must somehow gather the paper that lies between the gores so that it (a) brings the edges of the gores together, and (b) remains a developable surface. The second condition implies specifically that isometry exists between the flat (unfolded) and 3D (folded) surfaces.

A simple way of gathering the excess paper is to simply fold the surface halfway between consecutive gores and along one side of each gore, resulting in a series of flanges pointing ax- ially around the surface, flanges whose width is zero at the equator of the sphere and increases monotonically toward top and bottom, as illustrated in Figure 6-4.
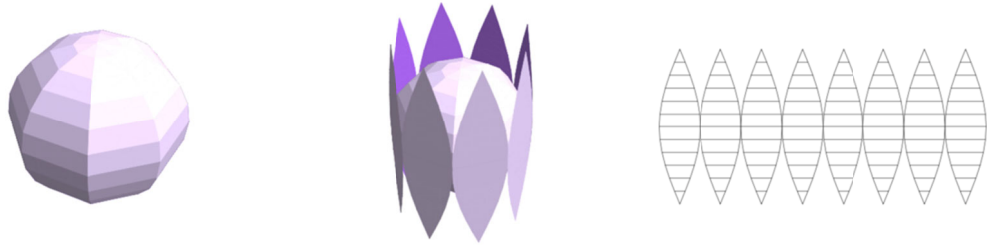
Figure 6-3. Left: Schematically of a rotationally symmetric polygonal approximation of a sphere (8-fold rotational symmetry). Middle: unwrapping the gores. Right: the 2D unwrapped gores that make up the surface.
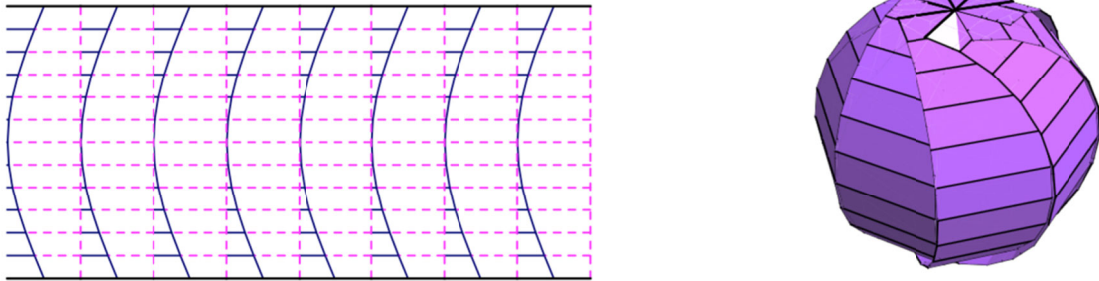
Figure 6-4. Left: crease pattern for an axially wrapped sphere. Right: the 3D sphere.

Here we show the sphere model before and after folding in Figure 6-5. For a retinal implant, we only need a segment of the finer grained sphere. The 5 segment of crease pattern and folded form is shown in Figure 6-6.
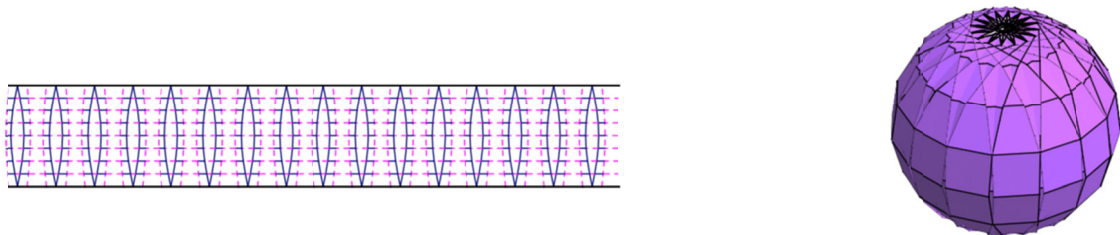
Figure 6-5. Left: crease pattern for the sphere. Right: folded form.
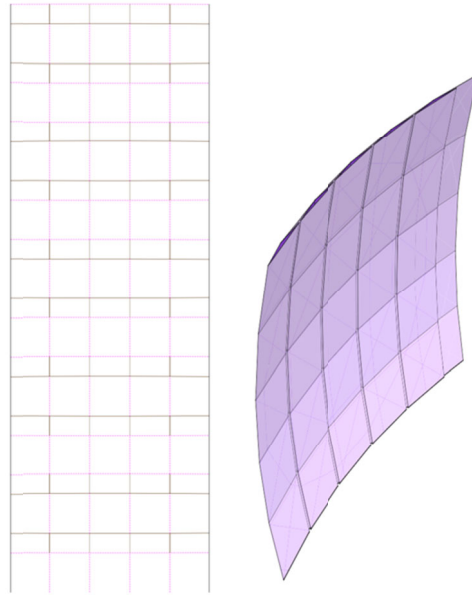
Figure 6-6. Left: crease pattern for the implant. Right: folded form.

6.3.2 Device and process design

The extended 2D film is a 20-μm-thick PA-C film with 3-μm-thick crease region (Figure 6-7f). Since we need both convex fold and concave fold, the width of right crease region is set to be 30 μm (for concave fold), while the width of left crease region is set to be 10 μm (for convex fold). The left crease region folds in the opposite direction of the right crease region, forming a Z-shaped stack as shown from Figure 6-7f to Figure 6-7g.
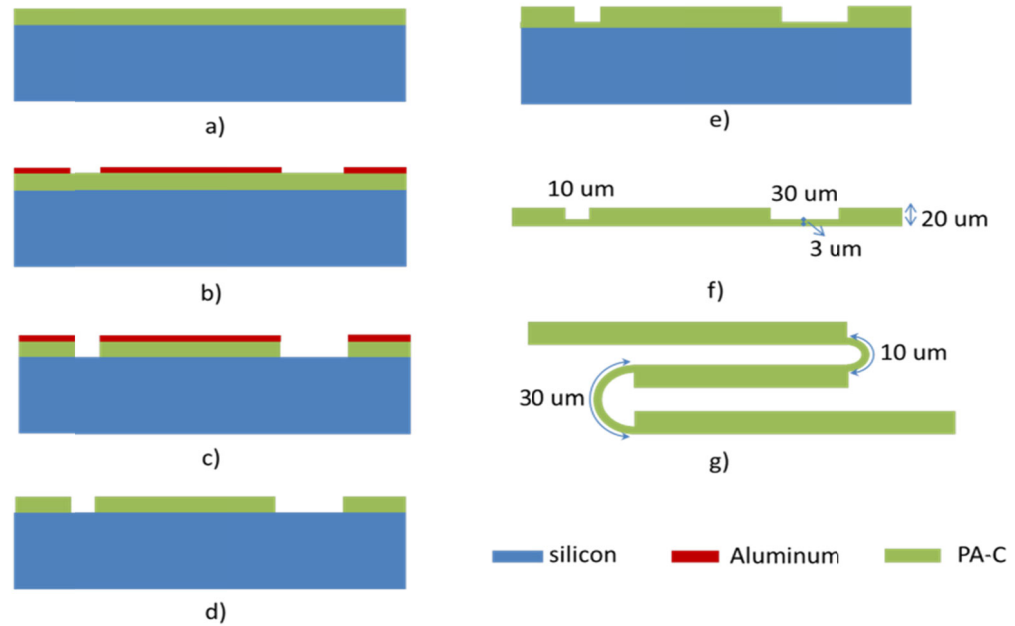
Figure 6-7. Fabrication and folding process. a) Deposition of 1st PA-C layer; b) Al patterning; c) oxygen plasma etching; d) getting rid of Al; e) deposition of the 2nd PA-C layer; f) Origami film separated from the silicon wafer; g) mechanical folding of the origami film. Note the difference between the convex and concave folds.

Figure 6-8a shows the fabricated device before and after folding. Perfect spherical structure can be achieved. Figure 6-8b demonstrated that because the radius of the device is controlled, after folding, it could attach to the spherical surface closely, while a piece of 2D parylene sheet couldn't and wrinkles appear.
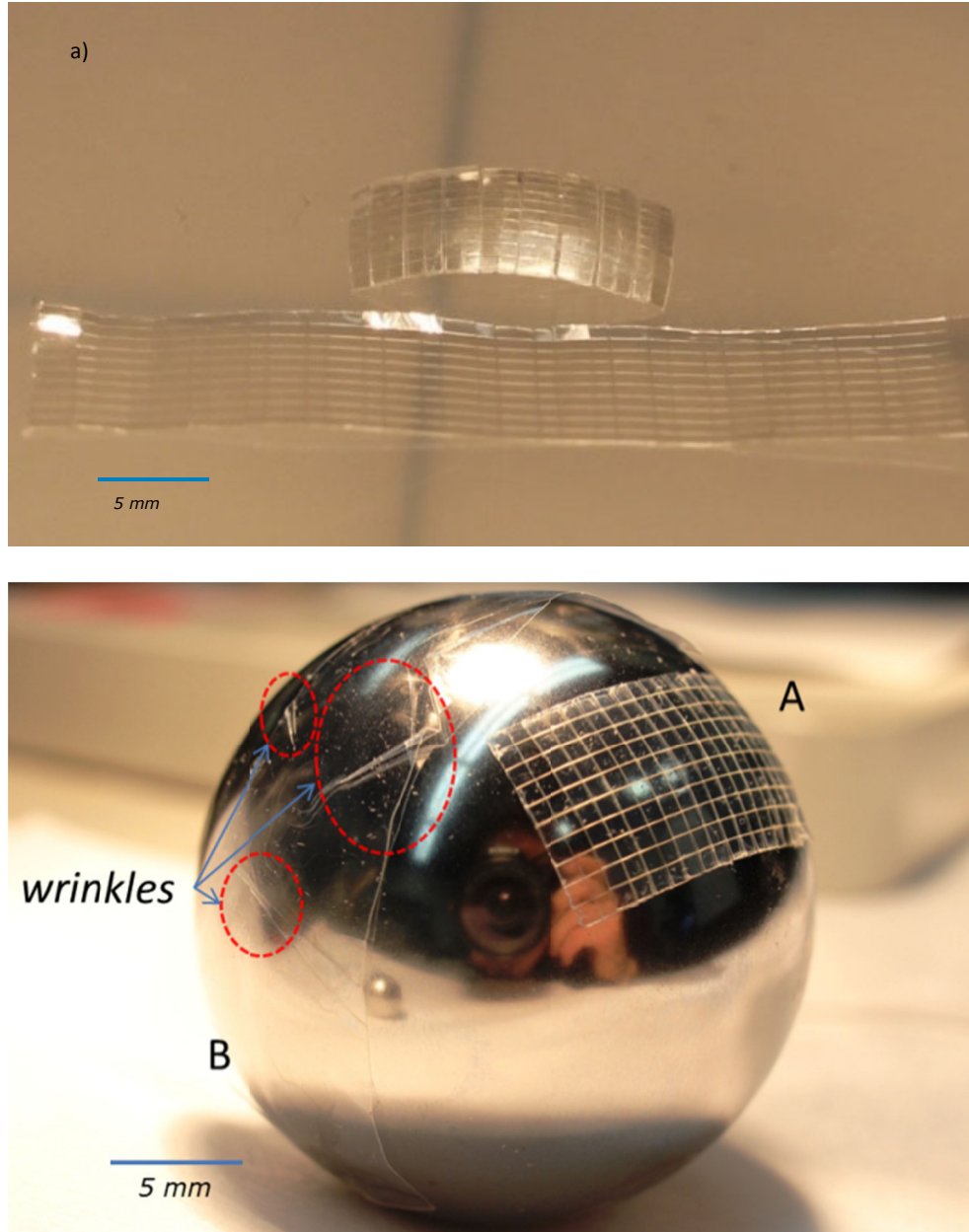
Figure 6-8. a) Spherical parylene-C structure after folding (top) and 2D patterned parylene-C film before folding (bottom); b) A and B have the same dimensions in 2D. A has crease pattern while B does not. When folded to sphere surface, A can fit the surface curvature precisely while B cannot.

6.4 Fabrication of Parylene Membrane

Figure 6-7 shows the fabrication process of the origami film. A 4-inch wafer is prepared for fabrication after piranha plus buffered hydrofluoric acid (BHF) cleaning, and then hexamethyldisilazane (HMDS) treatment respectively. A 17-μm-thick PA-C film is then deposited over the wafer (Figure 6-7a). Next, a 0.1μm-thick aluminum (Al) is thermally evaporated over the PA-C and the photoresist to pattern Al as a plasma etching mask is exposed and developed (Figure 6-7b). Oxygen plasma (400W, 300mT) is used to etch through the openings on PA-C film all the way down to silicon surface (Figure 6-7c). The openings on the PA-C film define the crease lines. After removing Al etching mask in Al etchant (Figure 6-7d), another run of oxygen plasma (50W, 200mT, 1 minute) is used to roughen the surface of PA-C, followed by a 30-second BHF cleaning to make the surface hydrophobic. A final 3-μm-thick layer of PA-C is deposited over the device (Figure 6-7e). Finally, a dicing saw is used to cut the origami wafer into dies and the PA-C origami films are peeled off from silicon in DI water.

6.5 Folding Method and Process

The method and process of the parylene origami folding is presented here. The PA-C film is peeled off from the wafer and attached on a stainless steel ball (20 mm in diameter). To enable the attachment and the following folding, the ball surface is first covered with silicone oil. This silicone oil serves as a temporary glue to provide surface tension to allow the PA-C film to stick to the ball through meniscus force. Then a one-dimensional "tent" (with the apex to be a convex fold) is picked up from the film (Figure

6-9a). The segment on the left of the tent is then pushed inward as in Figure 6-9b and the convex fold is finished. Because of the silicone oil, the left part can be pushed inside easily, while the right segment remains unmoved. Then, the closed tent is tilt to the left side to finish the concave fold on the ball surface (Figure 6-9c). The process repeats itself until the whole origami film is folded. Figure 6-8a shows the origami structure before and after folding. In Figure 6-8b, spherical origami device (A) is compared to PA-C film without crease patterns folded onto a ball (B). (A) can fit the surface curvature precisely while (B) cannot. Wrinkles and bad contacts with the ball surface can be observed on (B).
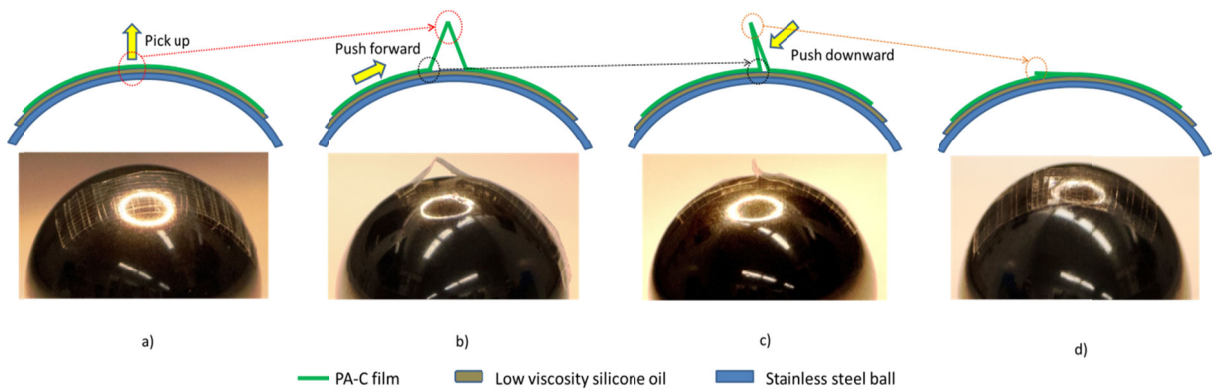
Figure 6-9. The folding process: a) start a segment with a convex fold on the right; b) form a tent by pushing the left part to the right while the right part stays unmoved; c) tilt the squeezed tent to left on the ball surface

6.6 Thermal Fixation of the Folded Origami

After folding, the silicone oil can only hold the folded origami temporarily. We then use thermal annealing to achieve the fixation of the folded origami. The glass transition temperature (Tg) for as-deposited PA-C is 50°C and viscoelasticity happens to

fix the shape when T > Tg. However, high temperature annealing larger than 100°C in air makes PA-C brittle. Thus tensile tests of parylene-C stripes after various annealing conditions have been done to determine the suitable temperature of thermal annealing. DMA (dynamic mechanical analysis) Q 800 from TA Instruments is used for the tensile tests. Procedures are described as follows. First, raise the environment temperature to 37°C; maintain isothermal for 30 minutes; finally ramp the strain at 0.5%/minute up to 250% (PA-C samples break before reaching 250% elongation). The sample annealed at 100°C shows 76.3% elongation, while 150°C and 200°C show 10.1% and 2.5%, respectively. Therefore, PA-C films annealed at 150°C and 200°C become too brittle. Considering stretching and bending in practical surgery process, 100 °C annealing is appropriate. In addition, since the time constant of PA-C crystallization is shorter than 1 minute, so a 30 minutes thermal annealing is sufficient. Therefore, all our folded origami devices are annealed at 100 °C for 30 minutes in vacuum. There is no damage to the silicone oil we used and it can be easily removed using organic solvents such as acetone.

6.7 Potential Applications

6.7.1 Design for Pattern of US-map.

We pattern US map from W125° to W65° and N25° to N50° at the PA-C sheet with crease line formed by the Mercator cylindrical projection method [64]. Map is divided into nine pieces along with geographical latitude, as illustrated in Figure 6-10A. The extended 2D film is a 20μm-thick PA-C film with 3μm-thick crease region, as illustrated in Figure 6-10B. Since we need both convex fold and concave fold, the width of the right crease region is set to be 30μm for concave fold, while the width of the left

crease region is set to be 10μm for convex fold. The left crease region folds in the opposite direction of the right crease region, forming a Z-shaped stack, as illustrated in Figure 6-10C.
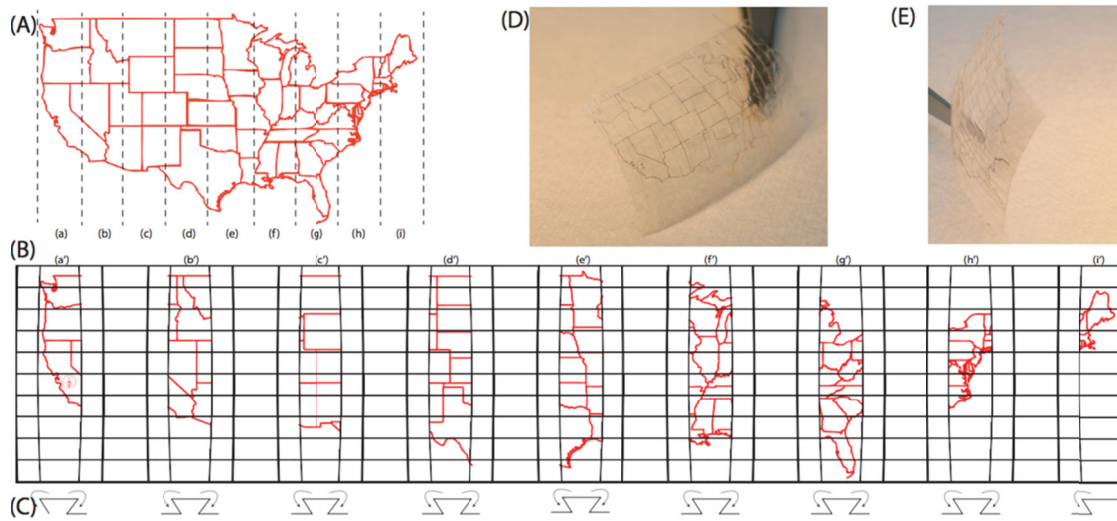
Figure 6-10. US map pattern

6.7.2 Fabrication Process

The fabrication process is similar to the origami for implant that discussed before. The major difference is that thin-film metal process is added. A 4-inch silicon wafer is cleaned in piranha solution, with three to one ratios between sulfuric acid (H2SO4) and hydro peroxide (H2O2). Natural oxide on the wafer is removed in buffered hydrofluoric acid (BHF), and we treat hexamethyldisilazane (HMDS) on wafer for more than 3 minutes in order to peel the PA-C device off easily. We deposit a 10μm thick PA-C film over the wafer. (Figure 6-11) Double-layered photoresist (PR, LOR3B, and AZ1518, AZ electronics Materials) is spin-coated, baked, and exposed with ultraviolet light for lift-off process. Oxygen plasma (50W, 200mT, 10 sec) is applied to get rid of PR residue on the

pattern for map as well as to treat the hydroxide group on the PA-C for better metal adhesion. Ti /Au (Titanium/ Gold) is deposited with e-beam evaporator one by one, and PR is rinsed in acetone and ST-22 (ACSI, Inc). (Fig. 10B) AZ4620, Thick PR, is spin-coated and patterned over the wafer for crease line (Fig. 10C), and oxygen plasma (400W, 300mT) is applied to etch through the device all the way down to silicon surface (Fig. 10D). After stripping thick PR and surface treatment with oxygen plasma (50W, 200mT, 1 min) and BHF, we deposit 2μm thick 2nd PA-C layer over the device (Fig. 10E). Finally we cut out each origami device with a dicing saw and peel it off in diH2O.
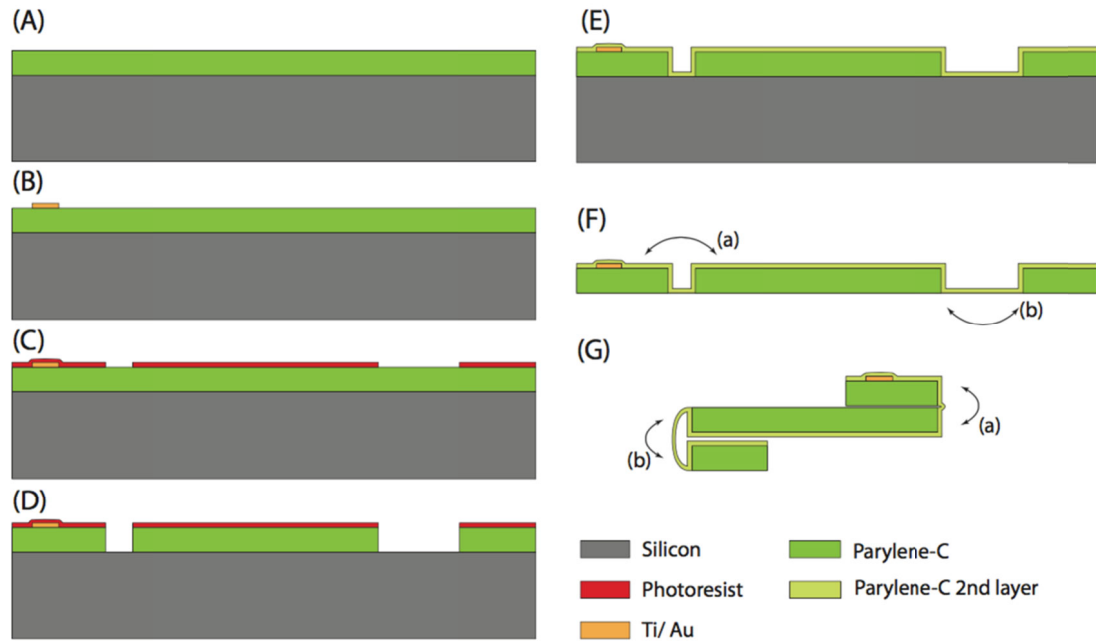
Figure 6-11. Fabrication process of origami US map

6.8 Summary

An origami technique to construct a 3D spherical structure from a 2D parylene-C (PA-C) film with designed folding crease patterns is presented. This origami technique

includes design, folding, and fixation to complete final origami devices. A lot of researches have been conducted taking advantage of the origami concept in different fields [65-81]. Here, the reported origami technique enables the possibility of first making an extended device in 2D format and then folding it into a 3D device. In our case, this new origami technique is intended for retinal implant application that requires a curved electrode array. This technique, however, can also be applied to other applications.

6.9 Reference

[57] J. H. Chang, R. Huang, Y. C. Tai, High Density 256- Channel Chip Integration with Flexible Parylene Pocket, *in Digest Tech. Papers Transducers'11 Conference*, pp. 390-393, 2011

[58] B. C. Basinger, A. P. Rowley, K. Chen, M. S. Humayun, and J. D. Weiland, Finite element modeling of retinal prosthesis mechanics, *Journal of Neural Engineering*, vol. 6, pp. 006-055, 2009

[59] K. Woo, N. Kuldeep, and C. H. Jenkins, Elective modulus of creased thin membranes, *Journal of Spacecraft and Rockets*, vol. 45, pp. 19-26, 2008

[60] K. Woo and C. H. Jenkins, Analysis of crease-wrinkle interaction for thin sheets, *Journal of Mechanical Science and Technology,* vol. 26, pp. 905-916, 2012

[61] R. J. Lang, Origami flanged pots. *http://demonstrations.wolfram.com/ Origami-FlangedPots/*

[62] J. Mitani, A design method for 3d origami based on rotational sweep, *Computer-Aided Design and Applications*, vol. 6, pp. 69-79, 2009

[63] J. Mitani, A design method for axisymmetric curved origami with triangular prism protrusions, *In Patsy Wang-Iverson*, R. J. Lang, and M. Yim, editors, Origami5, pp. 437-447. A K Peters Ltd., 2011.

[64] J. P. Snyder, Map projections–A working manual, No. 1395, USGPO, 1987

[65] J. Mosely, Square based bud, *Origami Tanteidan*, vol. 14, pp. 8, 2003

[66] J. Mosely, *Surface transitions in curved origami*, *Origami,* pp. 143-150, 2009

[67] R. J. Lang, Origami flanged pots, availabe at *http://demonstrations.wolfram.com/ Origami- FlangedPots/,* retrieved 2009

[68] K. Kuribayashi-Shigetomi, H. Onoe, and S. Takeuchi, Cell origami: self-folding of three-dimensional cell-laden microstructures driven by cell traction force. *PloS one*, vol. 7, e51085, 2012

[69] J. Elbaz, and I. Willner, DNA origami: nanorobots grab cellular control, *Nature materials*, vol. 11, pp. 276-277, 2012

[70] J. Sun, Y. Xianyu, M. Li, W. Liu, L. Zhang, D. Liu, C. Liu, G. Hu, and X. Jiang, A microfluidic origami chip for synthesis of functionalized polymeric nanoparticles, *Nanoscale*, vol. 5, pp. 5262-5265, 2013

[71] W. Liu, H. Zhong, R. Wang, and N. C. Seeman, Crystalline two‑dimensional DNA‑origami arrays, *Angewandte Chemie*, vol. 123, pp. 278-281, 2011

[72] X. C. Bai, T. G. Martin, S. H. Scheres, and H. Dietz, Cryo-EM structure of a 3D DNA-origami object. *Proceedings of the National Academy of Sciences*, vol. 109, pp. 20012-20017, 2012

[73] J. L. Silverberg, A. A. Evans, L. McLeod, R. C.Hayward, T. Hull, C. D. Santangelo, and I. Cohen, Using origami design principles to fold reprogrammable mechanical metamaterials, *Science*, vol. 345, pp. 647-650, 2014

[74] R. Tang, H. Huang, H. Tu, H. Liang, M. Liang, Z. Song, Y. Xu, H. Jiang, and H. Yu, Origami-enabled deformable silicon solar cells, *Applied Physics Letters*, vol. 104, pp. 083501, 2014

[75] H. Tu, H. Jiang, H. Yu, and Y. Xu, Hybrid silicon-polymer platform for self-locking and self-deploying origami, *Applied Physics Letters*, vol. 103, pp. 241902, 2013

[76] Y. Morikawa, S. Yamagiwa, H. Sawahata, M. Ishida, and T. Kawano, An origami-inspired ultrastretchable bioprobe film device, *In 2016 IEEE 29th International Conference on Micro Electro Mechanical Systems (MEMS)*, pp. 149-152, 2016

[77] E. A. Peraza-Hernandez, D. J. Hartl, R. J. Malak Jr, and D. C. Lagoudas, Origami-inspired active structures: a synthesis and review, *Smart Materials and Structures*, vol. 23, pp. 094001, 2014

[78] N. S. Shaar, G. Barbastathis, and C. Livermore, Integrated Folding, Alignment, and Latching for Reconfigurable Origami Microelectromechanical Systems. *Microelectromechanical Systems, Journal of*, vol. 24, pp. 1043-1051, 2015

[79]   Y. Zhao, M. S. Nandra, and Y. C. Tai, A MEMS intraocular origami coil. *In Solid-State Sensors, Actuators and Microsystems Conference (TRANSDUCERS), 2011 16th International*, pp. 2172-2175, 2011

[80]   X. M. Sun, Y. Zheng, Z. L. Li, X. H. Li, and H. X. Zhang, Flexible parylene-based MEMS inductor with Ni80Fe20 magnetic core for magnetic energy coupling system, *In Proceedings of Power MEMS 2012*, pp. 62-65, 2012

[81]   G. T. PIcKETT, Self-folding origami membranes, *Europhysics Letters*, vol. 78, pp. 48003, 2007

7 CONCLUSION

This work presents parylene based novel filters for biomedical applications. Three medical devices have been proposed, together with the parylene characterization and parylene origami structure design. In chapter 1, first of all the parylene is introduced. Parylene has been selected as the bioMEMS material because of a variety of favorable properties, including biocompatibility, good machinability, and so on. After that, the detailed parylene processing technology (low pressure chemical vapor deposition) is discussed. Parylene membrane applications in the bio and medical device field are reviewed, and several state-of-art researches are listed and discussed as examples. The second part of the chapter 1 focuses on the MEMS technology, including the history, overview, and state-of-art techniques. Among all the techniques, photolithography, bulk micromachining, and thin film process are particularly discussed in details.

The topic of chapter 2 is the parylene properties. Here, the mechanical properties and the surface properties are studied. For the mechanical properties, the dynamic mechanical analysis method is used to perform the uniaxial tensile test and the glass transition temperature test. For the surface properties, plasma treatment methods are applied to change the surface properties of parylene membranes. Stable hydrophilic surfaces are achieved for the cell attachment and growth study.

Chapter 3 focuses on the parylene magnesium embedded filter for circulating tumors cells isolation. State-of-art CTC detection techniques are reviewed and the motivation of this novel design is to help release the circulating tumor cells once captured by the slot filter. To achieve this goal, magnesium is applied as the biodegradable sacrificial layer on the new design. The properties of magnesium, including the processing technology and the etching properties together with the modeling, are studied. Both the material design and structural design of the parylene based magnesium filter are introduced, together with the fabrication methods, setup design and assembly.

Chapter 4 presented a novel parylene based microelectrode filter for single islet electroisletogram. Islets transplantation has become a promising way to treat the type I diabetes. The goal for this device is to screen the every individual islet based on the EIG to increase the quality of implanted islets. In the design section, both system level design and the microelectrodes filter design are studied. After the assembly and integration, the results are presented and discussed.

In chapter 5, parylene-on-PDMS membrane is investigated for vaccine production. The main target for the parylene-on-PDMS device is to increase the cell density for cell and virus culture. The oxygen permeation study has been performed before the cell growth experiments. The result indicates the device to be promising for largely increasing the cell numbers per volume.

The last chapter is on parylene origami structure. By folding the parylene membrane, 3D structures can be created from 2D. This origami technique includes design, folding, and fixation to complete the final origami devices.

In conclusion, the applications of parylene membranes are explored. Given different goals and different requirements, extra functionalities, modifications, and designs have been added to the parylene filters to make them "smart". Further improvements and optimizations are definitely needed for all the three devices. For instance, stacks of parylene-on-PDMS membranes need to be investigated to truly improve the cell culture. Still, however, the initial results do give us the confidence that smart parylene filter devices can be useful for the practical biomedical applications, and there will be more and more useful and interesting parylene filters invented in the future.